Characterisation of dynamic wind turbine rotor loads under normal and fault conditions

Oleksandr Chernyavskii

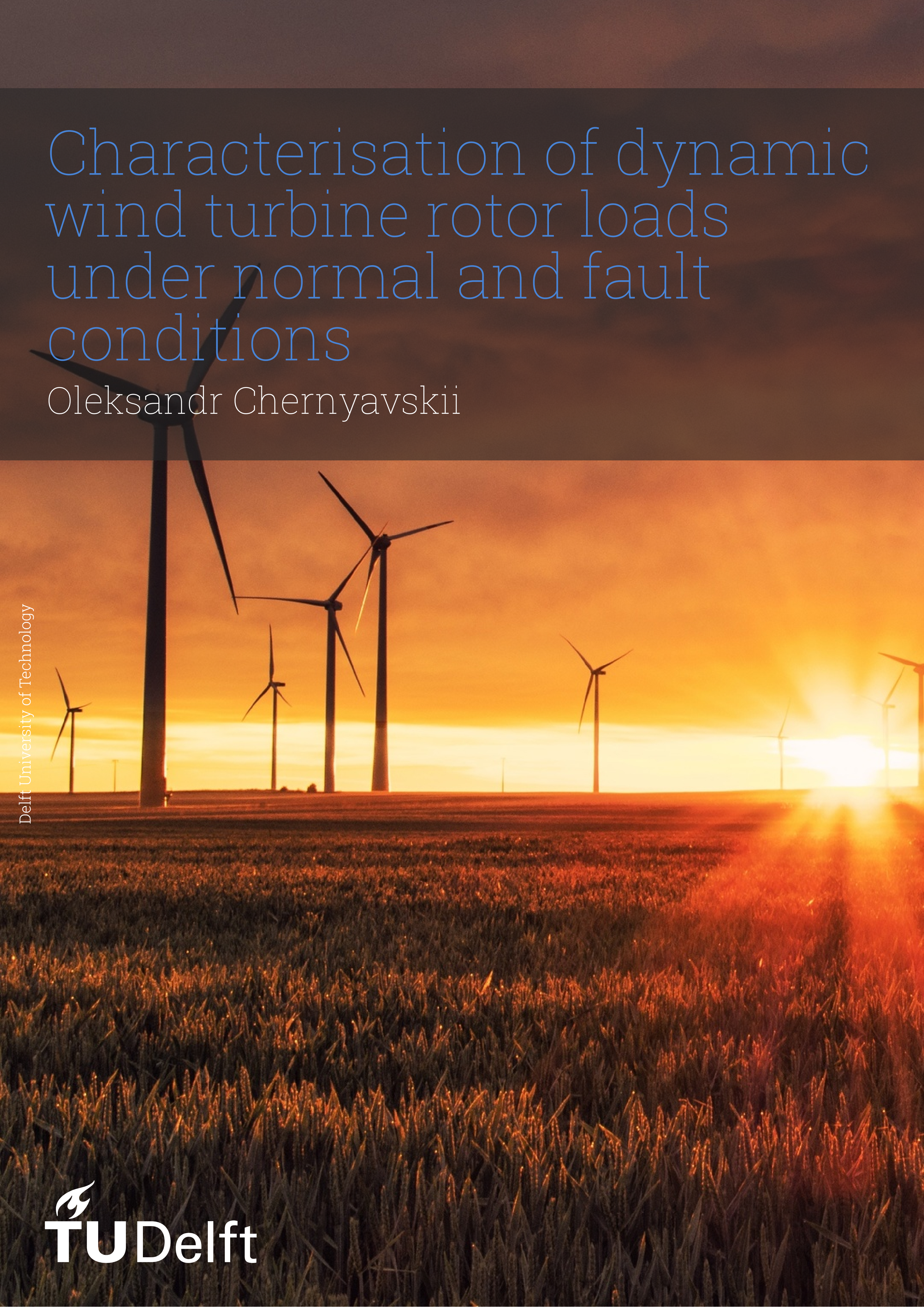

Delft University of Technology

Characterisation of dynamic wind turbine rotor loads under normal and fault conditions

by

Oleksandr Chernyavskii

to obtain the degree of Master of Science in Sustainable Energy Technology at Delft University of Technology
Wind Energy Group, Faculty of Aerospace Engineering, Delft University of Technology.

Student number:	4788869
Project duration:	November 22, 2023 – April 16, 2025
Main Supervisor:	Dr. D. Zappalá
Post-doc Assistant:	Dr. S. K. Pal

Cover: TU Delft Report Style, with modifications by Daan Zwaneveld

TU Delft

Abstract

As the demand for wind energy grows worldwide, so is the need to minimise the Levelized Cost of Electricity of wind energy. Rotor imbalances like Pitch Misalignment, Mass Imbalance and Yaw Misalignment commonly occur in the rotor and are often not detected on time, leading to increased component wear and possible component failure, therefore increasing the running costs of the wind turbine and downtime. The aim of this thesis is to investigate approaches to remotely detect and characterise rotor imbalances based on the system's dynamic responses to faulty operating conditions.

The methodology, derived from literature, involves modelling three cases of rotor imbalance – Pitch Misalignment, Mass Imbalance and Yaw Misalignment – in a wind turbine simulation tool OpenFAST. The models are simulated under different environmental conditions at three levels of fault severity and healthy conditions. The environmental conditions vary across six wind speeds, three of which are below rated and three are above rated. In addition, the simulated turbines are tested under steady and turbulent wind conditions. A series of simulations is conducted for every combination of rotor imbalance type, wind speed and fault level, under both steady and turbulent wind conditions. The output signals, low speed shaft moments and forces in x, y and z directions, are later analysed in the frequency domain by dividing the signals into 60 one-minute windows and performing a Fast Fourier Transform on each window separately. The windows in the frequency domain are then averaged, and peak amplitudes are extracted at 1P, 2P and 3P frequency. Finally, the peak amplitudes in cases with rotor imbalance are compared to those of a turbine with a healthy rotor.

The results show different dynamic responses for each case of rotor imbalance, represented by an absolute difference between healthy and faulty cases. For the case of pitch misalignment, significant excitations of the 1P moment harmonics in y and z directions are observed, with peak amplitudes ranging between 10^3 and 10^4 kNm, increasing with both wind speed and fault level. For the case of mass imbalance, excitations at 1P force harmonics in y and z directions are observed, with peak amplitudes ranging between 10^0 and 10^1 kN, increasing with fault level. Lastly, for the case of yaw misalignment, excitations at 3P moment harmonics in y and z directions are observed, with peak amplitudes ranging between 10^0 and 10^2 kNm, increasing with wind speed and fault level. Based on the results, a decision tree is proposed which can be used to detect and characterise rotor imbalances present in the rotor, based on the system's dynamic responses.

The findings presented in this work show that remote fault detection and characterisation could be feasible for the three cases of rotor imbalance investigated in this work. Further research can be done to build upon the findings of this work to develop a more robust fault detection and characterisation method, by investigating of other types and combinations of rotor faults for wind turbines of all sizes.

Contents

Abstract i

Nomenclature vii

1 Introduction 1
1.1 Overview . . . 1
1.2 Objectives . . . 2

2 Background and Literature 4
2.1 Wind Turbine Physics . . . 4
2.1.1 Momentum Conservation . . . 4
2.1.2 Blade Element Theory . . . 5
2.2 Wind Turbine System Dynamic Response . . . 7
2.2.1 Periodic Frequencies . . . 8
2.3 Current Fault Detection Techniques . . . 12
2.3.1 Data Collection . . . 12
2.3.2 Data Analysis and Fault Diagnosis . . . 13
2.4 Most Common Rotor Imbalances . . . 13
2.4.1 Pitch Misalignment . . . 13
2.4.2 Mass Imbalance . . . 14
2.4.3 Yaw Misalignment . . . 15
2.5 System Integration and Socioeconomic Impact . . . 16
2.5.1 Stakeholder Analysis . . . 16
2.5.2 Financial Aspects of Maintenance . . . 18

3 Methodology 22
3.1 Modelling Setup . . . 22
3.1.1 DTU 10 MW Reference Wind Turbine . . . 22
3.1.2 OpenFAST Modules and Fault Cases . . . 22
3.1.3 Environmental Cases . . . 24
3.1.4 OpenFAST Initialisation . . . 26
3.2 Data Processing . . . 27
3.2.1 Processing Strategy . . . 27
3.2.2 Processing Algorithm . . . 27
3.2.3 Data Analysis and Presentation . . . 29
3.2.4 Rotor Imbalance Characterisation . . . 31

4 Results and Discussion 33
4.1 Steady Wind Simulation Results . . . 33
4.1.1 Low Speed Shaft Moment . . . 33
4.1.2 Low Speed Shaft Force . . . 35
4.1.3 Discussion . . . 38
4.2 Turbulent Wind Simulation Results . . . 41
4.2.1 Low Speed Shaft Moment . . . 42
4.2.2 Low Speed Shaft Force . . . 42
4.2.3 Discussion and Comparison . . . 42
4.3 Fault Detection and Characterisation . . . 48

5 Conclusions 51

6 Recommendations 53

References **55**

A MATLAB Code: Peak Extraction Algorithm **59**

B Absolute Difference in Peak Magnitude Between Healthy and Faulty Rotor **63**
B.1 Steady State Bar Plots 64
B.2 Turbulent State Bar Plots 70

C FFT of the Signal at Steady Wind Conditions **76**
C.1 Pitch Misalignment 77
C.2 Mass Imbalance 80
C.3 Yaw Misalignment 83

List of Figures

1.1 Cumulative Installed Capacity of Wind Energy Worldwide [2] 1

2.1 Streamtube around an actuator disk [11] 5
2.2 The Velocity Triangle on a blade element [11] 6
2.3 Relationship Between Pitch Angle, Power Generation and Wind Speed [12] 7
2.4 Dynamic Amplification Factor at Various Damping Coefficients 8
2.5 1P Force Harmonics Produced by Each Blade Due to Tower Shadow Effect [11] 9
2.6 2P Force Harmonics Produced by Each Blade Due to Tower Shadow Effect [11] 10
2.7 Pitch Misaligned Blade Position Over One Rotational Period 10
2.8 3P Force Harmonics Produced by Each Blade Due to Tower Shadow Effect [11] 12
2.9 Effects of pitch misalignment on LSS loads [22] 14
2.10 Rotor mass imbalance forces caused by a point mass in one of the blades, in rotating (x,y,z) and fixed coordinate frame (X,Y,Z) [6] 15
2.11 Stakeholder Power-Interest Grid 17
2.12 Levelized Cost Breakdown for Reference Land-based Wind Plant [41] 18
2.13 Levelized Cost Breakdown for Reference Offshore-based Wind Plant [41] 19
2.14 GPRA Cost Reduction Pathway From 2016 to 2030 for Onshore Wind Energy [41] . . . 19
2.15 GPRA Cost Reduction Pathway From 2016 to 2030 for Offshore Wind Energy [41] . . . 20
2.16 TTF Probability based on number of previous faults [44] 21

3.1 Data Processing Strategy 27
3.2 Sorting peak-frequency pairs into separate columns 28
3.3 Example bar plot: Absolute Change in LSS Moment at U_1 and 1P 29
3.4 Difference in Moment and Force Peaks in LSS Between Healthy and Faulty Conditions, Steady Wind 30
3.5 Difference in Moment and Force Peaks between Healthy and Faulty Conditions, Turbulent Wind 31

4.1 Absolute Change in LSS Moment Below and Above Rated Wind Speeds at 1P Harmonic in Steady Wind Conditions 33
4.2 Absolute Change in LSS Moment Below and Above Rated Wind Speeds at 2P Harmonic in Steady Wind Conditions 34
4.3 Absolute Change in LSS Moment Below and Above Rated Wind Speeds at 2P Harmonic in Steady Wind Conditions 35
4.4 Absolute Change in LSS Force Below and Above Rated Wind Speeds at 1P Harmonic in Steady Wind Conditions 36
4.5 Absolute Change in LSS Force Below and Above Rated Wind Speeds at 2P Harmonic in Steady Wind Conditions 36
4.6 Absolute Change in LSS Force Below and Above Rated Wind Speeds at 3P Harmonic in Steady Wind Conditions 37
4.7 Rotor Fault Characterization Decision Tree 50

B.1 Absolute Change in LSS Moment Below and Above Rated Wind Speeds at 1P Frequency in Steady Wind Conditions 64
B.2 Absolute Change in LSS Moment Below and Above Rated Wind Speeds at 2P Frequency in Steady Wind Conditions 65
B.3 Absolute Change in LSS Moment Below and Above Rated Wind Speeds at 3P Frequency in Steady Wind Conditions 66

B.4 Absolute Change in LSS Force Below and Above Rated Wind Speeds at 1P Frequency in Steady Wind Conditions 67
B.5 Absolute Change in LSS Force Below and Above Rated Wind Speeds at 2P Frequency in Steady Wind Conditions 68
B.6 Absolute Change in LSS Force Below and Above Rated Wind Speeds at 3P Frequency in Steady Wind Conditions 69
B.7 Absolute Change in LSS Moment Below and Above Rated Wind Speeds at 1P Frequency in Turbulent Wind Conditions 70
B.8 Absolute Change in LSS Moment Below and Above Rated Wind Speeds at 2P Frequency in Turbulent Wind Conditions 71
B.9 Absolute Change in LSS Moment Below and Above Rated Wind Speeds at 3P Frequency in Turbulent Wind Conditions 72
B.10 Absolute Change in LSS Force Below and Above Rated Wind Speeds at 1P Frequency in Turbulent Wind Conditions 73
B.11 Absolute Change in LSS Force Below and Above Rated Wind Speeds at 2P Frequency in Turbulent Wind Conditions 74
B.12 Absolute Change in LSS Force Below and Above Rated Wind Speeds at 3P Frequency in Turbulent Wind Conditions 75

C.1 FFT of PMx LSS Torque at different fault levels and wind speeds 77
C.2 FFT of PMx LSS Thrust at different fault levels and wind speeds 77
C.3 FFT of PMy LSS Moment at different fault levels and wind speeds 78
C.4 FFT of PMy LSS Force at different fault levels and wind speeds 78
C.5 FFT of PMz LSS Moment at different fault levels and wind speeds 79
C.6 FFT of PMz LSS Force at different fault levels and wind speeds 79
C.7 FFT of MIx LSS Torque at different fault levels and wind speeds 80
C.8 FFT of MIx LSS Thrust at different fault levels and wind speeds 80
C.9 FFT of MIy LSS Moment at different fault levels and wind speeds 81
C.10 FFT of MIy LSS Force at different fault levels and wind speeds 81
C.11 FFT of MIz LSS Moment at different fault levels and wind speeds 82
C.12 FFT of MIz LSS Force at different fault levels and wind speeds 82
C.13 FFT of YMx LSS Torque at different fault levels and wind speeds 83
C.14 FFT of YMx LSS Thrust at different fault levels and wind speeds 83
C.15 FFT of YMy LSS Moment at different fault levels and wind speeds 84
C.16 FFT of YMy LSS Force at different fault levels and wind speeds 84
C.17 FFT of YMz LSS Moment at different fault levels and wind speeds 85
C.18 FFT of YMz LSS Force at different fault levels and wind speeds 85

List of Tables

3.1 Design parameters of DTU 10 MW reference turbine [49] 22
3.2 Fault cases for each type of rotor imbalance. 24
3.3 Basic Parameters for Wind Turbine Classes [57]. 25
3.4 Environmental Parameter Settings 25
3.5 List of Output Parameters 26
3.6 Periodic Frequency Values at Each Wind Speed 26
3.7 Summary tables legend for moment and force 31

4.1 Average Moment and Force Peak Difference in LSS Between a Healthy Rotor and a Rotor with PM, Steady Wind 39
4.2 Summary table for the case of PM at steady wind conditions 39
4.3 Average Moment and Force Peak Difference in LSS Between a Healthy Rotor and a Rotor with MI, Steady Wind 40
4.4 Summary table for the case of MI at steady wind conditions 40
4.5 Average Moment and Force Peak Difference in LSS Between a Healthy Rotor and a Rotor with YM, Steady Wind 41
4.6 Summary table for the case of YM at steady wind conditions 41
4.7 Average Moment and Force Peak Change in LSS Between Healthy Rotors in Turbulent and Steady Wind Conditions 43
4.8 Average Moment and Force Peak Change in LSS Between a Healthy Rotor and a Rotor with PM, Turbulent Conditions 43
4.9 Average Moment and Force Peak Change in LSS Between Turbulent and Steady Wind Conditions in a Rotor with PM 44
4.10 Summary table for the case of PM in turbulent wind conditions 45
4.11 Average Moment and Force Peak Change in LSS Between a Healthy Rotor and a Rotor with MI, Turbulent Conditions 45
4.12 Average Moment and Force Peak Change in LSS Between Turbulent and Steady Wind Conditions in a Rotor with MI 46
4.13 Summary table for the case of MI in turbulent wind conditions 46
4.14 Average Moment and Force Peak Change in LSS Between a Healthy Rotor and a Rotor with YM, Turbulent Conditions 47
4.15 Average Moment and Force Peak Change in LSS Between Turbulent and Steady Wind Conditions in a Rotor with YM 47
4.16 Summary table for the case of YM in turbulent wind conditions 47

Nomenclature

Abbreviations

Abbreviation	Definition
AEP	Annual Energy Production
BEMT	Blade Element Momentum Theory
CAPEX	Capital Expenditure
DAF	Dynamic Amplification Factor
FFT	Fast Fourier Transformation
GL	Germanischer Lloyd
GPRA	Government Performance and Results Act
IEC	International Electrotechnical Commission
LCOE	Levelized Cost of Electricity
LSS	Low Speed Shaft
MI	Mass Imbalance
ML	Machine Learning
O&M	Operation and Maintenance
PM	Pitch Misalignment
SCADA	Supervisory Control and Data Acquisition
TTF	Time to Failure
TTR	Time to Repair
WT	Wind Turbine
YM	Yaw Misalignment

Symbols

Symbol	Definition	Unit
a	Induction factor	[—]
c	Damping coefficient	[kg/s]
c_D	Drag coefficient	[—]
c_L	Lift coefficient	[—]
F	Force	[N]
k	Stiffness coefficient	[N/mm]
l	Blade section length	[m]
m	Mass	[kg]
$\dot{m}$	Mass flow rate	[kg/s]
M	Moment	[kNm]
R	Resultant force	[N]
T	Thrust Force	[N]
U	Velocity	[m/s]
U_e	Velocity downstream	[m/s]
U_r	Velocity at rotor	[m/s]
V_{res}	Resultant velocity	[m/s]
x_d	Dynamic amplitude	[—]
x_s	Static amplitude	[—]
α	Angle of attack	[°]
Δf	Increment in force magnitude	[N]

Symbol	Definition	Unit
ω	Excitation frequency	[rad/s]
ω_n	Natural frequency	[rad/s]
ϕ	Inflow angle	[°]
ρ	Density	[kg/m^3]
θ	Pitch angle	[°]
xP	Periodic Rotor Harmonic Amplitude (x times per revolution)	[kN]/[kNm]

1
Introduction

1.1. Overview

Climate change has been a rising issue in recent history, as greenhouse gas emissions have been increasing due to human activity [1]. To tackle the problem, scientists are considering various methods to reduce greenhouse emissions, one of which is renewable energy generation. Wind turbines (WTs) have shown to be one of the most promising renewable energy generation methods, with its capacity more than doubling since 2016, increasing to 1017 GW installed capacity worldwide in 2023 [2], as shown in Figure 1.1.

Performance of a WT or a wind park can be measured by calculating the Levelized Cost of Electricity (LCoE), which calculates the price of energy output as a function of investment cost (CAPEX), operation and maintenance cost (O&M) and the WT's lifetime, where lower LCoE is desirable. The LCoE is minimised by lowering CAPEX and O&M costs as much as possible, while trying to maximise the turbine's lifespan. WTs consist of many components that require large upfront investment, of which blades are by far the most expensive, as they take up around 20% of the WT cost [3]. While investors are prepared to spend large amounts on WTs and O&M, as both are accounted for in the calculation of LCoE, component failure is not accounted for in this calculation and may significantly impact both the risk and running costs of the WT [4]. As the blades are the most expensive component of a WT, blade failure should be considered in this calculation.

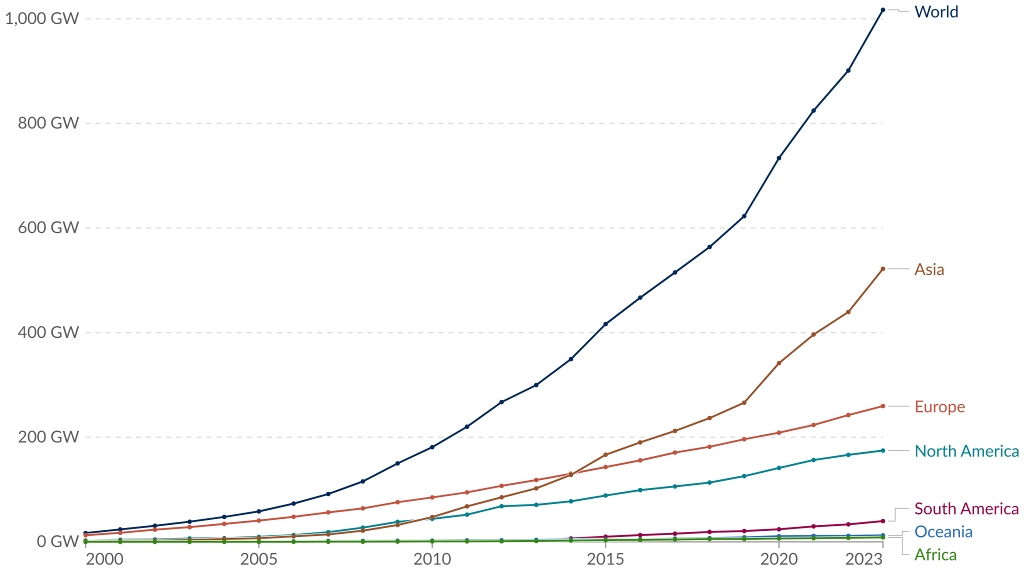

Figure 1.1: Cumulative Installed Capacity of Wind Energy Worldwide [2]

In general, rotor faults are serious issues for WTs, and it is quite difficult to detect and characterise the exact type of fault present in the rotor and its location [3, 5]. The most common types of rotor faults are, but not limited to: leading edge erosion, surface cracks, delamination, ice accumulation, mass imbalance and installation or controller defects like pitch and yaw misalignment [3, 5, 6]. Different types of faults require different types of maintenance, and therefore it is important to be able to characterise faults to distinguish one fault type from another. Today, rotor fault detection techniques are rather simplistic, which most commonly involves trained professionals inspecting the turbine manually in person, while they harness themselves to the blade using cables [7, 8]. Not only is this method dangerous for the workers, it is also time-consuming and not very effective at detecting internal damage to the blade and rotor imbalances, such as internal micro-cracks, rotor mass imbalances and blade pitch misalignment, since they are not visible to the naked eye [7–9].

Other methods involving inspection using cameras or drones are faster and safer alternative methods of blade inspection. However, they also experience difficulty with detecting issues with the blades' internal structure and rotor imbalances, as they can only inspect the blade on the surface level. In addition, using cameras and drones may also come with losing accuracy in detecting damage, as it depends on various factors, such as: lighting, camera resolution, camera focus and more [8]. Detecting faults in the blades and the rotor is rather important, since such faults may result in dynamic and/or aerodynamic discrepancies, causing undesirable fatigue loading and wear, due to force and moment fluctuations in the rotor, which could cause other components of the drive train to suffer, too [6, 9]. Therefore, it is crucial to derive a more accurate method of rotor fault detection and characterisation, that could be achieved remotely and cost effectively, without putting WT technicians into hazardous environments.

1.2. Objectives

This research aims to find a way to correctly detect and characterise common rotor fault conditions based on the dynamic responses of a WT, operating under faulty conditions. A rotor fault can be detected if the dynamic response profile does not match with the profile of a healthy rotor. While it can be characterised if the faulty rotor's dynamic response profile can be distinguished from that of a different rotor fault, allowing dynamic responses to be linked to specific rotor faults. Different types of faults will be investigated and modelled by either altering blade structure or rotor properties based on methods found in literature. The dynamic system responses will be used to analyse a WT under healthy and faulty rotor conditions, using the techniques and methodologies found in literature. In order to accomplish the objectives of this research, the following research question and sub-questions need to be addressed:

Main Question

Can common wind turbine rotor faults be detected and characterised, based on the dynamic system responses, under faulty operating conditions?

Sub-Questions

- Which output signals can be used to detect faults present in the rotor, and what signal characteristics should be considered in the process?
- To what extent can rotor fault conditions be differentiated from another, based on the dynamic responses of a wind turbine?
- How are wind turbine's dynamic system responses influence by a change in the wind speed, under healthy and faulty conditions?
- What effects do turbulent environmental conditions have on a wind turbine's dynamic system responses?

Subsequently, the report will have the following structure. Chapter 2 will provide all the necessary background information involved in this research, such as background physics and related literature review. Chapter 3 will present the methodology that was used to simulate healthy and faulty cases, as well as the way the data was handled. Chapter 4 will present analysis of the results obtained from simulations, and discuss the meaning and potential implications of the results. Chapter 5 will lay out the key takeaways and conclusions of this research and provide answers to the research questions. Lastly, Chapter 6 will highlight the limitations of this work and provide recommendations for potential future research.

2
Background and Literature

This chapter aims to familiarise the reader with concepts related to wind turbine rotor faults. Section 2.1 contains necessary background physics of a WT, and provides key operation principles. Section 2.2 depicts the dynamic system response of a WT and provides insights into signal processing and periodic frequencies typical in a WT. Section 2.3 gives an overview of most common ways WT faults are detected in literature, including data collection and analysis methods. Section 2.4 gives an overview of three common rotor imbalance types, which are investigated in this thesis. Lastly, section 2.5 discusses the socioeconomic impact of integrating new technology, going into detail about which stakeholders are involved and how it may impact the costs of maintenance.

2.1. Wind Turbine Physics

The first step of understanding WT blade damage modelling is delving into the related physics behind the turbines, as it will help understand causes and effects of different blade damage types and help draw conclusions on what is observed. To begin with, it is important to touch upon the core principles of how the rotor of the wind turbine interacts with the wind, which in turn causes the rotor to revolve. In rotor design, Blade Element Momentum Theory (BEMT) is used to determine the performance of the rotor based on its geometrical and mechanical parameters, as well as the way these parameters interact with the flow of the incoming wind [10]. The theory consists of two main parts: momentum conservation theory and blade element theory. However, to explain blade element theory, the concept of momentum conservation needs to be explained fist.

2.1.1. Momentum Conservation

Momentum conservation theory for WTs is based on the law of mass conservation and Bernoulli's principle. The theory assumes that the rotor is stationary, has a shape of an infinitesimally thin disk, and exerts an even thrust force on the flow. With these assumptions in mind, Figure 2.1 depicts the interaction between the flow and the actuator disk in a simple diagram [10, 11].

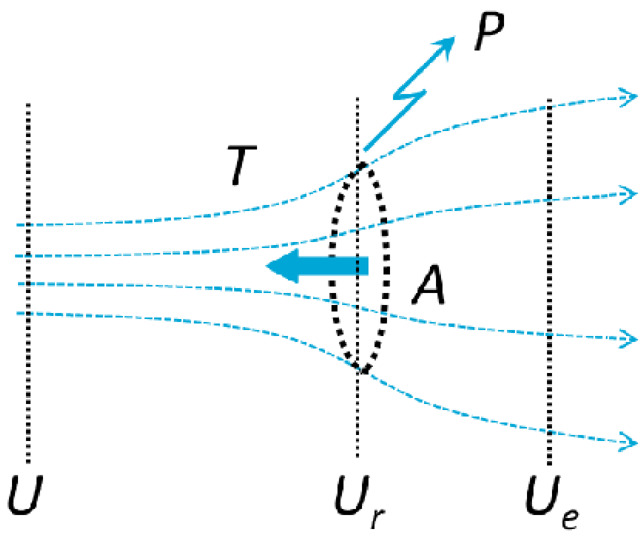

Figure 2.1: Streamtube around an actuator disk [11]

In this diagram, a set of streamlines form a streamtube of inviscid flow of velocity, U, around the actuator disk of area A. As the flow reaches the actuator disk, thrust force, T, exerted by the disk on the flow, slows the flow down to velocity U_e at the outlet, causing the flow to reduce in pressure and expand in volume, by Bernoulli's principle. By the law of mass conservation, mass flow rate, $\dot{m}$, upstream and downstream of the actuator disk must be equal, thus, implying that momentum of the flow downstream of the actuator disk is smaller than upstream. However, the momentum in the streamtube must be conserved, therefore, the momentum did not disappear, but rather is transferred into the thrust force, making it equal to the difference between the upstream and downstream momentum, shown in Equation 2.1.

$$T = \dot{m}(U - U_e) \tag{2.1}$$

As it was deduced earlier, the thrust induced by the rotor slows down the upstream flow of the wind. The amount that the upstream flow slows down by can be described the non-dimensional parameter a, which is known as the induction factor and is defined as a ratio between the difference of upstream velocity and velocity at the rotor, and the upstream velocity. The induction factor can be characterised by the Equation 2.2. Subsequently, velocity at the rotor can be defined by rearranging Equation 2.2, to obtain an expression for velocity at the rotor, which is expressed by Equation 2.3. Now that these quantities have been defined, blade element theory can now be explained in the next section.

$$a = \frac{U - U_r}{U} = \frac{\Delta U}{U} \tag{2.2}$$

$$U_r = U(1 - a) \tag{2.3}$$

2.1.2. Blade Element Theory

Blade Element Theory (BET) considers the blade to be divided into multiple smaller sections, each representing a cross-section of an airfoil. Figure 2.2 represents such a blade element in a velocity triangle diagram, which represents all the necessary information to determine the forces that act on the blade element.

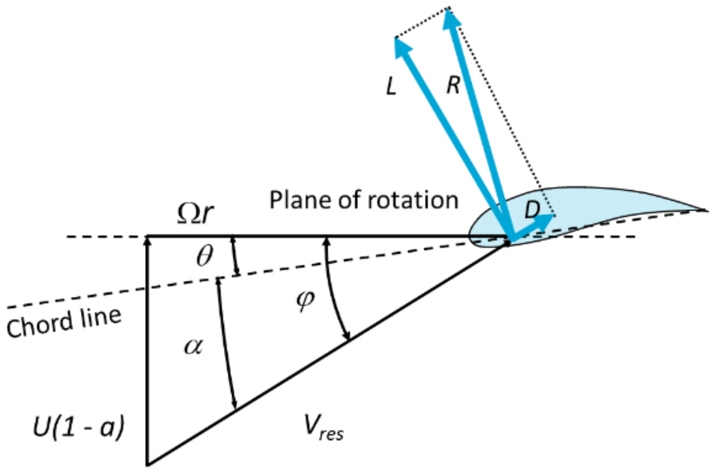

Figure 2.2: The Velocity Triangle on a blade element [11]

As the rotor rotates with velocity Ωr, and the inflow wind flows with velocity $U(1-a)$, the airfoil essentially interacts with the air at the resultant velocity vector, V_{res}, which can be defined by Equation 2.4. The resultant wind, in turn, creates a lift force, L, and a drag force, D, as it flows around the airfoil, creating the resultant force, R, which drives the rotation of the rotor. The lift and drag forces can be represented with Equation 2.5 and Equation 2.6, respectively, where ρ is air density, c_L and c_D are lift and drag coefficients, c is the cord length and l is the blade section length.

$$V_{res} = \sqrt{(\Omega r)^2 + (U(1-a))^2} \tag{2.4}$$

$$L = \frac{1}{2} c_L \rho V_{res}^2 cl \tag{2.5}$$

$$D = \frac{1}{2} c_D \rho V_{res}^2 cl \tag{2.6}$$

Furthermore, by having a closer look at the diagram, it is apparent that V_{res} meets the airfoil at an angle. This angle is known as the inflow angle, denoted by φ, and it is composed of two angles: the angle of attack, α, and the pitch angle, θ. The lift and drag coefficients are functions of α, which represents the angle between V_{res} vector and the chord line of the airfoil. As a design parameter, α must be chosen in a way that maximizes c_L and minimizes the c_D to utilize the energy of the wind to the fullest and optimize power production. However, that is only the case for winds of speeds below rated conditions. Above rated wind speed, α is increased beyond it's optimal value in order to limit the amount of lift the blades produce. This is done to protect the blades and drive-train components from high loads and natural frequencies caused by the rotor, keeping power production constant by doing so. To achieve this, the blades are pitched using motors located at the root of each blade, which essentially varies the angle θ to vary the angle α, shown in Equation 2.7.

$$\alpha = \varphi - \theta \tag{2.7}$$

The effect of blade pitching is demonstrated in Figure 2.3. It can be seen on the LHS plot that at below rated wind speed of around 11 m/s, the pitch of the blade does not change, as it is the most optimal blade orientation for power generation. By keeping pitch angle constant, the power generation increases cubically with wind speed, as seen on the RHS plot. However, at above rated wind speeds, the pitch angle begins to increase with wind speed. This causes power generation curve to flatten, since blades are aerodynamically stalling WT's rotation, generating constant power.

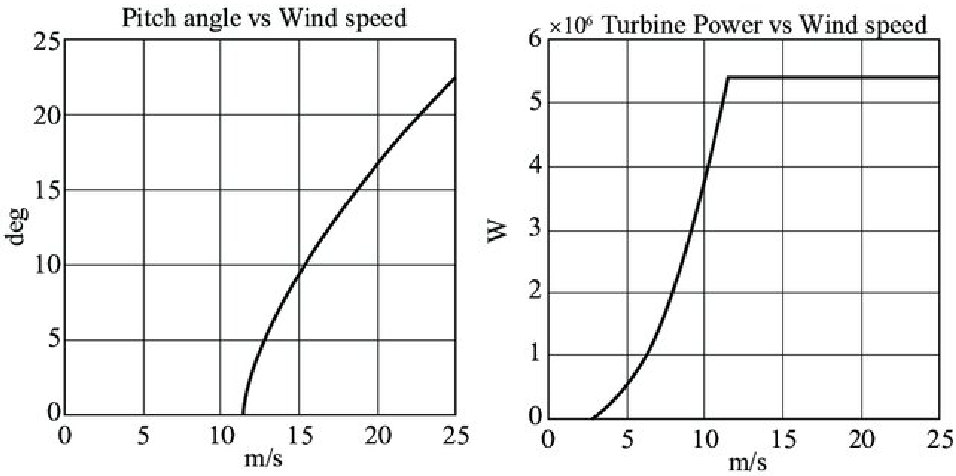

Figure 2.3: Relationship Between Pitch Angle, Power Generation and Wind Speed [12]

Therefore, the orientation of the airfoil with respect to the inflow wind is a crucial design parameter, bearing the responsibility of optimizing the power production and dynamic load conditions for WT components. Faults related to blade orientation may have a significant impact on the O&M costs and this will be discussed later in section 2.5.

2.2. Wind Turbine System Dynamic Response

WTs constantly experience both static and dynamic loads. Constant loads refer to loads that do not vary with time, resulting in stress, deformation, displacement and acceleration in the structure. On the other hand, dynamic loads refer to loads that vary with time, causing vibrations and oscillations of the structure. In general, any structure has dynamic responses to applied loads. Dynamic Amplification Factor (DAF) is a measure of how a structure responds to dynamic loading compared to how it responds to static loading [11]. By definition, DAF is measured as a ratio of dynamic and static amplitude, x_d and x_s, respectively, which can be written in terms of excitation frequency ω and natural frequency ω_n, seen in Equation 2.8, where k and c are static and dynamic coefficients, respectively, and m is the mass. The equation can be further simplified to Equation 2.9, assuming damping is negligible.

$$DAF = \frac{x_d}{x_s} = \frac{k}{\sqrt{\left(k - m\omega^2\right)^2 + (c\omega)^2}} \tag{2.8}$$

$$DAF = \frac{1}{|1 - \frac{\omega^2}{\omega_n^2}|} \tag{2.9}$$

where:

$$\omega_n = \sqrt{\frac{k}{m}} \tag{2.10}$$

The natural frequency of a structure is a frequency at which a structure vibrates in response to being displaced from its equilibrium position and allowed to vibrate freely [11]. For instance, a simple mass spring system is displaced from its equilibrium position and let go, it will start oscillating at its natural frequency. In reference to Equation 2.9, if ω approaches ω_n, the DAF begins approaching infinity, assuming no damping is present. Figure 2.4 graphically represents the dynamic responses of a structure as ω approaches ω_n, at different values of c. It can be seen that as frequency ratio approaches 1, the dynamic response is the largest, and its suppressed by the system's damping. When this happens, the structure is said to be in resonance.

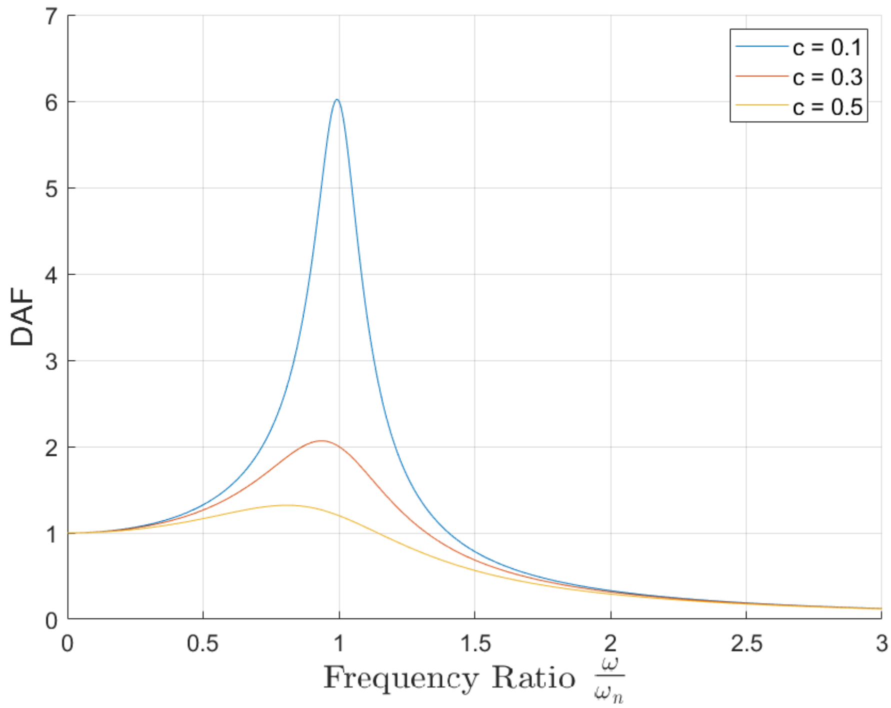

Figure 2.4: Dynamic Amplification Factor at Various Damping Coefficients

In general, complex structures like WTs have multiple degrees of freedom to consider, due to the large number of components present in the structure. Each component has their own mass, stiffness and damping coefficients, resulting in the WT having multiple natural frequencies. WTs operate at a wide range of wind speeds, resulting in a wide range of aerodynamic forces and rotor speeds. This means that by design, the natural frequency of components should not interfere with the rotational frequency of the rotor.

2.2.1. Periodic Frequencies

The periodic frequency of the rotor represents how many times the period of the load oscillates per rotor revolution. In literature, periodic frequencies are commonly denoted by 1P, 2P, 3P, meaning once, twice and three times per rotor revolution, respectively. Periodic frequencies are not fixed, since WT rotors operate at variable speeds, thus they increase linearly with rotor speed. The operational range of the rotor refers to the rotor speed between cut-in and cut-out wind speed [11]. The objective of the WT designers is to design components in a way that does not interfere with periodic frequencies assocciated with the operational frequeincies of the rotor. While higher order periodic frequencies may occur in the WTs, this thesis focuses primarily on 1P, 2P and 3P rotor frequencies.

Periodic frequencies in the rotor may stem from a varierty of origins. Most commonly, the cause is either gravitational or aerodynamic in origin [11][13]. Graviational sources of periodic frequencies can arise from mass imbalance in the rotor, where mass is not evenly distributed throughout the rotor. This in turn changes the centre of mass of the rotor, causing periodic load oscilations. Periodic frequiences aerodynamic in origin usually stem from aerodynamic imbalances. Aerodynamic imbalance is often caused by blade pitch misalignment or rotor yaw misalignment, which causes the rotor to interact with the wind unevenly. Moreover, uneven flow itself may induce uneven aerudoynamic loading onto the rotor. For instance, the tower shadow is a region near the tower, where the wind field in front and behind of the tower changes, resulting in slower wind in that region [11]. As the blades pass this region, they experience a change in aerodynamic load, as well as a change of angle of attack, due to a smaller free stream velocity vector, which can be visualised in Figure 2.2.

1P harmonic

The 1P harmonic is commonly caused by aerodynamic or gravitational imbalances in the rotor [6] [11]. These rotor imbalances are usually caused by pitch missalignment or mass imbalance in one of the blades, respectively. For example, in a healthy three-bladed rotor, each blade experiences an even load variation with a 1/3 shift of the period in the force variation harmonic. Therefore, when all three blade harmonics at 1P harmonic are added together, the 1P harmonics cancel out. This can be seen in Figure 2.5, where force harmonics produced by each of the three blades are shown, as the rotor completes 1 revolution per second.

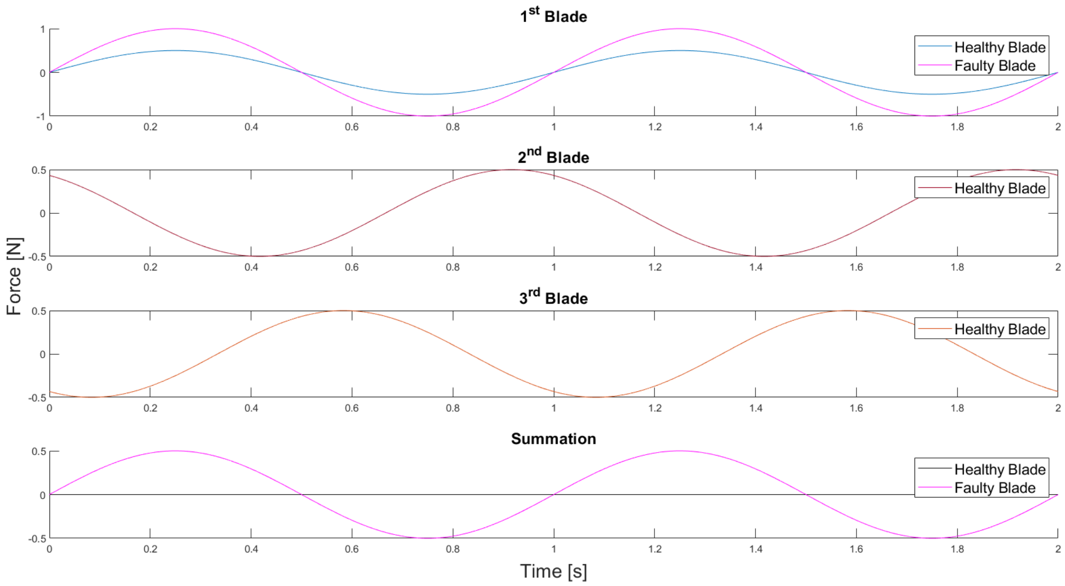

Figure 2.5: 1P Force Harmonics Produced by Each Blade Due to Tower Shadow Effect [11]

However, in a rotor where the first blade has a fault, the resulting 1P force harmonic of the first blade may be produced with a higher amplitude than the second and third blades, which are healthy. Subsequently, when the three 1P blade harmonics are added, they do not cancel out anymore, resulting in detectable 1P force signals.

2P Harmonic

The origin of the 2P harmonic could potentially be explained with similar reasoning to the origin of the 1P harmonic. The load fluctuation occurs twice per rotation when the blades experience uneven loading, due to aerodynamic or gravitational effects. The same principle holds, where the second and third blades are shifted 1/3 and 2/3 of rotor revolution later than the first blade, respectively. This is shown in Figure 2.6. In a healthy rotor, the three blade harmonics are out of phase, so the total force at the hub would equate to zero, after the three harmonics are added. However, if one blade is faulty, similar to the 1P harmonic example, the total force at the hub would not cancel out anymore, resulting in 2P force signals.

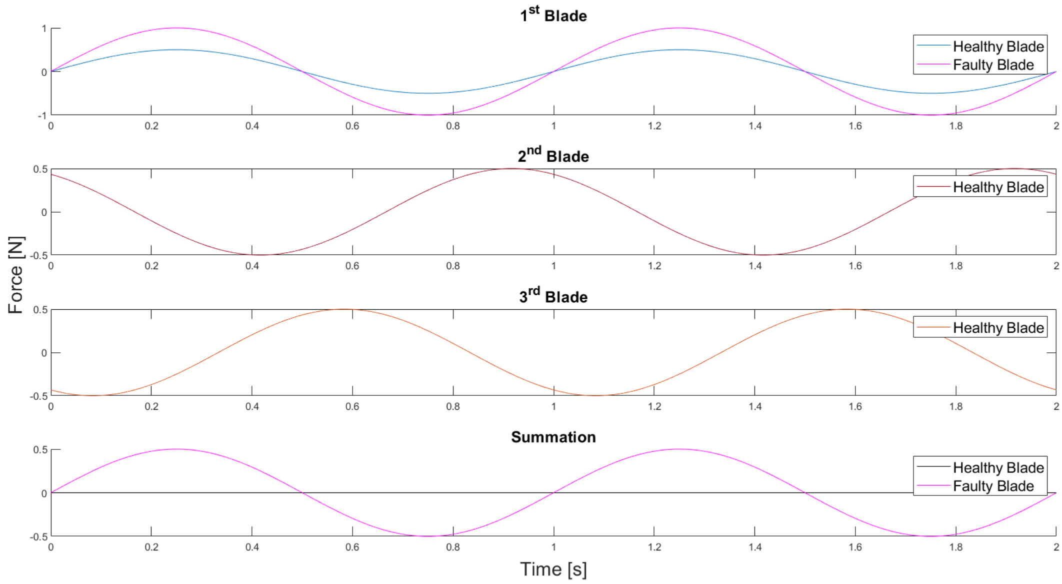

Figure 2.6: 2P Force Harmonics Produced by Each Blade Due to Tower Shadow Effect [11]

Another possible origin of 2P harmonics could from a pitch misaligned blade, which causes low speed shaft (LSS) displacements [14]. A. Heege and J. Hemmelmann argue that when one of the blades is incorrectly pitched, then that blade would meet the wind at a skewed angle of attack, resulting in a higher lift-to-drag ratio, following the explanation from subsection 2.1.2. Figure 2.7a shows a visual representation of a pitch misaligned blade at four different time instances, quarter of a revolution apart: A, B, C and D, where the misaligned blade is numbered 1 and the two healthy blades are numbered with 2 and 3. Figure 2.7b shows the rotor azimuth over time at rated rotation speed of 9.6 RPM, over two full rotor revolutions in the clockwise direction.

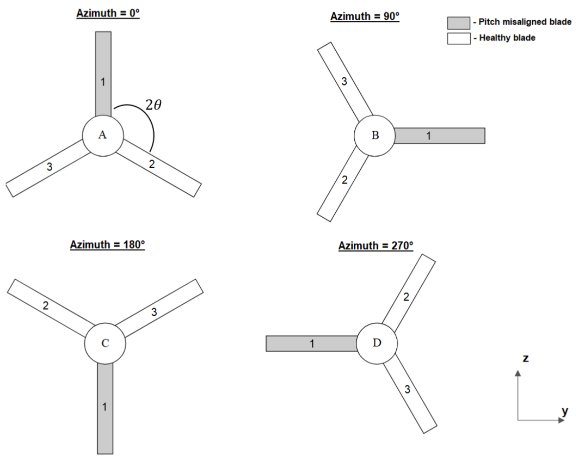

(a) Pitch Misaligned Blade Position

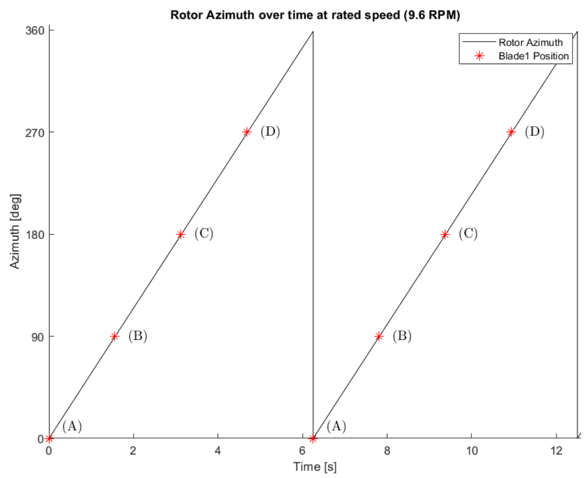

(b) Rotor Azimuth Over Time

Figure 2.7: Pitch Misaligned Blade Position Over One Rotational Period

The thrust force generated by the misaligned blade, acting in the x direction in reference to Figure 2.7a, is transferred onto the LSS, resulting in displacement. In Equation 2.11, F_1, F_2 and F_3 denote the thrust produced by blades 1, 2 and 3, respectively. The extra thrust produced by the misaligned blade is denoted by Δf, resulting in a higher force in blade number 1 than in blades 2 and 3. Peak displacement occurs four times in one revolution of the rotor, twice in the z axis in rotor positions A and C, as well as twice in the y axis in rotor positions B and D. Therefore, this could result in 2P harmonic peaks in moment in the y and z directions, as the maximum displacement occurs twice in each direction.

$$|F_1| = F + \Delta f \quad \text{and} \quad |F_2| = |F_3| = F \tag{2.11}$$

In reference to rotor position A from Figure 2.7a, Equation 2.12 shows the moment balance in a faulty rotor, where M_1, M_2 and M_3 denote the moments produced by blades 1, 2 and 3, respectively, while L denotes the distance from centre of rotor and 2θ denotes the angle between two blades. Since thrust is a distributed load, multiplying it by the distance from centre of rotor would result in a moment at the root of the blade, which will be translated onto the LSS due to the coupling in the hub.

In position A, blade 1 produces a moment about the y-axis, since the blade is at a right angle to the fixed reference y-z axis in the figure. Blades 2 and 3, however, produce a moment at an angle with respect to the fixed y-z axis, resulting in a partial moment about the z-axis. Since the blades are equally spaced between each other, θ is equal to 60°, equating the cosine term to 0.5. This ultimately results in a moment imbalance in the LSS of ΔfL, or ΔM_y, which also occurs in position C with a negative sign, due to symmetry. Subsequently, a moment peak about the z-axis occurs in rotor positions B and D, following a similar derivation as in Equation 2.12. Furthermore, it is worth noting that the sum of all moments would equate to 0 in a healthy rotor, since the Δf term would be equal to 0, resulting in no 2P peaks in the output.

$$\begin{aligned}
M_1 &= M_y + \Delta M_y = (F + \Delta f)L \\
M_2 &= -M_y \cos\theta - M_z \cos\theta = -FL\cos\theta - FL\cos\theta \\
M_3 &= -M_y \cos\theta + M_z \cos\theta = -FL\cos\theta + FL\cos\theta \\
\Sigma M &= M_1 + M_2 + M_3 = (F + \Delta f)L - 2FL\cos\theta \\
\Sigma M &= \Delta f L = \Delta M_y
\end{aligned} \tag{2.12}$$

where $\theta = 60°$

3P Harmonic

Unlike 1P and 2P harmonics, 3P harmonics produced by each blade are all in phase. This is because the harmonics have period that is three times shorter than 1P harmonics, so when the harmonic is shifted by 1/3 of blade revolution for subsequent blades, it results in the exact same harmonic, as seen in Figure 2.8. As a results, the total force sum at the hub would not cancel out, like in the previous examples. This means that healthy rotors also produce 3P harmonics. Furthermore, if one of the blades is imbalanced and produces a higher amplitude harmonic, the total force at the hub would also be larger.

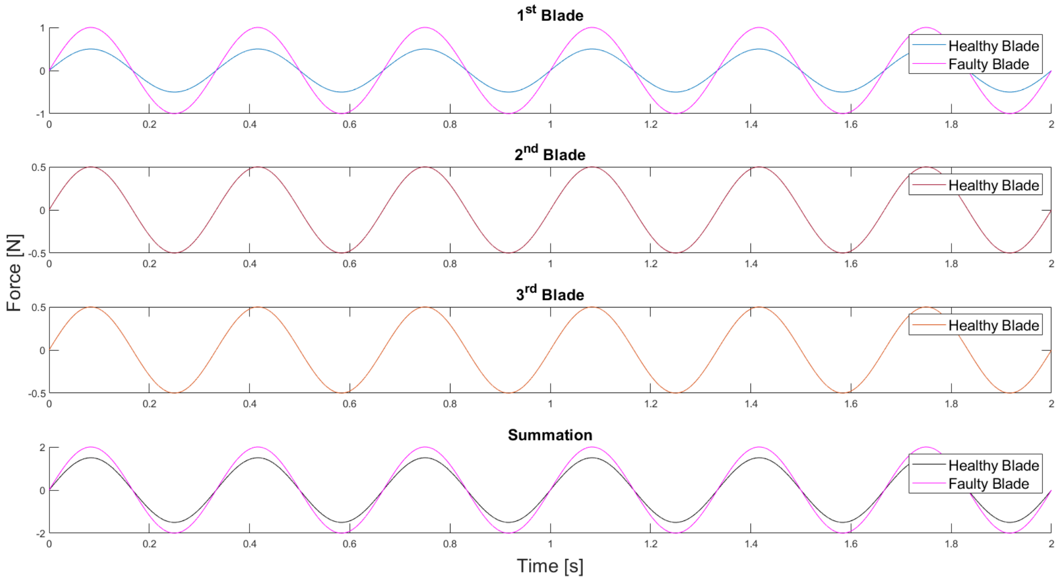

Figure 2.8: 3P Force Harmonics Produced by Each Blade Due to Tower Shadow Effect [11]

2.3. Current Fault Detection Techniques

Detecting faults in WTs requires information about the turbine in some form. After which, this information needs to be thoroughly analysed to see whether there are any deviations from a healthy turbine. Lastly, if a problem is detected, the problem type needs to be characterised, in order to fix it. This chapter will present different fault detection techniques found in literature, including the way WT data is gathered, how the data is analysed and how data analysis can be used to diagnose what type of fault is present.

2.3.1. Data Collection

Data collection is logically the first step in detecting a fault in a WT. There are many ways data can be collected from a wind turbine. For instance, readings from sensors located in different parts of the turbine: strain gauges, accelerometers, anemometers (mechanical or ultrasonic), thermometers and more [15]. Sensor readings provide a rich set of information about performance of different parts of the WT, providing WT operators remote access to status of specific components remotely and giving them the ability to analyse the data using various techniques.

One of the most common data collection methods found in literature is using the Supervisory Control and Data Acquisition (SCADA) system. SCADA is used for remotely controlling, real-time monitoring and analysing different parts of systems, both in and outside of the wind industry. SCADA architecture is build around sensors and other hardware components installed on site, and software that allows the collected data to be transferred to the system operator [16, 17]. A key advantages of using SCADA architecture for WT monitoring, is the fact that data is collected in real-time and remotely, with the ability to send control commands back to the WT by the operator.

Another way WT data is collected is visually and accoustically. Visual data can be collected through various methods, such as in-person inspections, drones, or fixed cameras [7–9]. While the biggest advantage of visual data is that some issues like surface cracks or blade delamination are immediately apparent, there are types of faults that are challenging to identify visually, such as rotor imbalances. On the other hand, acoustic detection methods use sound data collected from microphones to detect issues not visible to the naked eye. For example, the sound produced by a faulty component, such as blade fibre breakage or a faulty bearing, could differ in frequency from a healthy component [18, 19].

Overall, various collection methods can be used to detect issues present in the WT. After collecting the data, however, it still needs to be processed and analysed, in order to determine whether a fault is present or not.

2.3.2. Data Analysis and Fault Diagnosis

Data analysis is an important step in detecting faults in WTs, since in many cases data cannot show problems on its own, without proper manipulation and analysis. There are many different methods to analyse SCADA sensor data in literature. One popular method found in recent literature is using Machine Learning (ML) to analyse trends in data. ML utilizes characterised historic WT data and finds patterns and trends related to faults. ML models are then able to cross-examine uncharacterised data with historic data, and determine whether a fault is present or not [17]. Additionally, patterns leading to faults could potentially be identified using early warning systems, resulting in faults being detected as early as possible, before they can cause more damage or component failure [20].

Another common method is vibration analysis, which is used both in and outside the wind industry [21]. Vibration signals obtained from sensors can be analysed both in time and frequency domains, to obtain useful information about the health and performance of components, as well as be used for modal analysis of the structure [6, 9, 11, 22]. Low frequency load fluctuations in the LSS are commonly caused by rotor imbalances, and is the main data analysis method used in this thesis, therefore this is further discussed in section 2.2.

On the other hand, qualitative data analysis is inherently difficult to analyse mathematically, unlike signals. In person inspections, drone and camera footage require a specialist to visually identify and determine whether there is a visible problem that could potentially cause damage to the WT [8]. Alternatively, recent literature shows trends in analysing image data using ML image processing techniques, specifically for blade surface damage detection, such as cracks and delamination [23–26].

Lastly, fault diagnosis is the final step in characterising WT faults. The most common way of diagnosing WT faults found in literature is cross-examining analysed data with historic data [27, 28]. For instance, if a fault has been producing a certain system response historically, and if the same system response shows up in the data of the WT in question, then the chances are high that the same fault is present. Historic data is especially useful for training of many ML based fault diagnosis methods, many of which rely on this approach.

2.4. Most Common Rotor Imbalances

WTs are large dynamic structures that experience heavy variable loads and harsh operating conditions. Operating under such extreme conditions, WTs may experience certain degrees of wear, damage faults, especially in the rotor and the drivetrain. These faults carry various risks for the WT and may result in additional component wear, damage or failure. This chapter focuses on identifying the most common types of faults that can occur in the rotor. Additionally, the effects and risks of these faults on the turbine's operation are described, and statistics on occurrence rates are presented.

2.4.1. Pitch Misalignment

As was mentioned in section 2.1, the orientation of the blade with the respect to the resultant wind vector is crucial, as both the lift and drag coefficients are a function of the angle of attack. Pitch Misalignment (PM) is a type of rotor fault, where one or more blades are not orientated as intended by the design [6, 29]. PM may be caused by defects during manufacturing, incorrect installation of the blade, or incorrectly tuned or faulty pitch controller. Regardless of the cause, PM may result in a variety of issues for the WT, such as: lower power generation, fluctuating dynamic and aerodynamic loading, excessive drivetrain component wear and more. Ultimately, problems with PM of the blades could lead to component damage or in some cases failure, as well as introduce additional O&M costs, performance issues and potentially reduce the turbine's lifetime.

In a study on rotor imbalance detection methods by Kusnick et. al. [22], researchers have modelled PM in one of the blades, where PM severity was varied by increasing the pitch angle from 0^o, all the way up to 25^o. The results showed a significant increase in low speed shaft (LSS) bending moments and shear forces. The trends of the results have also shown an increase in LSS loads along with PM severity, which can clearly be seen in Figure 2.9. In another study, following the work of Kusnick et. al., F. C. Mehlan and A. R. Nejad [6] have modelled PM in a similar way, to see the effect different wind speed conditions would have on the turbine, at different degrees of PM severity. The results have shown a similar tendency of increased shear forces and bending moments in the LSS, both at higher wind speeds and degrees of PM severity.

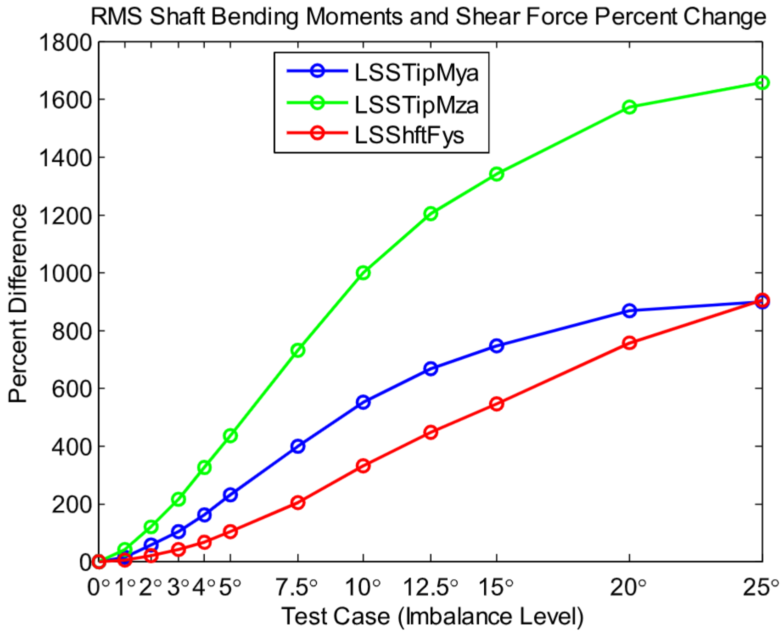

Figure 2.9: Effects of pitch misalignment on LSS loads [22]

According to Germanischer Lloyd (GL) guidelines for the certification of wind turbines, a PM of $\pm 0.3°$ is considered an acceptable range of deviation and should be considered in the design [30]. An empirical study on effect of PM on WT lifetime showed that 38% of turbines that have been measured were outside of this range [31], and have concluded that PM may cause reduced turbine lifetime and reduced annual energy production (AEP). This implies that PM is a rather common issue in WTs and has largely went undetected before measurements were taken for this study.

2.4.2. Mass Imbalance

Another common type of rotor fault is blade mass imbalance (MI). MI is caused by uneven mass distribution along the blades of the rotor, which can occur for a variety of reasons, such as: manufacturing defects, dirt, ice or moisture build-up on the surface, cracking or moisture build-up in the cracks [22, 32]. A perfectly balanced rotor would have its centre of rotation exactly at the centre of the rotor, exerting an even amount of thrust directly at the centre. However, and mass imbalanced rotor would have its centre of mass shifted towards the blade with higher mass. This shift in the centre of mass essentially causes additional gravitational and centrifugal forces at the new centre of mass. This in turn results in constant 1P harmonic loads in the LSS in rotating frame of reference and periodic 1P harmonic loads in the LSS in fixed frame [6, 11, 33]. Figure 2.10 shows an example model of MI, where it was represented by a point mass in one of the blades. Here, gravitational force F_G and centrifugal force F_c are caused by the point mass m.

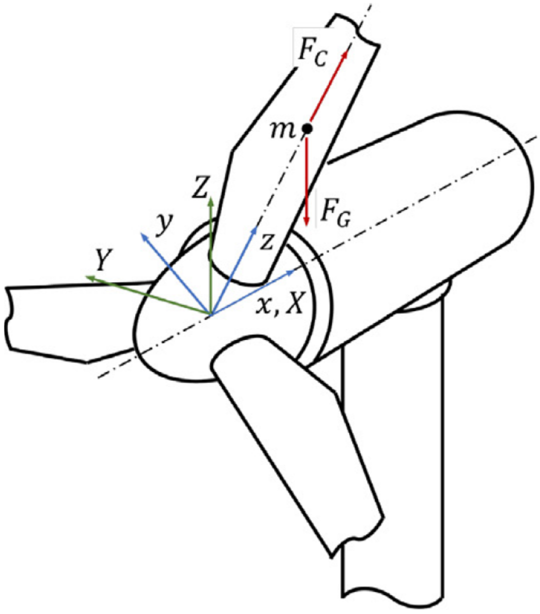

Figure 2.10: Rotor mass imbalance forces caused by a point mass in one of the blades, in rotating (x,y,z) and fixed coordinate frame (X,Y,Z) [6]

F_c, is proportional to the square of angular velocity of the rotor, ω, as per Equation 2.13. This means that below rated wind speeds, F_c increases with wind speed, since the rotor revolves faster at higher wind speeds. Above rated, on the other hand, the controller pitches the blades to stall to protect the rotor from overloading, resulting in constant rotation speed regardless of wind speed, given the wind speed is above rated. This means that the loads produced in the LSS due to centrifugal force above rated wind speeds will be larger than at below rated speeds, but remain constant until cut-off.

$$F_c = \frac{mv^2}{r} = m\omega^2 r \Rightarrow F_c \propto \omega^2 \tag{2.13}$$

According to a study [34], only 27% of 383 WTs were balanced within the IEC 61400-1 standards, with 29% of all turbines containing MI. This shows that MI is also a significant rotor balancing issue, similarly to PM which was discussed previously. Considering constant and periodic loads caused by MI on the LSS, as well as the issue being rather common, MI may result in component wear, damage or in some cases failure, if not detected in due time.

2.4.3. Yaw Misalignment

As mentioned in subsection 2.1.2, the angle at which wind interacts with the blade has a significant impact on the health of the rotor, drivetrain components and AEP of the WT. If the inflow wind in Figure 2.2 would come from a different direction, the angle of attack would change, which would directly impact lift and drag generated by the blade. To account for wind direction change, a yaw mechanism is present in all WTs, the purpose of which lies in rotating the rotor about its Z-axis, in reference to Figure 2.10, to meet the inflow wind at an optimal angle [6, 35, 36]. In literature, this type of misalignment is commonly referred to as yaw misalignment (YM) or yaw error, since the rotor and the wind are not properly aligned.

YM can be caused by a variety of factors, ranging from improperly tuned controller to frequent wind direction changes due to turbulence and wind direction reading errors from the sensor [35]. Furthermore, most wind turbines are designed to have a certain degree of tolerance of YM, in order to protect the yaw system from excessive wear. This is done to account for frequent changes in wind direction, sacrificing turbine efficiency to extend yaw system service life [6, 35].

The main effect of YM is a change in aerodynamic forces at the rotor. This change, in turn, may cause significant problems in the rotor and further down the drivetrain, including blade and drivetrain component fatigue and variations in power generation. Moreover, it has been shown that at larger degrees of YM, the output power curve fluctuates more, while also causing the average power output to suffer. Similarly, higher degrees of YM have also induced oscillations into the mechanical torque output curve [36]. Not only is this an issue for the LCOE, since power production is lower, but can also add unforeseeable costs towards O&M of turbine components. Similarly to other types of rotor imbalance mentioned previously, YM may also cause WT components to fail prematurely, resulting in further down-times and expensive component replacements.

2.5. System Integration and Socioeconomic Impact

This section aims to identify the socioeconomic impact of new WT fault detection techniques being developed and utilised in real wind parks. First, the most important stakeholders are analysed and ranked based on their power-interest levels. Next, financial aspects such as LCOE, component failure and time to repair are analysed, based on results found in literature.

2.5.1. Stakeholder Analysis

Every new technology aims to enter the market, there are a number of different stakeholders who have a certain degree of interest in said technology. New methods of detecting and charactering faults in the rotor of a WT concern many various groups of people in the energy industry, both directly and indirectly. Each stakeholder has a certain degree of interest in the new technology, while also having a certain degree of power and influence over it entering the market. Based on stakeholders' relative interest and power levels, they can be categorised into one of the four groups:

- **Context setters** are high power, low interest group of stakeholders. These stakeholders are very influential on new technology integration, but are not interested in all the details. These stakeholders need to be satisfied at all times, as well as being informed to some extent.
- **Players** are high power, high interest stakeholders. These stakeholders' interests coincide with what the new technology is trying to achieve, while also having influence on whether this technology is successful or not. The players should be satisfied and communicated with at all times, as they are the most important stakeholders.
- **Subjects** are low power, high interest stakeholders. There stakeholders do not have much power over whether or not the technology succeeds, however they may still hold interest towards this technology, as it may impact them in one way or another. The subjects should be well informed on the topic.
- **Crowd** are low power, low interest stakeholders. These stakeholders are neither very interested, nor very influential in relation to the new technology. Communication with these stakeholders is not crucial, but still desirable to a some extent.

Below, a list of seven most relevant stakeholders, related to remote rotor fault identification and characterisation methods, can be seen. Additionally, Figure 2.11 maps each stakeholder onto a Power-Interest grid, to represent to group each stakeholder falls into.

- **Transmission System Operator (TSO)** are responsible for keeping the electricity grid balanced to prevent power outages and grid failures [37]. Due to inconsistent energy generation of WT, the grid may experience fluctuations. TSO may have moderate amounts of interest in making WTs more reliable and having shorter repair times to reduce grid fluctuations[17]. However, TSO does not have power over which source the energy comes from, as their tasks are limited to transmitting energy from any source to the consumer, making them a crowd type stakeholder.
- **Standard Development Organisations (SDOs)** are independent regulatory bodies that are responsible over developing standards on technology, to ensure that the end result is efficient, of high quality and safe to use. Unlike the government, SDOs have power over deciding whether a technology follows the regulations, such as IEC-61400 [30, 38]. SDOs have high interest in new WT monitoring technologies to, since standards and regulations need to be updated constantly, to ensure safety and high performance. SDOs have the most power over which technology will be the next standard for WT design, making them a player type stakeholder.

- **Wind Farm Operators** ensure the wind farm runs optimally by monitoring WT operation and providing maintenance to the WTs [39]. Having more advanced WT monitoring tools could benefit farm operators by increasing work efficiency and improving WT downtimes. Additionally, having shorter and less frequent maintenance cycles would reduce the time WT technicians spend harnessed to the turbine, reducing the risk of injury for the technicians. This makes them moderately interested in this technology, but overall they have little decision making power when it comes to new technologies entering the market, putting them into the crowd category.

- **WT Engineers and Companies** are responsible for design and manufacturing of WTs. With new monitoring tools and techniques, WT engineers will be abele to account for such tools during the design phase. Furthermore, the companies could benefit from having latest technologies in their WTs, making the market more competitive. The companies and engineers have high interest in having a larger renewable energy market share by making their WTs more reliable and serviceable. Moreover, they have moderately high power of freedom when it comes to technology implementation in their design, which is limited by regulations and costs, making them a player type stakeholder.

- **WT Technicians** provide on-site service to WTs, such as inspection and maintenance. The ability to detect and characterise rotor faults rotor remotely could save time and improve accuracy, simplifying the task. Additionally, spending less time on-site would increase the safety of the working environment and potentially increasing demand in this field of work [40]. This shows that WT technicians have high amounts of interest in increasing their work environment safety, but have low amounts of power in making this technology becoming a standard, putting them into the subject stakeholder bracket.

- **Investors** are an important stakeholder in the wind energy industry. Large wind park projects require millions of dollars in upfront costs, therefore investors are required. Since WTs are infamous for having reliability issues and having high maintenance cost [41], making them a high risk investment. Improving reliability of turbines with new fault detection and characterisation techniques could increase the willingness of investors to finance these projects. Ultimately, investors are the most interested stakeholder in reliability improving technologies, while also having the highest power due to their financial leverage role in the market, making them a player type stakeholder.

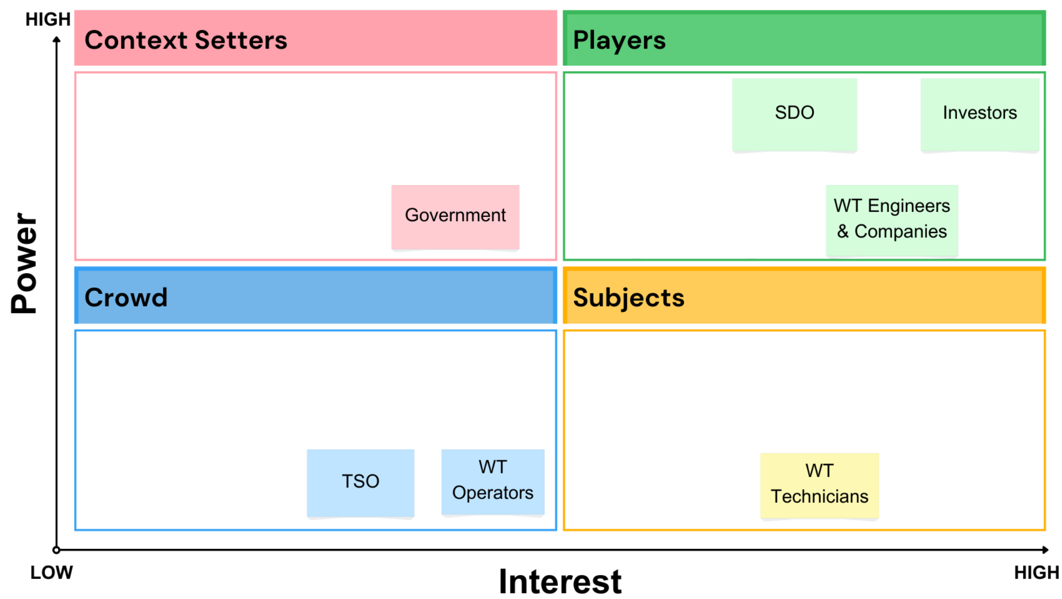

Figure 2.11: Stakeholder Power-Interest Grid

2.5.2. Financial Aspects of Maintenance

WTs and wind parks are complex and expensive structures to design, install and operate. Over their lifetime, WT require regular maintenance for different components, in order to reduce the risk of component failure. Given that WT site locations are often remote and difficult to access - such as mountainous areas, fields and offshore - providing inspections, maintenance and repairs to the turbine is logistically difficult and time consuming. This chapter will provide insights on the financial aspects of maintenance in terms of LCOE statistics, time to failure (TTF) and time to repair (TTR).

Levelized Cost of Electricity

As previously mentioned, LCOE is a metric used to quantify the average cost of electricity produced over the energy source's lifetime. The aim of the wind industry as a whole is to minimize the LCOE of wind energy, which could be done by reducing the CAPEX and O&M, as well as increasing WTs' efficiency and lifetime. From NREL's cost of wind energy review in 2021, it can be seen how the LCOE of wind energy is distributed [41]. In their study, NREL analyse real world wind industry data to provide the cost breakdown of onshore and offshore WTs, as well as compare their findings to historic data.

Figure 2.12 and Figure 2.13 represent levelized cost breakdown for onshore and offshore wind plants respectively. Immediately, it can be seen that the LCOE of an offshore plant is 2.3 times larger than the LCOE of onshore plant. The increase in LCOE comes from a myriad of factors, which mostly come from structural, electrical and installation difficulties in the sea, as well as other financial CAPEX factors. Additionally, the O&M costs more than double for offshore plant, primarily due to logistical reasons, like the requirement of a sea vessel and specialized equipment. Overall, it can be seen that regardless of the site, around 30% of the LCOE of wind energy comes from O&M costs.

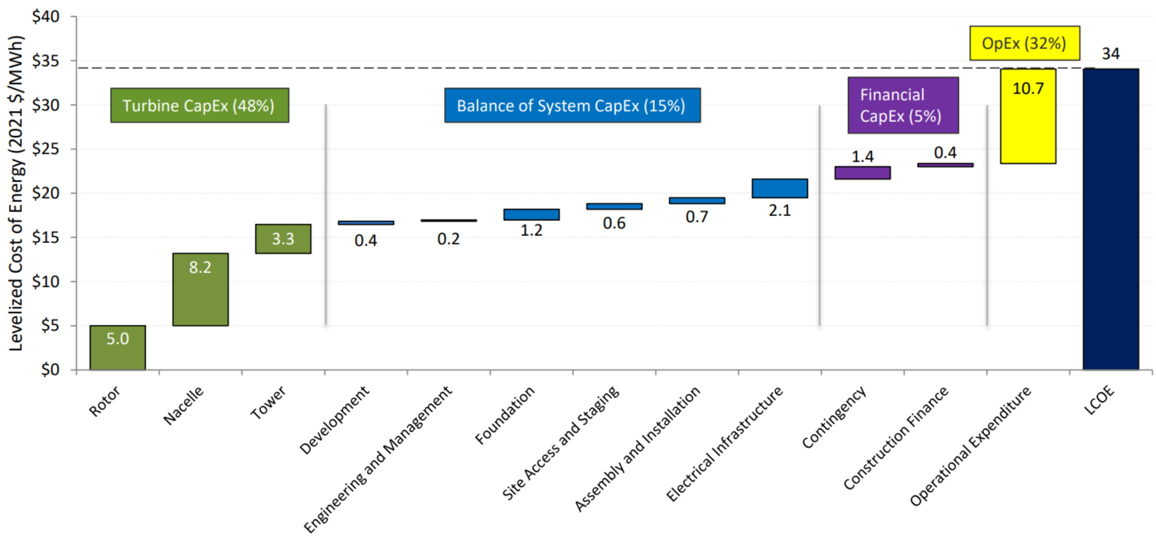

Figure 2.12: Levelized Cost Breakdown for Reference Land-based Wind Plant [41]

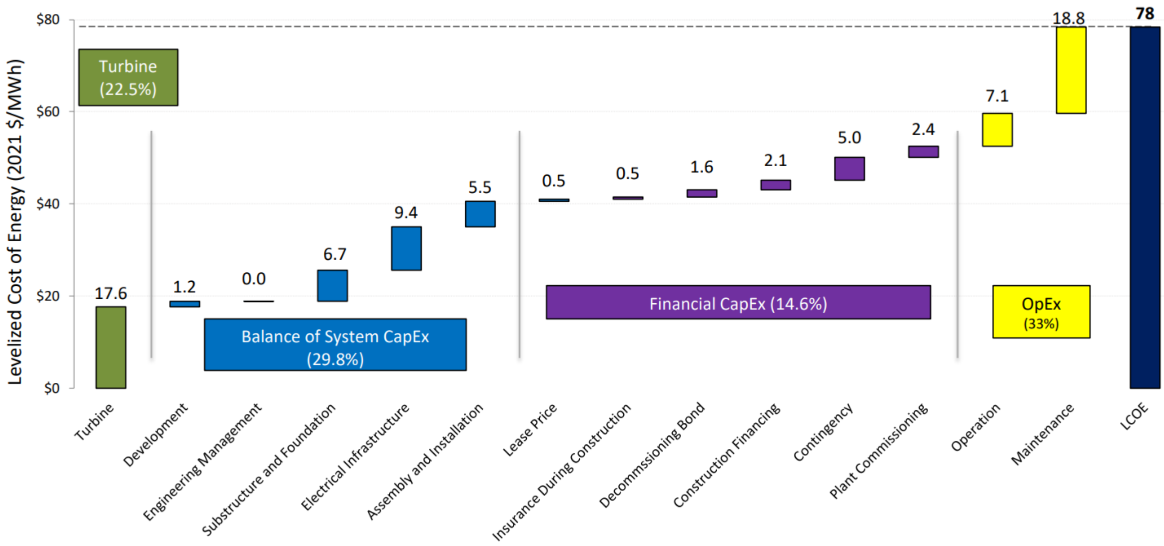

Figure 2.13: Levelized Cost Breakdown for Reference Offshore-based Wind Plant [41]

Furthermore, the US department of energy, in consensus with the Government Performance and Results Act (GPRA), aims to gradually decrease the LCOE of wind energy over the years [42, 43]. Figure 2.14a and Figure 2.15a show the historic reduction in LCOE of wind energy in comparison to goals set by GPRA, for onshore and offshore wind energy, respectively. It can be seen that between years 2016 and 2022, the LCOE of wind energy has significantly decreased for both on and offshore wind energy.

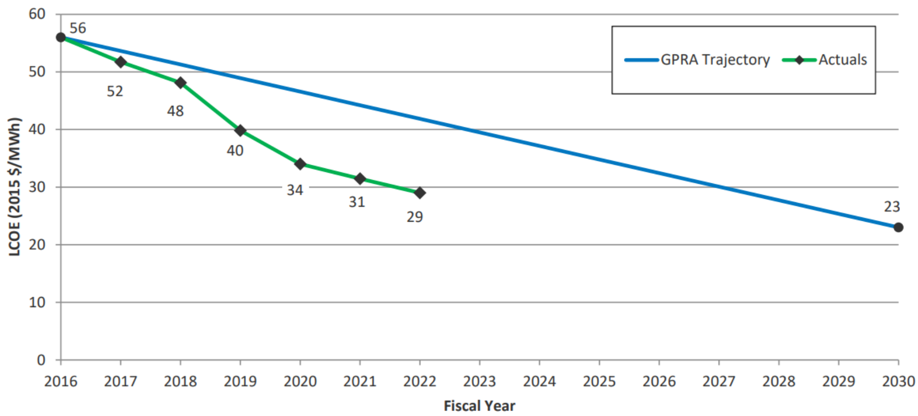

(a) GPRA Pathway vs Historic Data

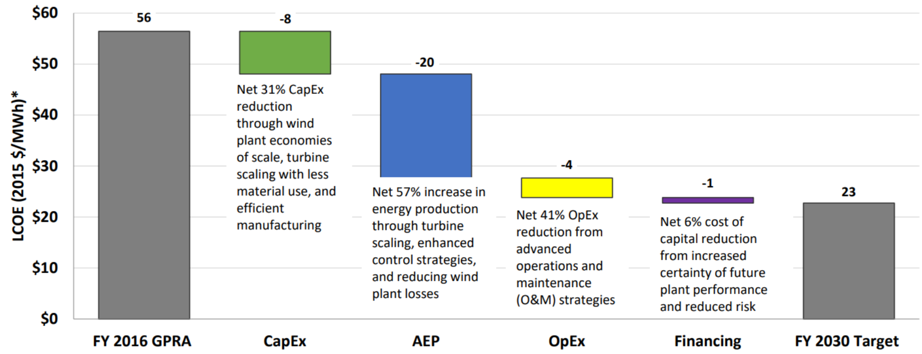

(b) LCOE Reduction by Source

Figure 2.14: GPRA Cost Reduction Pathway From 2016 to 2030 for Onshore Wind Energy [41]

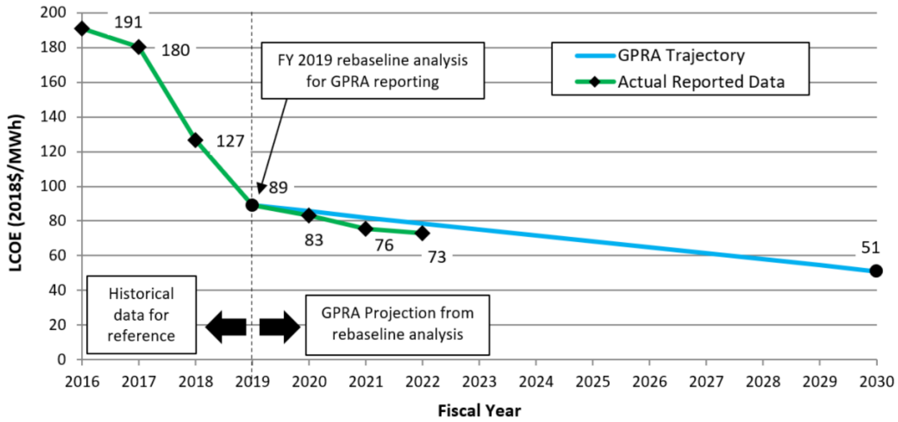

(a) GPRA Pathway vs Historic Data

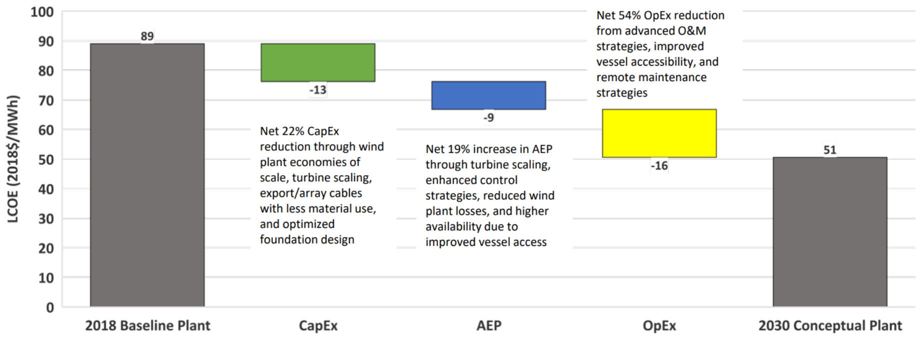

(b) LCOE Reduction by Source

Figure 2.15: GPRA Cost Reduction Pathway From 2016 to 2030 for Offshore Wind Energy [41]

Overall, it can be seen that O&M comprises a large part of the total LCOE of the WT of about 30%. The goals to reduce O&M costs by 41% and 54% for on and offshore wind, respectively, by utilising more advanced WT service and monitoring techniques, shows the importance of researching new ways to improve O&M procedures as a whole. Remote fault characterisation could potentially improve the logistics involved in servicing WTs and help reduce O&M costs both on and offshore.

Component Failure and Time to Repair

Component failure in WTs are rather common occurrences, which can lead to prolonged downtimes and reduced AEP, further component failure and additional variable costs for O&M. Detecting a problem as quickly as possible can reduce component failure rate and decrease service time and overall downtime of a WT [44–46].

In a study by S. Oztunk and V. Fthenakis [44], real world WT data was analysed to predict the frequency, TTR and costs of WT failures, using ML. Their study looked at various factors that could affect failure rates, TTR and time to failure (TTF), such as environmental conditions and previous failures in the WT. Additionally, WTs with gearbox drive were compared to direct drive WTs. Figure 2.16 shows the probability of failure over operation time in WTs with the total number of previous failures between 0 and 20, and WTs with more than 21 previous failures. Here, G denotes gearbox type and D denotes direct drive type of WT. It can be seen that for all cases, the longer the WT operates, the higher the probability of failure is, which supports the idea of having regular maintenance.

Moreover, it shows that WTs with higher number of previous failures tend to have a higher probability of failure, regardless of drivetrain type, which shows the importance of detecting issues in the rotor before they cause a failure. It is worth noting that the type of failure was not specified in this study, meaning it is unknown whether the previous failures refer to failures of the same type or any type of failure.

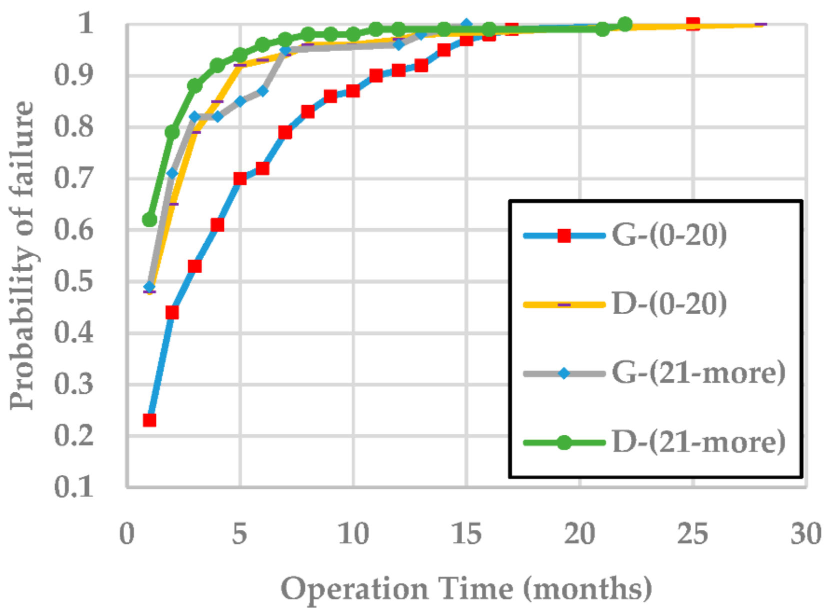

Figure 2.16: TTF Probability based on number of previous faults [44]

Higher TTR directly impacts the LCOE of the WT in two ways. First, is higher TTR means higher downtime, resulting in lower AEP. Second, Higher TTR means WT technicians would need to be compensated for longer working hours, making maintenance more expensive. Based on the results of this study, it is clear that preventing failures before they occur can save money on maintenance and produce a higher AEP .

3

Methodology

In this chapter, the methodology used in this thesis is presented. Section 3.1 describes the modelling setup used to simulate rotor imbalances, at different environmental conditions, as well as explains how the simulation software works. Section 3.2 explains how the data obtained from simulations is processed, analysed and presented.

3.1. Modelling Setup

In this section, the modelling setup is discussed. Background information about the WT used in the model and simulation software used is given. Moreover, fault cases are presented, along side environmental cases, output parameters and other parameters varied in the simulation software. Lastly, the simulation initialisation process is described and explained.

3.1.1. DTU 10 MW Reference Wind Turbine

Today, the wind energy sector shows growth tendencies not only in terms of installed capacity, but also in WT size. In response to the increase in global demand for larger turbines [47, 48], the DTU 10 MW horizontal axis wind turbine was modelled in this research, since this reference turbine is very well documented and is extensively used in literature. Design parameters of the turbine are summarised in Table 3.1.

Table 3.1: Design parameters of DTU 10 MW reference turbine [49]

Parameter	Value	Units
Name	DTU 10 MW RWT	—
Rated Power	10	MW
Rotor Diameter	178.3	m
Hub Height	119	m
Number of blades	3	—
Cut-in, Rated, Cut-out Wind Speed	4.0, 11.4, 25.0	m/s
Cut-in, Rated rotor speed	6.9, 9.6	RPM
Drivetrain	Medium speed gearbox	—
Control	Pitch regulated, variable speed	—

3.1.2. OpenFAST Modules and Fault Cases

Modelling of rotor faults has been carried out in OpenFAST, an open-source WT simulation tool [50, 51]. OpenFAST combines computational modules for aerodynamics, hydrodynamics, control and electrical servo-dynamics, and structural dynamics to simulate the dynamic response of a WT in response to user-defined initial conditions. The 10 MW DTU reference WT model was imported into OpenFAST simulation tool. Modelling of PM, MI and YM rotor imbalances, which are discussed in section 2.4, is done based on methodology seen in the paper by F.C. Mehlan and A.R. Nejad [6], where certain design parameters are varied to simulate healthy and faulty cases in OpenFAST. For this, three OpenFAST modules need to be considered, namely: AeroDyn, ElasoDyn and ServoDyn. This chapter will provide an overview of each of the three modules and how they are used to simulate rotor imbalances.

AeroDyn

The AeroDyn module is responsible for calculating aerodynamic loading on the turbine's blades and tower. It operates based on the principles of steady BEMT, discussed in 2.1, as well as dynamic BEMT [51]. AeroDyn performs the calculations by dividing each blade into smaller elements, while taking into account environmental conditions, such as wind speed and direction, as well as turbine's properties, like geometry, blade velocity and position at each time-step of the simulation. This results in high resolution and high accuracy calculations of lift, drag and pitching moments of each blade element [52].

In this thesis, the AerDyn module is used to alter the pitch angle of one of the blades, in order to model pitch misalignment, based on [6]. Since there is no direct way of changing the pitch angle of a blade, PM is modelled by uniformly changing the twist angle of one of the blades along its entire length, which is geometrically similar to changing the pitch of the blade. Blade twist is changed in one blade only, by increasing the value of the twist by 1, 2 or 3 degrees, respective to three levels of PM severity, PM1-PM3.

ElastoDyn

The ElastoDyn module is responsible for calculating system's kinematic properties, such as linear and angular positions, velocities and accelerations of key structural points of the WT, while also providing these properties in different frames of reference [51]. The calculations are computed based on user defined turbine geometry, component masses and inertias, degrees of freedom and initial conditions. In addition, system dynamics are calculated based on a linear spring-damper model.

In this thesis, ElastoDyn is used to model two cases. Firstly, it is used to model the MI case. MI is modelled by considering one of the blades to have a uniformly higher mass than the other two blades. This could, for instance, represent a blade with a uniform layer of ice. The mass density of one blade is therefore increased by a factor of 0.58%, 0.88%, and 1.17%, respective to three levels of MI severity, MI1-MI3. Secondly, ElastoDyn is also used to model YM. YM is simply modelled by changing the nacelle-yaw angle initial condition by 5, 10 and 15 degrees, respective to three levels of YM severity, YM1-YM3. Additionally, yaw degree of freedom has to be enabled, for ElastoDyn to consider the change.

ServoDyn

The ServoDyn module is essentially a virtual controller responsible for controlling various parts of the turbine, such as blade pitch, generator torque, high speed shaft brake and nacelle yaw [51, 53]. This module allows communication between other modules by analysing inputs from them and returning control outputs necessary for realistic simulation of WT operation. In this thesis, ServoDyn input settings are only altered when modelling YM.

InflowWind

InflowWing is a module responsible for processing input wind field data[50]. With each time-step, the module receives coordinates calculated by different modules in the FAST glue code, and returns the undisturbed wind-inflow velocities at these positions [54]. The velocity is calculated as a function of input coordinate positions and internal time varying parameters, set by the user. For this experiment, the InflowWind file is modified every time wind speed and turbulence seed is changed.

Overall, three OpenFAST module input settings are altered in order to simulate the three cases of rotor imbalance, namely: PM, MI and YM. Each case of rotor imbalance is modelled with three degrees of imbalance severity, that is pitch angle increase for PM, blade mass density for MI and yaw angle for YM. The imbalanced rotor cases are compared to a healthy rotor case, where parameters are set to factory settings. Table 3.2 provides a summary of fault cases simulated in this experiment.

Table 3.2: Fault cases for each type of rotor imbalance.

Imbalance Type	Case									
	Healthy	MI1	MI2	MI3	PM1	PM2	PM3	YM1	YM2	YM3
Mass Imbalance [%]	0	0.58	0.88	1.17	0	0	0	0	0	0
Pitch Misalignment [deg]	0	0	0	0	1	2	3	0	0	0
Yam Misalignment [deg]	0	0	0	0	0	0	0	5	10	15

3.1.3. Environmental Cases

In this experiment, environmental conditions are also varied. In the real world, environmental conditions are rarely consistent on larger time scales. Therefore, in order simulate more realistic and meaningful results, each fault case is run at six different wind speeds. Moreover, two types of wind conditions are considered - steady and turbulent wind.

Steady Wind

Steady wind is uniform by nature. In steady wind, both flow speed and direction remain constant over long periods of time, but still varies with height due to wind shear. Steady wind is a simplified wind model and is not a realistic representation of real world wind conditions. However, not including wind speed and direction fluctuations in the simulation will allow for a clearer look of what effect rotor imbalances have on the rotor. Additionally, steady wind simulations require less computational power for aerodynamic calculations, resulting in quicker but less accurate simulations [55]. Steady wind is simply simulated by selecting steady wind option in the inflow wind file in OpenFAST.

Turbulent Wind

Turbulent wind, on the other hand, is far more complex than steady wind, and is a closer representation of wind found in the real world environment. Unlike steady wind, turbulent wind is stochastic in nature, with both speed and direction continuously changing in a random manner. There are two main contributors to turbulence, one being friction caused by the Earth's surface. And the second being the thermal gradients, causing movement from hot to cold [56].

Normal turbulence model (NTM) is used to calculate turbulence intensity factor for each wind speed. NTM is a standardised approach in WT design to represent typical atmospheric conditions a WT may experience, which is defined by IEC 61400-1 wind turbine design standard [57]. For calculations of turbulence intensity factor, I, Equation 3.1 was used, where I_{ref} is the expected value of the turbulence intensity at 15 m/s, V_{hub} is the 10-min averaged wind velocity at hub height and σ is the standard deviation of longitudinal wind velocity.

$$I = \frac{\sigma}{V_{hub}} = \frac{I_{ref}(0.75V_{hub} + 5.6)}{V_{hub}} \tag{3.1}$$

The value for I_{ref} can be found in Table 3.3. The table shows three different wind turbine classes, where each class represents a different levels of turbulence intensity, where class A is high turbulence, class B is medium turbulence and class C is low turbulence. Turbulence intensity depends on the local terrain and surface roughness. Locations further inland usually have higher turbulence intensity due to trees, buildings and uneven terrain creating a rough surface, while locations offshore have a smoother ocean surface.

For example, F.C. Mehlan and A.R. Nejad [6] have investigated the effects of rotor imbalances on a floating offshore WT, therefore they used I_{ref} value for a class C WT. In general, simulating a WT in an offshore environment, let alone a floating one, is more complex, time consuming and computationally intensive, since the wave profile and wave interactions with the floater would have to be accounted for in the model. Therefore, for simplicity reasons and time constraints of this thesis, it was decided to model an onshore turbine, thus, I_{ref} value for class A turbines was used. However, a beneficial outcome of conducting the simulations at higher turbulence intensity, is that it can put a higher emphasis on the effect turbulence has when comparing results from steady and turbulent wind conditions.

Table 3.3: Basic Parameters for Wind Turbine Classes [57].

Wind turbine class		I	II	III
V_{ref}	(m/s)	50	42,5	37,5
A	I_{ref} (-)	0,16		
B	I_{ref} (-)	0,14		
C	I_{ref} (-)	0,12		

Turbulent wind files were generated by using a software called 'TurbSim'. TurbSim is a stochastic, full-field, turbulence simulator. It uses statistical models, rather than physical ones, to simulate time varied wind vector field in three dimensions [58]. Table 3.4 shows the I_{ref} values calculated using Equation 3.1 and the corresponding wind speed values used to generate the turbulent wind files. For each wind speed case, six different turbulent seeds were generated to have a larger sample size and therefore precision. For instance, if a certain dynamic response is observed in all six seeds, then the result will have a higher statistical significance than if a certain response is observed in only one of the seed. Therefore, the data obtained from six turbulent seeds is averaged to account for randomness.

Wind Speeds

To simulate a wide range of aerodynamic loads, six wind speeds were considered, three of which are below rated wind speed, 4, 7 and 10 m/s, denoted by U_1-U_3, respectively. While the rest are above rated wind speed, 12, 14 and 20 m/s, denoted by U_4-U_6, respectively. The same wind speed values are used for both steady and turbulent wind conditions. The above mentioned values were taken from the paper by F.C. Mehlan and A.R. Nejad [6].

Simulating wind speeds below and above rated is important because the pitch controller begins to pitch the blades to stall at above rated speeds, changing aerodynamic behaviour of the rotor. Additionally, the wind speeds are intentionally spread out to cover speeds close to cut-in, below and above rated threshold and cut-off threshold to see how the turbine behaves in scenarios close to change of state of operation. This is especially important for turbulent wind conditions, since wind speeds close to those thresholds could cross them due to speed fluctuations.

Table 3.4: Environmental Parameter Settings

Wind Condition	Environmental Parameter	Case					
		U_1	U_2	U_3	U_4	U_5	U_6
Steady Wind	Wind speed, U [m/s]	4.0	7.0	10.0	12.0	14.0	20.0
Turbulent Wind	Wind speed, U [m/s]	4.0	7.0	10.0	12.0	14.0	20.0
	Turbulence intensity, I [-]	0.34	0.25	0.21	0.19	0.18	0.16
	Number of seeds	6	6	6	6	6	6

Signals of Interest

The effects of the aforementioned fault cases and environmental conditions is assessed by measuring moment and force in the LSS, from OpenFAST simulation output. In total, six signals are measured: moment in x, y and z direction, and force in x, y and z direction - in the shaft's non-rotating frame of reference, as previously depicted in Figure 2.10. Moreover, each signal is outputted in the time domain. This is done for each fault case - environmental condition combination. The list of signals, as they are named in OpenFAST, can be found in Table 3.5.

Table 3.5: List of Output Parameters

Output Parameter	Description	Axis
LSShftFxa	Low-speed shaft thrust force [kN] (constant along the shaft)	x-axis
LSShftFys	Low-speed shaft shear force [kN] (constant along the shaft)	y-axis
LSShftFzs	Low-speed shaft shear force [kN] (constant along the shaft)	z-axis
LSShftMxs	Low-speed shaft torque [kNm] (constant along the shaft)	x-axis
LSSTipMys	Low-speed shaft bending moment at the shaft tip [kNm]	y-axis
LSSTipMzs	Low-speed shaft bending moment at the shaft tip [kNm]	z-axis

Periodic Frequencies

Since the WT is simulated at different wind speeds, it means that the rotor revolves at different RPMs, at below rated wind speeds $U_1 - U_3$. Whereas above rated wind speeds, $U_4 - U_6$, the rotation speed of the rotor is constant. Subsequently, the periodic frequencies also change with wind speed. Table 3.6 shows a list of periodic frequency values at different wind speeds.

Table 3.6: Periodic Frequency Values at Each Wind Speed

	Wind Speed			
Periodic Frequency [Hz]	U_1	U_2	U_3	U_4 - U_6
1P	0.1164	0.1165	0.1338	0.1600
2P	0.2328	0.2330	0.2676	0.3200
3P	0.3492	0.3495	0.4014	0.4800

3.1.4. OpenFAST Initialisation

With all the fault cases and environmental settings determined, it is now possible to run simulations. The final initialisation step is specifying simulation duration and time-step. The duration needs to be long enough to ensure two things. Firstly, the simulation has transient start-up time, which needs some time to settle [6]. Secondly, is to have a rich source of data for analysis, since analysing large data sets is more statistically significant, and makes the results more accurate. Moreover, this is especially true for cases running in turbulent wind conditions, since the random variability of wind speed and direction would average out over long periods of time.

The time-step determines how often each simulation parameters are updated, similar to sampling frequency. For example, for a time-step of 0.5 seconds, the simulation parameters are updated two times per second, while for a time-step of 0.25 they are updated four times per second. Lower time-step means the output data is calculated to a higher degree of accuracy, but require more computational power. NREL recommend the time-step to be around ten times of the highest frequency modelled, based on Equation 3.2 [51]. In this experiment, the highest frequency of interest is 3P rotor harmonic. Above rated speed, the rotor speed reaches 9.6 RPM, or 0.16 Hz, meaning 3P frequency would equal to 0.48 Hz. This results in a time-step of 0.208 seconds or lower.

$$DT = \frac{1}{10 f_{max}} \tag{3.2}$$

Therefore, it was decided to follow F.C. Mehlan and A.R. Nejad's [6] methodology and use a simulation duration of 4000 seconds with a time-step of 0.025 seconds. Having a lower than recommended time step will ensure a rich and high resolution data set for a more accurate analysis. The first 400 seconds are discarded to let the transient time of the simulation to settle, resulting in 3600 seconds or 1 hour of real time simulated.

3.2. Data Processing

After setting up and running the simulations, OpenFAST outputs a large file, containing a large matrix of data, for each output parameter specified in the settings. As mentioned previously, it was decided to simulate 4000 seconds of real time at a sampling frequency of 40Hz, resulting in a total of 160 000 data points per output parameter. Working with large data sets like this can be quite challenging; therefore, appropriate data processing techniques need to be utilised in order to analyse the signals properly.

3.2.1. Processing Strategy

In this study, it was decided to use MATLAB to process the output data. The data processing strategy, summarised in Figure 3.1, has the following format. First, the data output from OpenFAST simulations needs to imported into MATLAB, and formatted into the correct '.mat' format, which will allow for data manipulation.

Second, the data need to be processed using MATLAB code. As mentioned in section 2.2 and section 2.3, output data is in the time domain. However, in order to analyse the periodic harmonics produced by the rotor, the data needs to be transformed into the frequency domain. This is done using a Fast Fourier Transformation (FFT) [59]. FFT is a signal processing algorithm used across various industries to discompose complex output signals into multiple simpler signals in the frequency domain.

Third, the code needs to be automated. The total number of cases simulated is 420, of which 60 of the cases are from steady wind simulations and 360 of which are from turbulent wind simulations. Processing such a large number of output files one by one would be unreasonably time-consuming, therefore a processing algorithm needed to be created, with the ability to handle multiple cases at the same time. Additionally, the algorithm needs to be able to output the data in a user-friendly format without irrelevant signals, to allow faster extraction of peaks for data analysis. A more detailed overview of this algorithm can be found in subsection 3.2.2

Lastly, the processed data need to be analysed. The data is plotted on a bar plot with respect to periodic rotor frequency, environmental conditions, fault type, and fault level. Finally, the plots are analysed using the methods discussed later in subsection 3.2.3, and a decision tree is proposed.

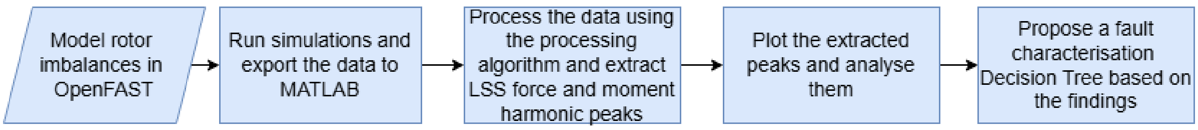

Figure 3.1: Data Processing Strategy

3.2.2. Processing Algorithm

The data processing algorithm was devised based on the signal processing methodology found in literature [6]. The strategy is as follows: extract the output signals listed in Table 3.5, disregard the first 400 seconds, divide it into 60 one-minute intervals, calculate the FFT of each window and calculate the mean of all the FFTs. The purpose of the algorithm is to execute this strategy for multiple cases at once. In addition, the output must be formatted in a way that is easy to extract for plotting and analysis. The full version of the MATLAB code can be found in Appendix A.

Segmenting

After removing the first 400 seconds of the signals listed in Table 3.5, the algorithm segments the data into 60 one-minute time windows, or 2400 data points per window. The algorithm then analyses the segments one-by-one, repeating itself for the next 2400 data points 60 times, using a for loop. Each loop iteration is stored and averaged after the final iteration.

Frequency Peak Calculation

Each segment undergoes an FFT, with 0.0167Hz frequency resolution. The FFT converts the time-domain data into frequency domain. Now that the data is in the frequency domain, the peak frequencies can be extracted. This is done using Matlab commands below. The commands essentially normalize the signal by dividing the FFT by its length, L. The FFT output has an imaginary component in it, therefore the absolute value is taken to obtain the magnitude spectrum. Moreover, the spectrum is two-sided, meaning the spectrum contains frequencies that are positive and negative, where positive frequencies are a complex conjugate of the negative. This results in peak magnitudes in the frequency domain to be equal to half of peak magnitudes in the time domain. The first and last values are the 0 and Nyquist frequencies, respectively, which do not have a complex conjugate and therefore do not need to be multiplied by 2.

```
Y = fft(x);     %where x is the 1-minute data segment
L = 2400;       %Length of the signal
P2 = abs(Y/L); %Normalized magnitude spectrum, where L is signal length
P1 = P2(1:L/2+1); %Two-sided spectrum
P1(2:end-1) = 2*P1(2:end-1); % single-sided spectrum
```

Filtering and Sorting

The next step is to filter the single-sided spectrum. The spectrum contains noise in the form of small amplitudes at different frequencies. This causes an issue when storing the data, resulting in large data sets of unwanted data. The filter ensures values smaller than 10% of maximum peak magnitude are stored and the rest are equated to 0.

By default, the data are stored in a two-column matrix, where column 1 is dedicated to the peak magnitude and column 2 for that peak's frequency. This is problematic, since the algorithm needs to be able to analyse multiple output parameters at once to speed up data processing. Therefore, peak-frequency pairs are allocated into seperate column pairs, one for each output parameter. For example, Figure 3.2 shows how the LSShftFzs pair is sorted into a separate column pair from LSShftFys.

LSShftFys	8.38	1P
	24.54	2P
LSShftFzs	24.19	1P
	55.33	2P

LSShftFys		LSShftFzs	
8.38	1P	24.19	1P
24.54	2P	55.33	2P

Figure 3.2: Sorting peak-frequency pairs into separate columns

Summation and Averaging

Finally, the 60 stored and sorted matrices are added together and averaged. Each matrix has the same number of columns, equal to double the number of output paramers. However, a problem arises if matrix M+1 has more rows of peak-frequency pairs than matrix M, because Matlab will not be able to perform matrix addition, resulting in an error. This issue is resolved by first finding the matrix with the largest number of rows and placing that matrix first on the list. Next, the algorithm calculates the number of rows in other 59 matrices. If the number of rows in a matrix does not equal to the number of rows of the largest matrix, then the algorithm adds a row of zeros to it at the bottom. The size is checked again in a loop, until the sizes match. This is repeated until all matrices are of the same size.

An important step when adding the matrices together is ensuring that the correct peaks are added together. For example, 1P peak needs to be added to the 1P peak. However, in many cases, 1P magnitude can be added with a 2P or a 3P magnitude, which is incorrect. Therefore, after making the matrices the same size, the summation loop can take place. The algorithm compares the frequency value of the first row column pair with the first row column pair of a subsequent matrix. If the frequencies match, the magnitude and frequency in that position are added together. If they are not equal, the algorithm checks the peak-frequency pair in the next row, until a match is found. If no match is found, zeroes are added, and the next row column pair of the first matrix is checked. This process is repeated until all matrices have been added, resulting in one matrix with summed up values.

After each successful addition, the addition count is stored. If no addition took place, for example, in the case where zeroes are added, the addition count does not change. The final summed up matrix is then divided by the addition count, resulting in a sorted and averaged matrix, which is later used for data analysis. This algorithm works for both steady-state and turbulence environmental conditions. However, the algorithm has an additional step of averaging the six turbulent seeds for turbulent data sets. This algorithm is repeated for every environmental condition and fault case combination.

3.2.3. Data Analysis and Presentation

After force and moment FFTs have been extracted and averaged, they can be analysed. The data contains three fault cases at three different fault levels for each case, each of which refers to six different wind speeds in steady and turbulent conditions. For each case and environmental condition combination, three force and three moment signals are analysed, which are listed in Table 3.5. In total, this results in 720 signals to be analysed.

Bar Plots

Bar plots are formatted in the following way. The vertical axis shows the absolute difference between the faulty peak magnitude and the healthy peak magnitude at a particular periodic frequency, while the horizontal axis shows the fault level F_1-F_3. Each plot contains the peak magnitudes for all fault cases at one wind speed and one periodic frequency. The force and moment signals are plotted separately. Figure 3.3 shows an example of a bar plot, which looks at absolute difference between faulty and healthy 1P LSS moment peaks about the x, y and z axis, for each fault case and three fault levels. Fault levels 1-3 are denoted by F_1-F_3, respectively. Each fault case PM$_{x/y/z}$, MI$_{x/y/z}$ and YM$_{x/y/z}$ denotes the moment difference about x, y and z axis. The same principles apply for force bar plots.

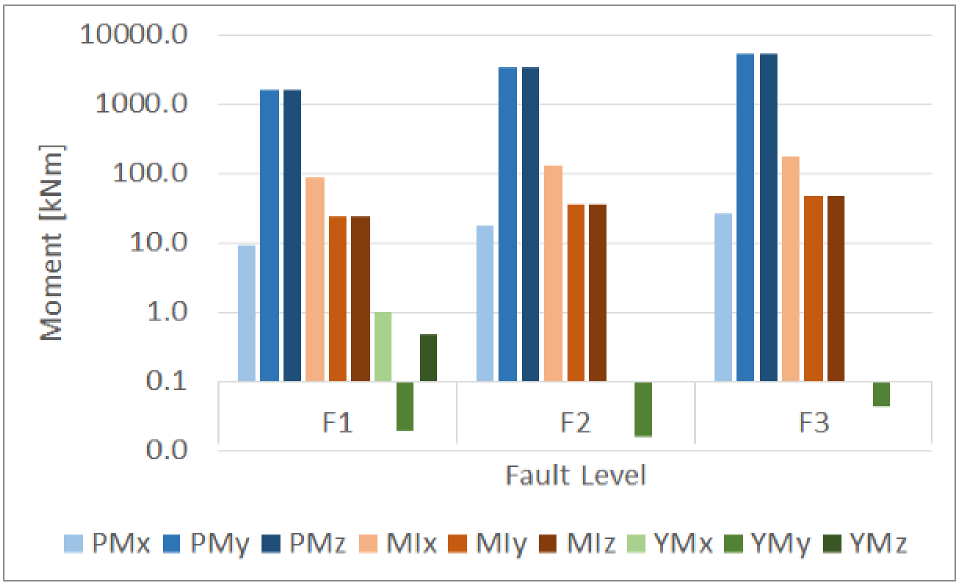

Figure 3.3: Example bar plot: Absolute Change in LSS Moment at U_1 and 1P

The purpose of plotting data signals this way is to show the relationship between fault cases and fault levels in the same environmental conditions, as well as measure the numerical difference in magnitude between a healthy and an imbalanced rotor. The absolute change is measured for the ability to plot the data on a logarithmic scale, in order to level the size of bars due to large differences in peak magnitudes in many cases, making the bar plots more readable. Some information regarding the dynamic response is lost when the absolute value is taken, since some faulty signals have a decreased magnitude in comparison to the healthy signals. That being said, the majority of cases have a positive increase in magnitude, so that is only an issue for some of the cases.

Summary Tables

While the bar plots show a good amount of numerical detail about trends between fault cases and fault levels at a particular wind speed and periodic frequency, the total number of bar plots is too high to analyse the trends between wind speeds and periodic frequencies. For this reasons, the data is also presented in the form of summary tables.

The difference between healthy and faulty peaks is summarised by first dividing the data into below (U_1, U_2 and U_3) and above rated (U_4, U_5 and U_6) wind speeds. Next, the data is further divided by fault case and frequency. Finally, the categorised peaks are added together and averaged. For example, for the below rated case of PM$_x$ at 1P frequency, the peak differences in moment at U_1-U_3 for fault levels F_1-F_3 are added together and the mean value is calculated. This process is repeated for each fault case and frequency below and above rated wind speeds. This is expressed mathematically in Equation 3.3 and Equation 3.4, used for below rated and above rated wind speeds, respectively. There, $\Delta\bar{P}_{BR}$ and $\Delta\bar{P}_{AR}$ are the average differences in peak magnitude, below and above rated, respectively. C is the specific fault case force or moment magnitude, i represents the fault level subscript as in F_i, and j represents the wind speed subscript as in U_j.

$$\Delta\bar{P}_{BR} = \frac{1}{9}\sum_{i=1}^{3}\sum_{j=1}^{3} C_{ij} \quad | \quad \text{for} \quad i = \{1,2,3\} \quad j = \{1,2,3\} \tag{3.3}$$

$$\Delta\bar{P}_{AR} = \frac{1}{9}\sum_{i=1}^{3}\sum_{j=3}^{3} C_{ij} \quad | \quad \text{for} \quad i = \{1,2,3\} \quad j = \{4,5,6\} \tag{3.4}$$

The tables are also colour-coded based on how large the change is from healthy to faulty, with a different scale for force and moment signals. To determine the scale for the moment, the difference in the moment peaks for each case, wind speed and frequency is distributed into five equally sized bins. This is shown in Figure 3.4–3.5, for steady and turbulent windm respectively. In this figure, each bin represents a level of how sensitive the signal is to a fault in the rotor. Figure 3.4a shows the five bins obtained from distributing all absolute moment peak differences above 0, M1-M5, each with its own colour. Bins M1-M4 each have ranges of 50 kNm, while the M5 includes all peaks above 200 kNm. The same approach was taken for the force peak difference. Figure 3.4b shows the five bins obtained from distributing all force peak differences above 0, F1-F5, with the same colour coding as M1-M5 bins. Bins F1-F4 each have ranges of 6 kN, while the F5 bin includes all the peaks above 24 kN.

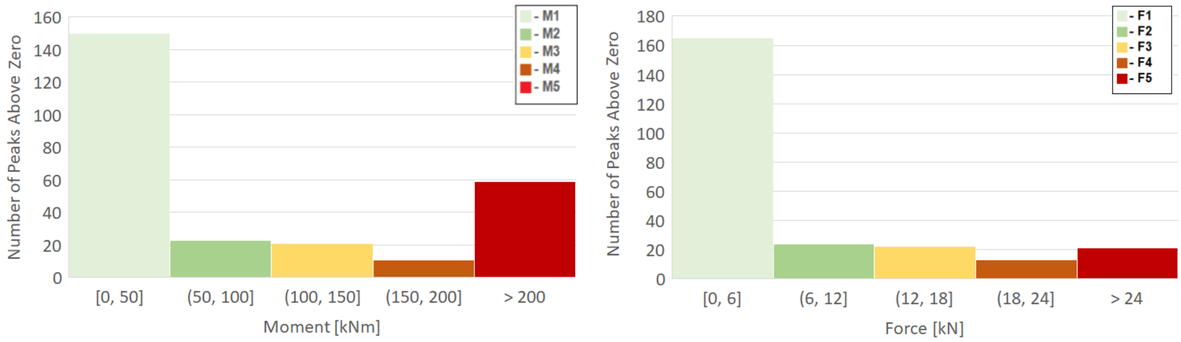

(a) Difference in Moment **(b)** Difference in Force

Figure 3.4: Difference in Moment and Force Peaks in LSS Between Healthy and Faulty Conditions, Steady Wind

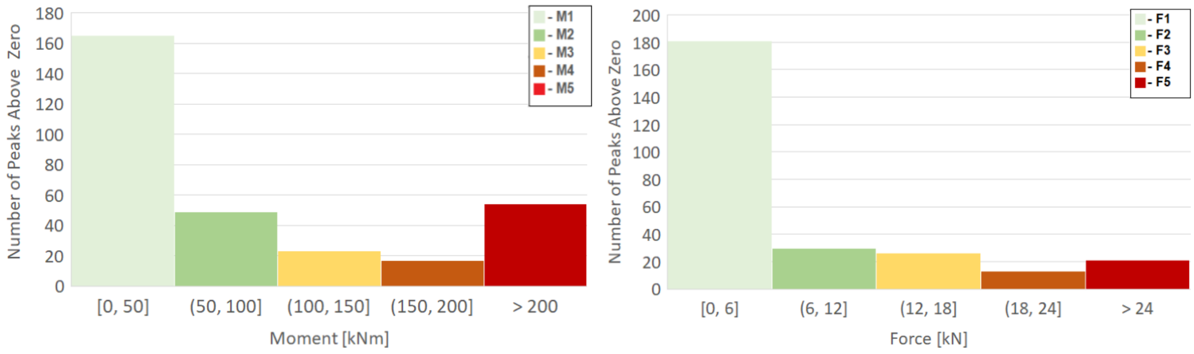

(a) Difference in Moment

(b) Difference in Force

Figure 3.5: Difference in Moment and Force Peaks between Healthy and Faulty Conditions, Turbulent Wind

Using bar plots and summary tables described in this section, the most sensitive signals for each fault case are determined. Signal sensitivity is determined based on three factors.

- The difference in magnitude between healthy and faulty signals, where the larger the magnitude change, the more sensitive the system is to fault being present
- The magnitude difference increase with fault level. That is, if magnitude difference in a fault case increases from fault levels F_1 to F_2, and from F_2 to F_3, then it is more likely that similar behaviour will be seen in a different simulation setup with the same fault case present. The increasing trend with fault level is represented by underlining M1-M5 or F1-F5 in the summary tables
- The magnitude difference increase with wind speed. That is, if magnitude increases from U_1 to U_2 and from U_2 to U_3, the a "+" is added next to the bin value for below rated wind speed range in the summary table. The same is done for above rated wind speeds.

Table 3.7: Summary tables legend for moment and force

Moment	Range [kNm]
M1	0 < M ≤ 50
M2	50 < M ≤ 100
M3	100 < M ≤ 150
M4	150 < M ≤ 200
M5	200 < M
N/A	unclear/zero
Underlined	Increases with fault
+	Increases with wind speed
c	Constant with wind speed

Force	Range [kN]
F1	0 < F ≤ 6
F2	6 < F ≤ 12
F3	12 < F ≤ 18
F4	18 < F ≤ 24
F5	24 < F
N/A	unclear/zero
Underlined	Increases with fault
+	Increases with wind speed
c	Constant with wind speed

3.2.4. Rotor Imbalance Characterisation

Based on the analysed data, rotor imbalances are characterised. The most sensitive signal based on magnitude, speed, and fault trends is chosen to represent the type of rotor imbalance present in the rotor. In the case where the same signal could represent two different rotor fault types, a less sensitive signal, that is not present in another rotor fault case, is chosen. The representative signals are then used to form a decision tree flowchart, to simulate how a fault detection and characterisation algorithm would identify rotor imbalance type based on sensor data, assuming a scenario where the data is obtained from a real WT.

It was previously mentioned in section 3.1 that this simulation is designed based on methodology proposed by [6]. Therefore, the findings of this work are compared to theirs, in order to assess validity of the data obtained from simulations. That being said, [6] have only looked at 1P rotor harmonic in turbulent wind conditions, thus only 1P turbulent results can be compared.

4

Results and Discussion

4.1. Steady Wind Simulation Results

As mentioned previously in Chapter 3, three different fault conditions were modelled in steady and turbulent wind conditions, at six different wind speeds and three levels of fault severity. The LSS moments and forces were analysed in the harmonic domain and the peaks were extracted. The data were sorted and averaged using the data processing algorithm, described in subsection 3.2.2. In this section, steady-state simulation results are presented in the form of bar plots and summary tables, as explained in subsection 3.2.3. In this chapter, only a subset of results is presented for clarity and brevity. Specifically, two representative cases: one below and one above rated wind speed. The full set of results can be found in the Appendix B.1.

4.1.1. Low Speed Shaft Moment

1P Harmonic

In this section, the absolute change in the 1P peaks in the LSS moment is discussed at two different wind speeds: at below rated U_3 and at above rated U_6. Figure 4.1 shows the change at 1P harmonic, while Figure B.1 shows the results for all wind speeds tested. Overall, it can be seen that PM and MI fault cases show significant change in 1P peak magnitude in all three directions, with PMy and PMz having the largest magnitude difference. On the other hand, YM fault case shows little to no change from healthy conditions at the 1P harmonic, therefore it was omitted from Figure 4.1 to enhance clarity.

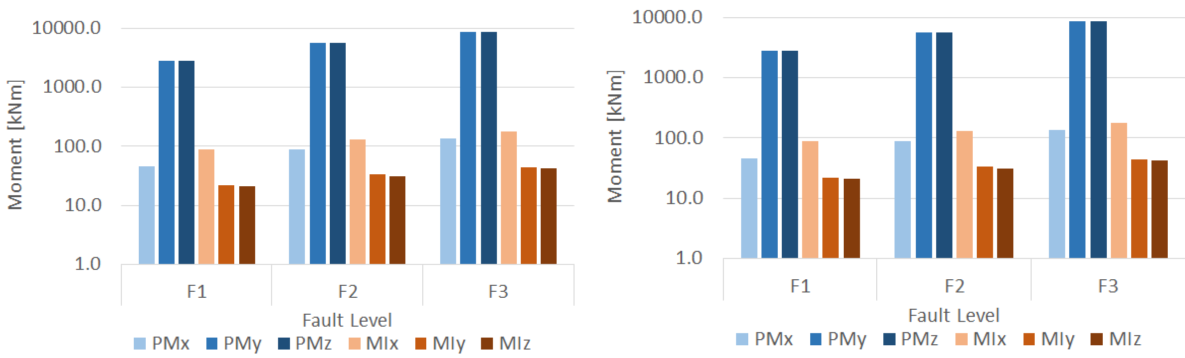

(a) 1P LSS Moment Below Rated U_3 = 10m/s

(b) 1P LSS Moment Above Rated U_6 = 20m/s

Figure 4.1: Absolute Change in LSS Moment Below and Above Rated Wind Speeds at 1P Harmonic in Steady Wind Conditions

For PM, such a large difference in magnitude could be caused by the large blade length, making the system sensitive to small changes in pitch angle. Additionally, an increasing trend with both wind speed and fault level is observed for all PM cases, both below and above rated speeds. This was an expected outcome following the explanation on the origin of 1P rotor harmonics in subsection 2.2.1. For the case of MI, the results show an increasing trend with fault level. However, the system appears to be less seinsitive to MI than it is to PM in terms of magnitude difference

When comparing the results between U_3 and U_6, the magnitude decreases for PMx, MIx, MIy and MIz, while it increases for PMy and PMz. The decrease in PMx and MIx can be explained by the pitch controller pitching the blades to stall above rated wind speed, aerodynamically limiting toque generation [6, 11]. Looking at results for all wind speeds in AppendixB.1, PMx torque progressively increases between $U_1 - U_2 - U_3$, then significantly drops from U_3 to U_4 and starts progressively increasing again between $U_4 - U_6$, at all fault levels.

The same decrease from U_3 to U_4 can be seen for MIx, but unlike the PMx case, no progressive increase can be seen between wind speeds below or above rated. A possible explanation for this could be the fact that 1P torque harmonic in the MI case is caused by gravitational forces and shifted centre of gravity, which in theory should be independent of wind speed [11]. Whereas in the case of PM, the 1P torque harmonic is aerodynamic in nature, which in theory should be affected by a change in wind speed.

In the case of PMy and PMz, the magnitude difference progressively increases between all wind speeds $U_1 - U_6$. This complies with the theory, since PM is aerodynamic in nature , therefore it is natural for it to increase at higher wind speeds. MIy and MIz show a decreasing trend with wind speed between $U_1 - U_3$, but the trends for these two signals differ above rated. For MIy, the magnitude drops significantly from U_3 to U_4 and starts progressively increasing from $U_4 - U_6$. Whereas for MIz, the trend is reversed: magnitude increases from U_3 to U_4, but starts decreasing between $U_4 - U_6$. These trends were not expected, since in theory the bending moments should be caused by centrifugal force and gravity from the mass imbalanced blade, as was explained back in section 2.4. Therefore, the bending moments should follow the same trends as the shear force shown in Figure B.4, which it does not.

For the case of YM, no response at the 1P moment harmonic was an expected outcome. This is because all three blades are affected equally at once by the change in yaw angle. Therefore, unlike PM and MI cases which affect only one blade, insignificant 1P harmonic response can be seen for YM.

2P Harmonic

Similarly, Figure 4.2 and Figure B.2 show the absolute change at 2P harmonic. Overall, it can be seen that the system is sensitive to the cases of PM and MI, with PMy and PMz signals showing a larger change than the other fault cases. The peaks increase with fault level both below and above rated wind speeds, while also progressively increasing with wind speed from $U_1 - U_6$. Similartly to the 1P moment results, YM case has been omitted from Figure 4.2 to enhance clarity.

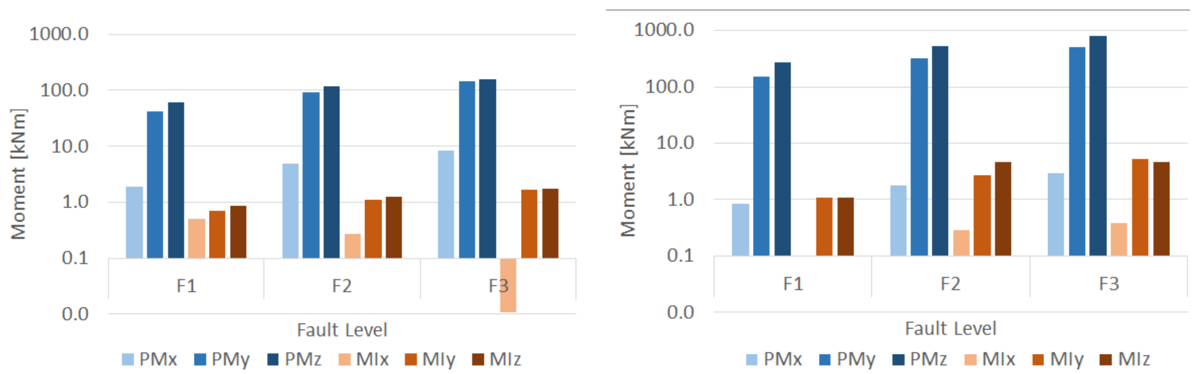

(a) 2P LSS Moment Below Rated U_3 = 10m/s

(b) 2P LSS Moment Above Rated U_6 = 20m/s

Figure 4.2: Absolute Change in LSS Moment Below and Above Rated Wind Speeds at 2P Harmonic in Steady Wind Conditions

PMx also shows an increasing trend with fault level for all wind speed cases. Below rated, the magnitude drops from U_1 to U_2, but increases at U_3, to values higher than both U_1 and U_2. During the transition to above rated wind speed, the magnitude drops from U_3 to U_4, which is probably caused by the blades pitching. However, it begins to progressively increase between $U_4 - U_6$. Although the data show that the magnitude trends with both fault level and wind speed for the PMx signal, the magnitude itself is relatively small, especially when comparing to PMy and PMz signals.

Similarly, MIy and MIz also show an increasing trend with fault level below and above rated, with a slightly larger magnitude above rated. On the contrary, the difference in peak magnitude one to two orders of magnitude smaller than PMy and PMz signals, showing a much less sensitive system response at this harmonic. The remaining YM and MIx signals show small peaks without a consistent trend with fault level or wind speed.

3P Harmonic

Figure 4.3 and Figure B.3 show the moment peaks at 3P harmonic. Unlike at 1P and 2P harmonics, the 3P harmonic is also present in a healthy rotor. PMy and PMz peaks can also be seen below and above rated, having a significantly larger magnitude above rated. Below rated, no trend with wind speed or fault level can be seen. However, above rated, the magnitude difference tends to increase with both fault level and wind speed consistently. This result was not expected, since 3P harmonics are rarely mentioned in the context of PM in literature.

YMy and YMz peaks show an increasing trend with fault level and wind speed below and above rated. Additionally, the magnitude drops slightly from U_3 to U_4, due to pitch control activation. This result complies with theory discussed in subsection 2.2.1, since all blades are affected equally by the change in yaw angle, thus the moment fluctuation is detected three times per rotation. Other signals show no significant response at this harmonic, as the magnitude change is small and no wind speed or fault trends are present.

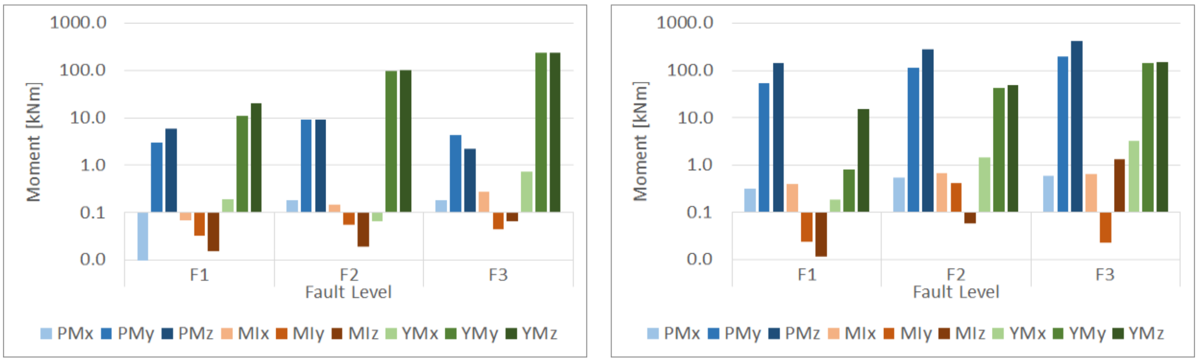

(a) 3P LSS Moment Below Rated U_3 = 10m/s

(b) 3P LSS Moment Above Rated U_6 = 20m/s

Figure 4.3: Absolute Change in LSS Moment Below and Above Rated Wind Speeds at 2P Harmonic in Steady Wind Conditions

4.1.2. Low Speed Shaft Force

1P Harmonic

In this section, the absolute change in force peaks in the LSS is shown at two different wind speeds: at below rated U_3 and above rated U_6, shown in Figure 4.4. The full set of results can be found in Figure B.4. Overall, it can be seen that PM in all three directions shows in a increasing magnitude trend with both wind speed and fault level, below and above rated wind speed, while also having a significant increase in magnitude above rated wind speed. Additionally, force response is similar to the moment response discussed previously, and follows the theory from section 2.1.

All three MI force signals show an increasing trend with wind speed and fault level at below rated conditions. However, above rated these trends change. MIx keeps the tendency to increase with fault level for all wind speeds, but begins to progressively decrease from $U_4 - U_6$. MIy and MIz also keep their increasing trend with fault level, however, show very little change in magnitude between $U_4 - U_6$, with changes being in the 10^{-1} magnitude range. This result was expected following the explanation on centrifugal force from section 2.4. Similar to the moment response, YM show little to no response at the 1P harmonic.

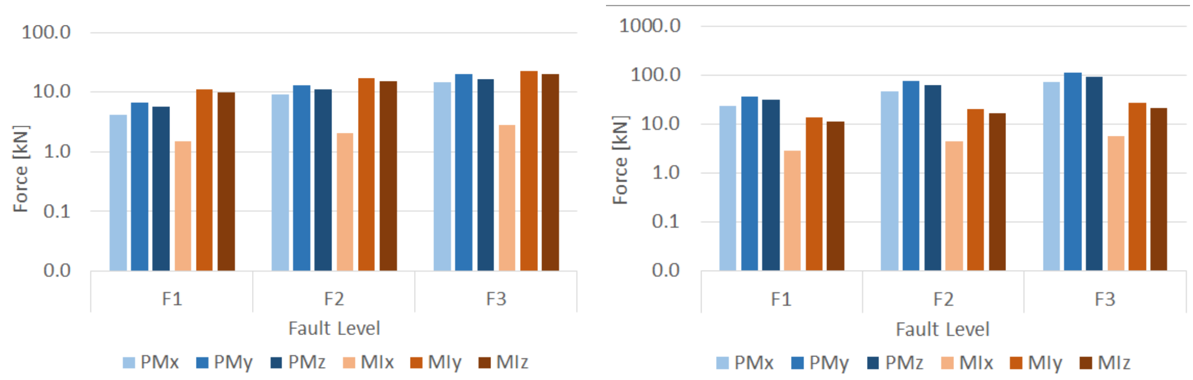

(a) 1P LSS Force Below Rated U_3 = 10m/s **(b)** 1P LSS Force Above Rated U_6 = 20m/s

Figure 4.4: Absolute Change in LSS Force Below and Above Rated Wind Speeds at 1P Harmonic in Steady Wind Conditions

2P Harmonic

Figure 4.5 and Figure B.5 show the force peak differences at the 2P harmonic. In general, all cases show a relatively small difference in magnitude at this harmonic, ranging from $10^{-2} - 10^{0}$ kN. All three PM cases show an increasing trend with fault level at all wind speeds, below and above rated wind speed. However, only PMx below and above rated, and PMz above rated show a consistent increasing trend with wind speed. The trends in force at this harmonic are very similar to the trends in the moment shown earlier, in terms of the increase with fault level and wind speed. That being said, the difference in force magnitude is much less significant than what is observed for the difference in moment magnitude.

Although some of the MI and YM cases showed fault level trends at the 2P moment harmonic, these trends are not seen for the change in the 2P force harmonic. All three cases show no significant changes in magnitude, or have any consistent trends with either fault level or wind speed. The loss of trends present in the 2P moment harmonic was not expected, since a change in shear force should result in a proportional change in bending moment.

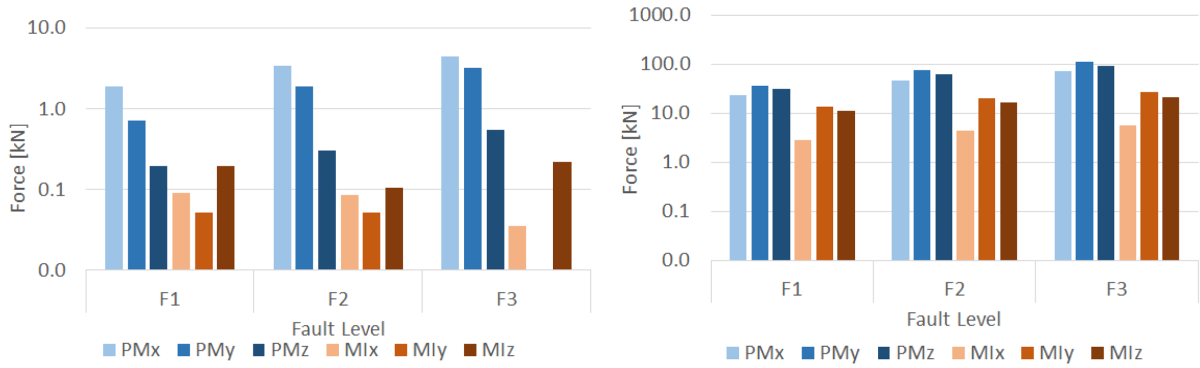

(a) 2P LSS Force Below Rated U_3 = 10m/s **(b)** 2P LSS Force Above Rated U_6 = 20m/s

Figure 4.5: Absolute Change in LSS Force Below and Above Rated Wind Speeds at 2P Harmonic in Steady Wind Conditions

3P Harmonic

Figure 4.6 and Figure B.6 show the force peak differences at the 3P harmonic. Overall, it can be seen that the magnitude change at this harmonic is rather small for the majority of signals. The majority of cases do not show a consistent trend of a magnitude increase with the level of the fault or wind speed, whereas the magnitudes remain small at all speeds and fault levels. All three PM cases show an increasing trend with wind speed above rated speeds. Other than that, only YMx shows an increasing trend with wind speed at below and above rated speeds.

Similarly to the 2P force harmonic, some of the signals that previously had trends at the 3P moment harmonic have lost them at the 3P force harmonic. Namely, PMz has lost their increasing trend with fault level at above rated speeds, while YMy and YMz have lost their trends with fault level and wind speed at below and above rated speeds. After double checking the data, both with and without averaging it, the possibility of trends being lost due to averaging can be ruled out, since steady wind conditions produce a rather uniform signal which does not vary between time windows.

Another potential reason for this outcome could be the peak extraction algorithm was picking up noise. To test this, the FFTs of the moment and force signals were plotted to see whether noise was being extracted, shown in Appendix C.1. These figures show FFTs at two wind speeds, U_2 and U_5, and two fault levels, PM1 and PM3, of the PM case in the y-direction. It can be seen that distinct peaks appear at U_2 for all moment and force cases. However, this changes for U_5. For the moment, the 3P peak flattens, meaning the peak being picked up by the algorithm was indeed noise. For the force, both 2P and 3P peaks flatten, meaning it was noise for these cases, too. A similar situation is observed for PMz, YMy and YMz.

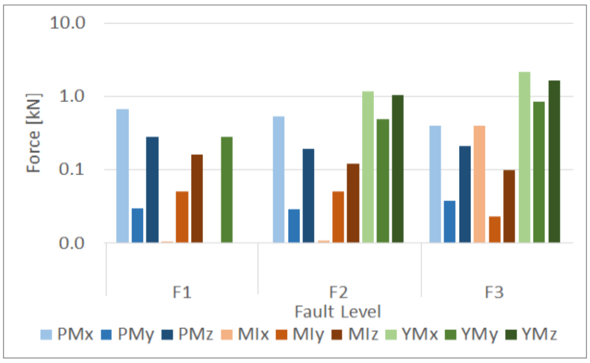

(a) 3P LSS Force Below Rated U_3 = 10m/s

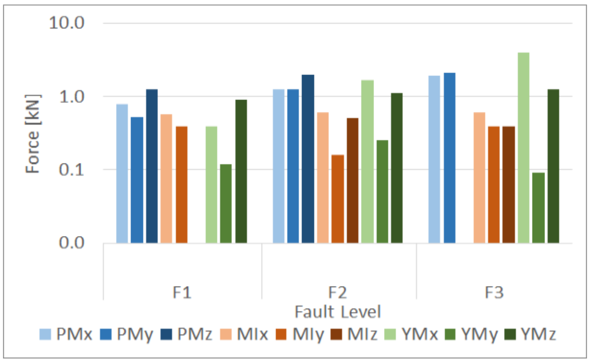

(b) 3P LSS Force Above Rated U_6 = 20m/s

Figure 4.6: Absolute Change in LSS Force Below and Above Rated Wind Speeds at 3P Harmonic in Steady Wind Conditions

4.1.3. Discussion

To help analyse the results and trends present within, the data needs to be further processed and analysed from a different perspective. This chapter contains the results from the steady wind simulations that have been summarised with an intent to highlight the trends and system responses to the three fault cases.

Pitch Misalignment

Table 4.1 shows the averaged results below and above rated wind speeds for the case of PM, the colour code for which can be found in Table 3.7. The moment in x-direction (the torque) shows to be more sensitive to PM at 1P harmonic, with an average magnitude change of 50.2 kNm. However, at above rated, the peak difference in PMx becomes much smaller at 10.3 kNm. At 2P and 3P harmonic, the difference in torque peaks decreases further, both below and above rated. The force in x-direction (thrust), on the other hand, shows a large increase from below to above rated speeds at 1P harmonic. Whereas, at 2P and 3P the change becomes less significant.

The moment and force in the y and z directions show similar trends to each other in terms of average peak difference, with both moments and forces in the z-direction showing slightly larger magnitude changes for all harmonics than in the y directions, with an exception of below rated moment in y-direction. Moment changes at 1P harmonic are very large compared to other signals below rated, increasing even further above rated. Moments at 2P harmonic appear to be less sensitive to PM below rated, displaying values between M2-M3 levels (in reference to the scale provided in Table 3.7), while above rated, the sensitivity increases drastically to M5 level in both directions. Forces, on the other hand, show a different response to PM. 1P force changes show lower sensitivity below rated speeds, being at level F2 on average. However, the changes become much larger above rated, going above the F5 level threshold. As for 2P and 3P harmonics, both directions are shown to be much less sensitive to PM, resulting in F1 level peaks below and above rated.

In terms of magnitude change, 1P harmonic has shown to be the most sensitive to PM in all three directions, both for moment and force signals. Additionally, the 2P harmonic has consistently appeared in the moment FFTs for all directions below and above rated wind speeds, while only appearing below rated for all force cases, as is shown in Figure C.1 – C.6. The 3P harmonic, on the other hand, lacked the same consistency demonstrated by the 1P and 2P harmonics, having small peaks in comparison to the noise.

From this, it can be concluded that the 1P moment and force harmonics can be considered as PM identification factors with a high degree of confidence, due to their consistently high peak compared to the surrounding noise, both below and above rated wind speeds, as well as trends present. Moreover, the below and above rated 2P moment harmonics can also be considered as potential PM identification factors, despite being less sensitive than the 1P harmonic. The 3P harmonics, however, should not be considered as potential identification factors for this type of imbalance, due to the relatively small peaks compared to the noise, despite having a relatively large magnitude difference. That being said, it is still not fully clear as to why exactly the 2P and 3P moment harmonics are far more sensitive than the force harmonics.

Table 4.1: Average Moment and Force Peak Difference in LSS Between a Healthy Rotor and a Rotor with PM, Steady Wind

		PM Moment in LSS [kNm]		PM Force in LSS [kN]	
Frequency	Axis	Below Rated	Above Rated	Below Rated	Above Rated
1P	x	50.2	10.3	5.8	37.7
	y	4490.0	8163.9	7.0	44.9
	z	4464.0	8333.3	6.2	36.9
2P	x	2.3	1.1	2.5	2.9
	y	92.3	306.1	1.4	0.7
	z	100.2	439.2	0.4	2.0
3P	x	0.0	0.3	0.2	1.0
	y	5.1	137.0	0.1	0.8
	z	4.4	235.1	0.5	0.8

Summary

Table 4.2 summarises the results for the steady case of PM. The table was constructed by utilizing the average peak differences in Table 4.1, while using the same colour scheme and sensitivity level derived in Figure 3.4. One key difference between Table 4.1 and Table 4.2 is that the latter also provides information on the trends related to wind speed and fault level. Table **??** and Table **??** provide the legend for the moment and force summary table, respectively. The legends contain the moment and force ranges for levels M_1-M_5 and F_1-F_5, respectively.

From Table 4.2 it can be seen that the most sensitive sets of resuls are 1P moment and force harmonics, due to the high magnitude difference, and wind speed and fault level trends present. The 2P moment harmonic shows and increased sensitivity at above rated speeds in y and z-directions, while the force harmonic shows to be much less sensitive. Similarly to the 2P moment harmonic, the 3P moment hamronic shows increased sensitivity above rated, while the 3P force harmonic appears to be less sensitive.

Table 4.2: Summary table for the case of PM at steady wind conditions

		PM Moment in LSS		PM Force in LSS	
Frequency	Axis	Below Rated	Above Rated	Below Rated	Above Rated
1P	x	M2+	M1+	F2+	F5+
	y	M5+	M5+	F2	F5+
	z	M5+	M5+	F2	F5+
2P	x	M1	M1	F1+	F1+
	y	M2	M5	F1	F1
	z	M3	M5+	F1	F1+
3P	x	M1	M1	N/A	F1+
	y	M1	M3	N/A	F1+
	z	M1	M5+	N/A	F1+

Mass Imbalance

Table 4.3 shows the averaged results below and above rated wind speeds for the case of MI. The 1P torque shows to be more sensitive to MI at below rated speeds, with an average magnitude change of 125.2 kNm, while it goes down significantly above rated to 6.2 kNm. The opposite is observed for the 1P thrust, with the magnitude increasing on average above rated speeds.

The 1P MIy and MIz moment harmonics show a substantial increase in magnitude both below and above rated wind speeds, with magnitudes being within the M1 region. In comparison, the 1P force harmonic demonstrates a higher degree of sensitivity to MI, with peaks ranging from F3 to F4 on the scale. Similarly, the 2P MIy and MIz moment harmonics show, on average, a peak magnitude difference of about 10^0 kNm, with peaks displaying a significantly large peaks compared to the noise. On the contrary, the 2P force signals could most likely be noise, in all directions.

Overall, the 1P harmonic seems to have the highest sensitivity to MI in all three directions, both for the force and the moment. All cases produce distinct 1P peaks, standing out from the surrounding noise, in addition to having consistent wind speed and fault level trends that could be used to characterise this fault case based on the signal data. The 1P MIy and MIz force signals have displayed the most consistent trends with theory [6][11] and can therefore be considered as primary signals for characterising the fault. On the other hand, 2P and 3P force and moment in all three directions show no significant change in magnitude or trends, with peaks extracted having a high noise ratio, shown in Figure C.7 – C.12. This therefore gives low confidence in using these signals as identification factors for the case of MI.

Table 4.3: Average Moment and Force Peak Difference in LSS Between a Healthy Rotor and a Rotor with MI, Steady Wind

		MI Moment in LSS [kNm]		MI Force in LSS [kN]	
Frequency	Axis	Below Rated	Above Rated	Below Rated	Above Rated
1P	x	125.2	6.2	1.0	8.8
	y	33.0	13.2	14.8	20.3
	z	31.9	38.2	12.2	16.4
2P	x	0.3	0.3	0.0	0.1
	y	0.8	2.0	0.8	0.6
	z	2.0	2.7	0.1	0.8
3P	x	0.1	0.4	0.1	0.5
	y	0.1	0.1	0.1	0.3
	z	0.0	0.4	0.4	0.5

Summary

Table 4.4 summarises the results for the steady case of MI. Immediately, it is apparent that the 1P harmonics show the most significant change based on magnitude, as well as wind speed and fault level trends. Additinally, it can be seen that the resonse at 1P force harmonic is the most sensitive in terms of magnitude difference and trends with wind speed and fault level. 2P and 3P harmonics on the other hand, show far less sensitive responses in comparison.

Table 4.4: Summary table for the case of MI at steady wind conditions

		MI Moment in LSS		MI Force in LSS	
Frequency	Axis	Below Rated	Above Rated	Below Rated	Above Rated
1P	x	M3	M1	F1+	F2
	y	M1	M1+	F3+	F4c
	z	M1	M1	F3+	F3c
2P	x	M1	M1	F1	N/A
	y	M1	M1	F1	F1
	z	M1	M1	F1	F1
3P	x	M1	M1	F1	F1
	y	M1	M1	F1	F1
	z	M1	M1	F1	F1

Yaw Misalignment

Table 4.5 shows the averaged results below and above rated wind speeds for the case of YM. From the table, it can be seen that primarily the 3P moment harmonics in y and z directions have the largest change in response to YM, with moment peaks reaching up to M2 level on average. While there are some peaks that appear at 1P and 2P harmonic, it is difficult to draw any conclusions from them, since they do not show any trends related to increasing with wind speed or fault level. Furthermore, 1P and 2P peaks are not very pronounced when plotted in comparison to the surrounding noise, shown in Figure C.13–C.18. With this, it can be concluded that the 3P moment harmonic in y and z can be used to characterise YM.

Table 4.5: Average Moment and Force Peak Difference in LSS Between a Healthy Rotor and a Rotor with YM, Steady Wind

		YM Moment LSS [kNm]		YM Force in LSS [kN]	
Frequency	Axis	Below Rated	Above Rated	Below Rated	Above Rated
1P	x	0.0	0.0	0.0	0.0
	y	0.0	0.1	0.0	0.0
	z	0.1	0.1	0.0	0.0
2P	x	0.4	0.1	0.0	0.2
	y	0.2	0.8	0.5	0.3
	z	1.7	1.4	0.0	0.0
3P	x	0.3	0.7	0.6	0.8
	y	52.9	51.9	0.2	0.1
	z	62.1	60.9	0.6	0.7

Summary

Table 4.6 summarises the results for the steady case of MYM. Immediately, it is apparent that the 1P and 2P harmonics show no significant changes based on magnitude, as well as wind speed and fault level trends. On the other hand, the 3P moment harmonics are much more sensitive to YM, with YMy and YMz harmonics showing the highest sensitivity in terms of wind speed and fault level trends and magnitude difference.

Table 4.6: Summary table for the case of YM at steady wind conditions

		YM Moment in LSS		YM Force in LSS	
Frequency	Axis	Below Rated	Above Rated	Below Rated	Above Rated
1P	x	N/A	N/A	N/A	N/A
	y	N/A	N/A	N/A	N/A
	z	N/A	N/A	N/A	N/A
2P	x	M1	M1	F1	F1
	y	M1	M1	F1	F1
	z	N/A	M1	N/A	F1
3P	x	M1	M1	F1+	F1+
	y	M2+	M2+	F1	F1
	z	M2+	M2+	F1	F1

4.2. Turbulent Wind Simulation Results

In this section, the turbulent wind simulation results are discussed. The turbulent wind simulations were conducted in a similar way to steady wind simulations, with the exception of using six turbulent wind seed files for each fault case, as was discussed in chapter 3. The results provided in this chapter are of the same format as in section 4.1, presenting moment and force peak change, between a healthy and a faulty rotor, in the x, y and z direction for each fault case, below and above rated speeds, averaged over the six seeds. The aim of this section is to highlight the differences in trends and magnitudes between steady and turbulent wind conditions. All relevant figures can be found in section B.2

4.2.1. Low Speed Shaft Moment

Figures B.7 – B.9 show the changes in moment peaks at 1P, 2P and 3P harmonics, respectively. For the 1P harmonic, it can be seen that the differences in trends and magnitude changes are minimal for all cases, in comparison to the steady results. The most significant change at this harmonic can be seen in PMy and PMz magnitude difference being slightly smaller than in the steady wind results. Similarly, for the 2P hamronic the differences between steady and turbulent results are minimal. The magnitude differences are largely the same. The trends are no longer seen for the cases of PMx, MIy, MIz and all directions of YM. Other cases see no significant changes. For the 3P harmonic, the PMy and PMz magnitude difference at above rated has decreased and the trends are no longer seen, when compared to the steady case. For MIy and MIz, the increasing trends with fault level have become slightly clearer. For YM, the magnitude difference remained similar, with wind speed trends being lost at above rated speeds for YMy and YMz directions. No significant change is observed for the remaining cases.

4.2.2. Low Speed Shaft Force

Figures B.10 – B.12 show the change in force peaks at 1P, 2P and 3P harmonics, respectively. For the 1P harmonic, the turbulent results appear to be similar to steady-state results in terms of magnitude difference. In terms of trends, the only difference is ovserved for below rated PMy and PMz gaining a more conistent positive trend with wind speed. For The 2P harmonic results show loss of wind speed trends for the case of PM, while the peaks for MI and YM disappear entirely. As for the 3P harmonic, the most apparent change is the loss of trends seen in the steady results, for all cases. The only exception to this is the above rated PMy keeping its increasing trend with wind speed.

4.2.3. Discussion and Comparison

This section contains the results from the turbulent wind simulations that have been summarised with an intent to highlight the trends and system responses to the three fault cases. This was done using the same procedure as for the steady wind results. After distributing the results into five bins, seen in Figure 3.5. As a result, a distribution similar to Figure 3.4 was obtained, with bins having the same thresholds for both moment and force. The color scheme and naming of the bins was kept the same, therefore Table 3.7 can be referred to this chapter, too. Additionally, the turbulent results are compared to the steady results.

Healthy

Table 4.7 shows the difference between average moments and forces in a healthy rotor at turbulent and steady wind conditions. The signals which increased in the turbulent results are highlighted in green, while the ones that decreased are highlighted in red. This was calculated by subtracting healthy steady peaks from healthy turbulent peaks. Then the mean below and above rated is calculated in each direction. From the table it can be seen that overall there is no change at 1P harmonic between turbulent and steady results. This difference is presented to highlight what effect turbulence brings, without the effect of rotor imbalances present. Small decrease in peak magnitude can be observed at 2P moment and force peaks in the y direction, as well as a small decrease in moment peaks in the z direction. On the other hand, the magnitude increases substantially for both moment an force at 3P, in all three directions. A very large increase in peak magnitude is seen at 3P moment about the y and z axis, which increases with wind speed.

Table 4.7: Average Moment and Force Peak Change in LSS Between Healthy Rotors in Turbulent and Steady Wind Conditions

		Healthy Moment LSS [kNm]		Healthy Force in LSS [kN]	
Frequency	Axis	Below Rated	Above Rated	Below Rated	Above Rated
1P	x	0.0	0.0	0.0	0.0
	y	-0.1	0.0	0.0	0.0
	z	0.0	0.0	0.0	0.0
2P	x	-0.8	0.0	0.0	0.0
	y	-1.2	-0.7	-1.9	-0.1
	z	-4.7	-0.4	0.0	0.0
3P	x	1.1	3.1	7.4	14.6
	y	659.4	1528.5	2.0	4.6
	z	633.1	1455.9	1.6	8.0

The increase in 3P harmonic could be explained by the way turbulence is modelled. In a steady wind profile, the wind velocity remains constant and is only present in the x direction, with velocity in the y and z direction equating to zero. However, in the turbulent wind profile, variance is added to the velocity to induce a degree of randomness. This results in a wind profile that has variable wind velocity in the x, y and z directions. The small velocity variability in the y and z directions results in the wind meeting the rotor at a skewed angle of attack. As mentioned in the previous chapter, a healthy rotor should only output peaks at 3P harmonic, since 1P and 2P harmonics cancel out. Therefore, an increase in 3P peaks could be caused by the variation in angle of attack.

Pitch Misalignment

Table 4.8 shows the averaged results below and above rated wind speeds for the case of PM, at turbulent wind conditions. Overall, little difference can be observed in comparison with steady results in Table 4.1, in terms of harmonic response. Similar trends can be observed, with the same harmonics being excited in all three directions. However, Table 4.9 gives a closer look what role turbulence plays on dynamic responses, in terms of peak magnitude. The difference was calculated by subtracting steady wind results from turbulent wind results, after which the mean peak differences between the two wind conditions were calculated using Equation 3.3 and Equation 3.4.

Table 4.8: Average Moment and Force Peak Change in LSS Between a Healthy Rotor and a Rotor with PM, Turbulent Conditions

		PM Moment in LSS [kNm]		PM Force in LSS [kN]	
Frequency	Axis	Below Rated	Above Rated	Below Rated	Above Rated
1P	x	50.1	11.0	10.1	41.1
	y	4389.2	8115.9	6.6	43.8
	z	4384.9	8209.6	5.8	35.7
2P	x	4.9	0.0	2.6	0.0
	y	92.3	307.8	2.7	4.6
	z	105.7	440.9	1.0	4.0
3P	x	1.2	0.1	0.6	0.3
	y	41.3	68.2	0.9	3.5
	z	47.7	65.8	0.5	0.0

From, Table 4.9 it can be seen that mostly there are small changes in peak magnitude, with most peaks showing a small increase. However, 1P and 3P moment peaks PMy and PMz, both below and above rated, show a much larger change. As mentioned previously, the effect of PM is aerodynamic by nature, meaning that the aerodynamic effect of turbulence could be acting in tandem with the aerodynamic effect of PM. Despite the fact that the 1P peak magnitude increases with fault level and wind speed both in steady and turbulent wind conditions, the magnitude is smaller overall in turbulent wind conditions. One possible reason for this decrease in 1P peak magnitude in the turbulent case could be the interaction between the angle change due to PM in the faulty blade and change in the inflow angle caused by the turbulence, resulting in a smaller moment produced by the faulty blade, in reference to Equation 2.12.

A significant increase in the 3P moment peaks, PMy and PMz, is observed. On average, these peaks are smaller in turbulent wind conditions than in steady wind conditions, as shown in Table 4.8 and Table 4.1. However, Table 4.7 indicates that turbulence generally leads to larger 3P peaks compared to steady wind. This suggests that turbulence increases the LSS 3P moment. Meanwhile, the presence of PM slightly reduces the 3P moment, meaning the moment from all three blades are slightly smaller under turbulent conditions when PM is present.

Table 4.9: Average Moment and Force Peak Change in LSS Between Turbulent and Steady Wind Conditions in a Rotor with PM

		PM Moment in LSS [kNm]		PM Force in LSS [kN]	
Frequency	Axis	Below Rated	Above Rated	Below Rated	Above Rated
1P	x	-0.1	0.7	4.2	3.4
	y	-100.9	-48.0	-0.4	-1.1
	z	-79.1	-123.7	-0.4	-1.2
2P	x	1.5	-1.1	0.4	-2.9
	y	-1.1	1.0	0.0	3.9
	z	0.8	1.3	0.6	2.0
3P	x	0.0	2.9	6.9	13.9
	y	629.0	1406.0	1.2	7.3
	z	592.2	1275.0	1.7	7.6

Summary

Table 4.10 summarises the results for the turbulent case of PM. Immediately, it can be see that all 1P moment and force cases show an increase in magnitude change with both fault level and wind speed, which is expected given the aerodynamic origin of 1P moment and force. Similar trends to the steady wind simulations can be seen in the 2P moment and force peaks, with minimal changes in magnitude, meaning that turbulence plays a small role in this fault case. The 3P moment peaks show smaller peak difference from healthy, which was mentioned previously.

Lastly, it is worth noting that some signals no longer increase with wind speed and/or fault level, comparing to the steady wind results. The signals are: PMx moment at 2P, PMy and PMz moments at 3P, PMx force at 2P and 3P, PMy force at 1P and 3P and PMz force at 1P, 2P and 3P One possible reason could be that the trends were lost during averaging of the 6 seeds, since different seeds produce slightly different results, due to variance in wind speed magnitude and direction. This was not the case for the steady wind data, since the variation between time windows is negligible. In addition, the small peak being mixed in with the noise could have averaged out, and with it, the trends seen in the steady case.

Table 4.10: Summary table for the case of PM in turbulent wind conditions

		PM Moment in LSS		PM Force in LSS	
Frequency	Axis	Below Rated	Above Rated	Below Rated	Above Rated
1P	x	M2+	M1+	F2+	F5+
	y	M5+	M5+	F2+	F5+
	z	M5+	M5+	F1+	F5+
2P	x	M1+	N/A	F1	N/A
	y	M2	M5	F1	F1
	z	M3	M5+	F1	F1
3P	x	N/A	M1	F1	F1
	y	M1	M2	N/A	F1+
	z	M1	M2	F1	F1

Mass Imbalance

Table 4.11 shows the averaged results below and above rated wind speeds for the case of MI, at turbulent wind conditions. Overall, little changes are observed in comparison to the steady conditions.The key signals of 1P MIx torque and 1P MIy and MIz forces experience minor increases in magnitude, as seen in in Table 4.12. Larger increases can be seen in 1P and 3P MIy and MIz moments.

An increase in 2P MIY and MIz moments can be seen. One possible explanation for this could be an increase variation of rotor speed, caused by turbulence. It was established in the previous chapter that the origin of 2P moment could be centripetal force, which is proportional to the square of rotor speed. Therefore, the variation in rotor speed could lead to slightly larger 2P moment peaks seen in the results. Lastly, an increase in 3P moment is caused by an increase in aerodynamic loading due to turbulence, which is also seen in the healthy and PM cases.

Table 4.11: Average Moment and Force Peak Change in LSS Between a Healthy Rotor and a Rotor with MI, Turbulent Conditions

		MI Moment in LSS [kNm]		MI Force in LSS [kN]	
Frequency	Axis	Below Rated	Above Rated	Below Rated	Above Rated
1P	x	125.4	6.2	0.0	9.6
	y	31.7	23.2	13.5	21.0
	z	36.9	32.9	12.7	17.4
2P	x	2.2	0.0	0.1	0.0
	y	6.1	6.3	2.1	0.0
	z	14.6	14.3	0.0	0.0
3P	x	0.0	0.0	0.1	0.2
	y	16.0	31.7	0.4	0.0
	z	20.4	13.8	0.0	0.0

Table 4.12: Average Moment and Force Peak Change in LSS Between Turbulent and Steady Wind Conditions in a Rotor with MI

		MI Moment in LSS [kNm]		MI Force in LSS [kN]	
Frequency	Axis	Below Rated	Above Rated	Below Rated	Above Rated
1P	x	0.2	0.0	-1.0	0.8
	y	-1.3	10.0	0.0	0.7
	z	5.0	-5.3	0.5	1.0
2P	x	-3.1	-0.3	-0.1	-0.1
	y	4.3	3.6	0.2	-0.7
	z	9.9	11.1	-0.1	-0.8
3P	x	1.4	2.7	7.3	13.9
	y	655.0	1524.6	1.1	4.5
	z	628.6	1452.6	1.9	7.9

Summary

Table 4.13 summarises the results for the turbulent case of MI. Overall, in comparison to the results from the steady wind condition simulation, seen in Table 4.13, there is little change in terms of difference in magnitude between healthy and MI results. However, some signals no longer increase with wind speed and/or fault level. These signals are: MIx moment at 2P and 3P, MIy moment and 1P, 2P and 3P, MIz moment at 2P and 3P, MIx force at 1P and 2P, MIy force at 2P and 3P and MIz force at 2P. Again, the probable cause of losing this trend is averaging the results of six turbulence seeds in tandem with peaks being surrounded by noise. That being said, the key signals like 1P MIy and MIz force peaks, as well as 1P MIx torque, still show similar trends to the steady case below and above rated speeds. This increases the confidence in using these signals to identify MI in the rotor.

Table 4.13: Summary table for the case of MI in turbulent wind conditions

		MI Moment in LSS		MI Force in LSS	
Frequency	Axis	Below Rated	Above Rated	Below Rated	Above Rated
1P	x	M3	M1	N/A	F2
	y	M1	M1	F3+	F4c
	z	M1	M1	F3+	F3c
2P	x	N/A	N/A	N/A	N/A
	y	M1	M1	N/A	N/A
	z	M1	M1	N/A	N/A
3P	x	N/A	N/A	F1	F1
	y	M1	M1	N/A	N/A
	z	M1+	M1	F1	F1

Yaw Misalignment

Table 4.14 shows the averaged results below and above rated wind speeds for the case of YM, at turbulent wind conditions. Overall, little changes are observed in comparison to the steady conditions. The small variations in 2P harmonic are mostly gone, similarly to other cases where noise was averaged out over multiple turbulence seeds. Lastly, slight increases in 3P YMy and YMz moments are observed.

From Table 4.15 it can be seen that there is an increase in 3P moment and force peak magnitudes, in all three directions, with 3P YMy and YMz moments experiencing the largest change. This is caused by an increased load due to turbulence, similar to other fault cases. Other than that, the differences are minor.

Table 4.14: Average Moment and Force Peak Change in LSS Between a Healthy Rotor and a Rotor with YM, Turbulent Conditions

		YM Moment LSS [kNm]		YM Force in LSS [kN]	
Frequency	Axis	Below Rated	Above Rated	Below Rated	Above Rated
1P	x	0.7	0.0	0.0	0.0
	y	0.0	0.0	0.0	0.0
	z	0.0	0.0	0.0	0.0
2P	x	0.6	0.0	0.6	0.0
	y	0.0	0.0	0.0	0.0
	z	0.0	0.0	0.0	0.0
3P	x	0.7	0.9	1.4	1.9
	y	76.3	89.3	0.5	1.4
	z	101.1	113.0	0.6	0.7

Table 4.15: Average Moment and Force Peak Change in LSS Between Turbulent and Steady Wind Conditions in a Rotor with YM

		YM Moment LSS [kNm]		YM Force in LSS [kN]	
Frequency	Axis	Below Rated	Above Rated	Below Rated	Above Rated
1P	x	0.7	0.0	0.0	0.0
	y	-0.1	-0.1	0.0	0.0
	z	-0.1	-0.1	0.0	0.0
2P	x	-1.4	-0.1	0.6	-0.2
	y	-1.4	-1.5	-2.4	-0.5
	z	-5.3	-1.7	0.0	0.0
3P	x	2.1	3.3	6.7	12.6
	y	684.5	1568.0	1.4	6.0
	z	680.7	1503.8	1.2	7.6

Summary

Table 4.16 summarises the results for the turbulent case of YM. Overall, only a few changes are seen in comparison to steady case results, seen in Table 4.6. Above rated 3P YMy and YMz moment peaks lost their increasing trend with wind speed, which is again probably caused by averaging of the six seed. Similarly, the increasing trend in wind speed for 3P YMx force is gone, too. Additionally, all 2P force and moment peaks observed in the steady case are now gone and do not appear in the FFT of the signal in any of the seeds.

Table 4.16: Summary table for the case of YM in turbulent wind conditions

		YM Moment LSS		YM Force in LSS	
Frequency	Axis	Below Rated	Above Rated	Below Rated	Above Rated
1P	x	N/A	N/A	N/A	N/A
	y	N/A	N/A	N/A	N/A
	z	N/A	N/A	N/A	N/A
2P	x	N/A	N/A	N/A	N/A
	y	N/A	N/A	N/A	N/A
	z	N/A	N/A	N/A	N/A
3P	x	M1	M1	F1	F1
	y	M2+	M2	F1	F1
	z	M2+	M3	F1	F1

4.3. Fault Detection and Characterisation

Given the results presented and analysed in section 4.1 and section 4.2, it is now possible to determine how the three rotor faults can be detected and distinguished from each other. To determine the most suitable signal to identify each fault, the following signal characteristics need to be considered: peak magnitude, trends with wind speed increase and trends with fault level increase. Additionally, the peak amplitude relative to noise should be considered. Signals with clearly pronounced high amplitude peaks would be easier to detect in a real-world scenario, as signals with smaller peaks mixed in with the noise can be misidentified. Furthermore, the results from both steady and turbulent cases need to be used to determine the most suitable signal for each rotor fault case. Lastly, it is also important to compare the results obtained in this work with the results obtained by [6]. Finding similarities in the results would improve their reliability.

To begin with, the difference between steady and turbulent wind conditions needs to be analysed. The key differences found in section 4.2 have shown that many signals have lost their trends with wind speed and/or fault level, with some signals even not showing up on the FFT. It was also seen in section 4.1 that these signals in particular have also had less pronounced peaks than those that maintained similar tendencies in the turbulent wind cases. This means that the peaks extracted by the algorithm have most likely been picked up from the noise surrounding that harmonic and averaged out over the six turbulence seeds. Therefore, it is safe to assume that these signals can be omitted from the signal selection process. Moreover, signals that maintained a trend between steady and turbulent results are more likely to accurately identify a specific rotor fault.

Now that majority of the signals have been discarded, it becomes much easier to match each remaining signal to each rotor fault case. To further narrow the list of potential candidate signals, signal magnitude should now be considered. Higher peak amplitudes of the FFT could imply that the system is more sensitive to a fault at that particular frequency. Therefore, signals with higher amplitude should be prioritised over signals with lower amplitude. For instance, PMx 1P moment displays consistent increasing trends with fault level and wind speed, both below and above rated speed, while having a clear FFT peak with high amplitude. However, it would make more sense to use 1P PMy and PMz moment signals instead, since they have all of the above-mentioned trends, but a much higher amplitude. That being said, replying on magnitude alone will not show the full picture. For example, 2P PMy and PMz moment at above rated speed both have an M5 level magnitude, but only PMz has a consistent increasing trend with wind speed, making PMz a better signal to use.

Lastly, similarities and differences with [6] need to be established. First of all, their results show a very clear increase in magnitude for PMy and PMz force and moment signals, increasing with wind speed and fault level, which is very similar to the results obtained in this work. Second, in their results, 1P MIx torque at below rated, and 1P MIy and MIz shear forces have experienced significant excitation, similar to what was observed in this work. The 1P MIx torque at below rated speed matches this work's results in particular, based on their description. The 1P MIy and MIz force trends, based on the plots provided, experience similar increasing wind speed and fault level trends at below rated speeds. However, at above rated speeds, they show an increasing trend with wind speed, while results in this work show a more constant wind speed trend, with only minor changes in magnitude. Third, 1P YM results similarly show insignificant changes in magnitude for most cases. The only exception being the 1P YMy force, which appeared to consistently increase for all wind speeds, whereas in this work no significant changes were observed.

One major difference is that the research in [6] does not look at harmonics other than 1P. Some signals have shown to have some degree of sensitivity at 2P (PM moment) or 3P harmonic (YM moment) in this work, with YM cases particularly showing significant magnitude changes at 3P moment harmonic. That being said, many 2P and 3P harmonics in PM and MI cases resulted in FFT peaks having a rather small amplitudes compared to the noise, meaning it would be difficult to justify choosing them over their 1P counterparts.

Decision Tree

Based on the above reasoning, the most sensitive signals have been identified for each case and the decision tree in Figure 4.7 has been produced. The decision determines which signals are the best identifier of a fault present in the rotor. Based on the results, it was noticed that many signals display different trends at above rated speeds. Therefore, the decision tree contains two paths at the beginning, one for below rated and one for above rated data.

The decision tree is designed to be used in a real-world scenario. For example, in a scenario where an operational WT's LSS moment (M) and force (F) data is collected to check whether any rotor imbalances are present. The data is analysed in the frequency domain and compared to the data of a reference turbine that is known to be healthy. The data is compared at the same wind speed, U. If an increase in magntiude is detected and it can be matched to one or more characteristic signals of a rotor imbalance derived in this work, then the fault can be characterised. Additionally, the characteristic trends with wind speed are also taken into account to increase fault characterisation accuracy. The characteristic trends with fault level are not taken into account in the decision tree, since it would be difficult to measure accurately the exact fault level in a real world scenario.

The decision tree is constructed in a way which eliminates the possibility of misidentifying the fault, by characterising the faults in the order: PM-MI-YM. For instance, both PM and MI cases have 1P force harmonics present in the output, which can be used to identify either of the faults in the rotor. To eliminate the possibility of mischaracterisation, the presence of PM needs to be checked first by checking whether PMy or PMz 1P moment harmonic increases with wind speed. While 1P MIy and MIz moment harmonics are also present, their magnitude is much smaller than that of 1P PM moments, and they do not have a clear increasing trend with wind speed, unlike PMy and PMz harmonics. This therefore lowers the probability of misidentifying MI as PM, and vice versa.

For PM, the signals were narrowed down to two: PMy and PMz 1P moment harmonics. Either one of them can be used to identify PM in the rotor, since both signals produce very similar response, namely large magnitude change which increases with wind speed. These signals can be used both below and above rated wind speeds, since the trends remain the same and the magnitude keeps increasing. 1P PMx torque and thrust could also be used, but since these harmonics also appear in 1P MIx torque and thrust it could lead to misidentification. 2P and 3P harmonics were not considered due to higher amount of noise surrounding the extracted peaks and a lack of consistent wind speed trends.

For MI, the signals were also narrowed down to two: MIy and MIz 1P force harmonics. Similarly to the signals chosen for PM identification, either of the two could be used below and above rated. 1P MIx torque and thrust signals were not considered to not confuse them with PM. 2P and 3P harmonics have not shown consistent trends or high enough peak amplitudes to be considered.

Lastly, for YM the signals were also narrowed down to two: YMy and YMz moment harmonics, where either of which could be used below and above rated. Other signals have not shown any wind speed trends, so they were not considered. This completes the decision tree and it is now possible to identify whether either of the three rotor faults, PM, MI or YM, are present.

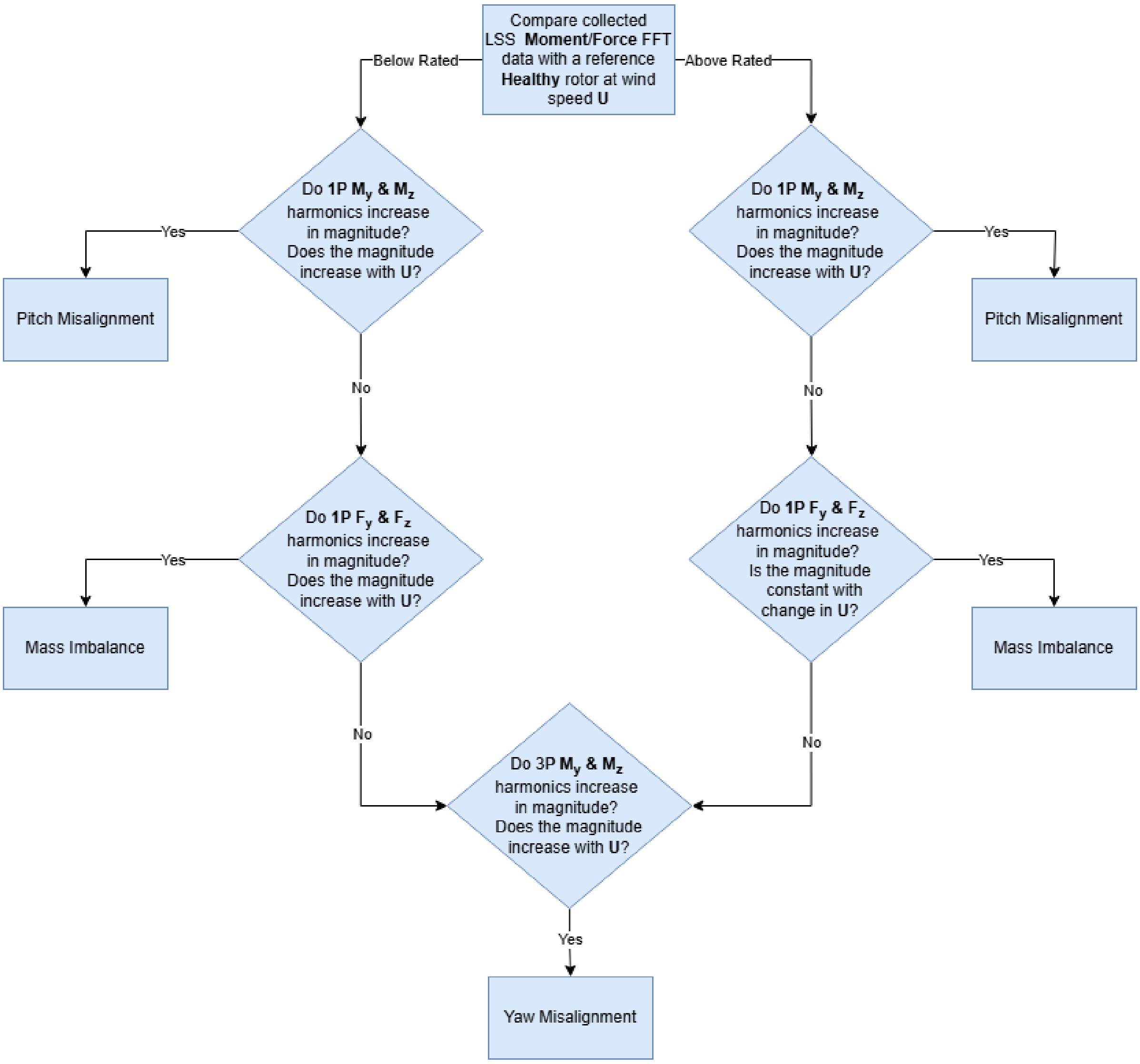

Figure 4.7: Rotor Fault Characterization Decision Tree

5 Conclusions

With the wind industry growing rapidly to meet the world's demand for clean energy, it is more important than ever to address underlying costs posed by O&M of WTs. Detecting rotor faults in time through remote techniques may reduce O&M costs of a WT, as well as reduce the risk of turbine failure. This work investigated ways to remotely characterise and identify WT rotor imbalances based on dynamic loads produced by the rotor. This chapter provides answers to the questions posed in chapter 1.

Main Research Question: ***Can common wind turbine rotor faults be detected and characterised, based on the dynamic system responses, under faulty operating conditions?***

Based on the findings of this research, it can be concluded that it is possible to detect and characterise three different rotor imbalances from one another. This was achieved by simulating the WT under healthy and faulty conditions at different combinations of environmental conditions and fault levels. The output signals were later analysed in the frequency domain, clearly showing the difference in dynamic responses of the rotor to each type of rotor imbalance. The decision tree proposed in the results section characterises each rotor imbalance based on signals' magnitudes and wind speed trends, while taking into account scenarios where similar behaviour is observed in multiple imbalance cases. The findings therefore show that it is feasible to detect a faulty rotor remotely following the steps proposed by the decision tree, whilst also being able to characterise what type of fault it is before arriving on site to provide maintenance, saving time and reducing costs.

In turn, the sub-questions can also be answered:

- ***Which output signals can be used to detect faults present in the rotor, and what signal characteristics should be considered in the process?***

  This work focused primarily on analysing quantitative data sets, including moment and force output signals in the LSS. It was found that LSS moment and force signals can be used to detect the presence of rotor imbalance and can be used to differentiate one imbalance type from another, when analysed in the frequency domain. Moreover, it was found that it is not sufficient to solely rely on FFT peak magnitudes because imbalances had some moment and/or force harmonic peaks in common, making it difficult to distinguish one imbalance from another. Therefore, analysing trends, such as wind speed and fault level trends, can help distinguish between different rotor imbalances. Overall, it was found that LSS moment signals have shown the clearest and most consistent trends that could be used to characterise pitch and yaw misalignments, while LSS force signals were more reliable at characterising mass imbalance.

  Moreover, it was also found that it is important to consider a wide range of harmonics to more accurately characterise each imbalance type. For PM and MI, relying solely on the 1P harmonic would be sufficient to detect and differentiate one from another. However, for the YM case, the 3P moment harmonic showed to be a much better identifier than both 1P and 2P harmonics. Thus, considering harmonics other than 1P, the most common harmonic found in literature, can improve rotor imbalance characterisation accuracy.

- ***To what extent can rotor fault conditions be differentiated from another, based on the dynamic responses of a wind turbine?***

  As it was seen in the results, each type of rotor imbalance produced a distinct set of outputs with unique characteristics specific to that imbalance type. The difference between the outputs of each imbalance case was primarily seen in the signals that were excited, the excitation magnitude, and the wind speed and fault level trends present in the data. PM and MI fault cases had some signals in common with similar trends, making it possible to mislabel one imbalance for another. That being said, the differences in the output signals were sufficient to correctly characterise each signal and differentiate one from the other, which is also true for the case of YM.

- ***How are wind turbine's dynamic system responses influenced by a change in the wind speed, under healthy and faulty conditions?***

  In this work's approach, healthy and faulty WT rotors have been modelled under six different wind speeds, three below rated and three above rated, to see what effect wind speed has on the system's dynamic responses. From the results, it was seen that higher wind speeds posed a higher aerodynamic load on the rotor. The higher loads, in turn, enhanced the system responses to the imbalance, seen in the larger FFT peak amplitudes in harmonics respective to each type of imbalance tested. The clearest positive wind speed trends were observed in 1P moments, 1P forces and 3P moments in y and z directions for PM, MI and YM, respectively. In a healthy rotor, an increase in wind speed results in higher 3P force and moment harmonic amplitudes in all three directions, while the 1P and 2P harmonics remain unchanged.

- ***What effects do turbulent environmental conditions have on a wind turbine's dynamic system responses?*** In comparison to steady wind, turbulent wind added noise into the output, making it easier to distinguish peaks from noise in the FFTs, since the majority of the noise averaged out over multiple turbulence seeds. In addition, turbulent wind resulted in higher 3P harmonic peak loads in all healthy and faulty cases, and smaller 1P loads in the PM case. Other cases show little to change in magnitude. Additionally, some wind speed and fault level trends have been lost due to averaging. However, the signals used for imbalance characterisation kept the same trends observed in the cases with steady wind.

Overall, this work successfully demonstrated that common wind turbine rotor imbalances can be detected and characterised based on the dynamic system response. This is achieved by simulating various rotor imbalances with different combinations of environmental conditions and fault levels, and analysing the output in the frequency domain.

6 Recommendations

While the results in this thesis have been promising, there are areas where this work can be further improved on. This chapter aims to highlight the limitations of this work and provide recommendations on how future works could build upon the findings of this thesis.

To begin with, the first big limitation of this work is that it only considered three cases of rotor imbalance: PM, MI and YM. While these rotor faults are common in WTs, they by far not the only issues that could be present, such as: surface cracking, delamination, surface erosion and more. Unlike PM, YM and some cases of MI (e.g.icing), faults like surface cracking may grow and worsen over time. All of this together leads to questioning whether it is possible to detect and characterise other types of rotor faults using the methodology presented in this thesis. In addition, it is also important to find an accurate way to model other types of rotor faults, that can properly represent the dynamic and aerodynamic effects they pose on the system [60].

Furthermore, another important factor to consider when modelling and analysing other rotor faults is what type of dynamic responses can be expected from them. While this work has shown that frequency analysis in the 1P-3P harmonic range is enough to distinguish between PM, MI and YM, other types of rotor faults have not been explored, and higher order harmonics have not been considered. Therefore, this result is limited by the fact that other rotor faults, like blade cracking or delamination, could give dynamic responses too similar to PM, MI or YM, making it difficult to distinguish between them, compromising the robustness and accuracy of this method. With this, it is therefore recommended to explore the dynamic effects of other types of rotor faults and imbalances to build a more robust method of remote rotor fault detection and characterisation. In addition, it is also recommended to review a wider range of harmonics in order to build a more complete model.

Another limitation of this thesis is that rotor imbalances were only modelled one at a time and one blade at a time. In a real world scenario, nothing prevents a WT rotor from having multiple blades being affected by one or multiple imbalances at the same time. In cases with multiple imbalances could potentially result in a different dynamic response, compared to the cases addressed in this thesis, which again makes this method of fault detection and characterisation less robust. Therefore, in addition to exploring other types of rotor faults and imbalances, it is also recommended to model multiple different combinations of faults and imbalances acting at the same time, to further increase the robustness of the fault characterisation method, or develop a better method entirely.

The method discussed in this thesis has been tested on the DTU RWT 10MW model in OpenFAST. While both the model and the software are extensively used in research, it is important to check whether similar results can be achieved on different WT models and/or software. In addition, collecting data from a real world model could provide further insights on the matter.

Lastly, the data analysed in this thesis only included x-y-z moments and forces in the LSS. While the faults have been successfully characterised based on these signals, it is still difficult to say whether the LSS is the best location to collect the data. Moreover, it still remains unclear which type of sensor would have to be used to collect LSS force and moment data. Furthermore, would it be possible to install such a sensor on WTs that are already operating, or does a turbine need to account for a monitoring system during the design phase instead? It also raises the question on how large and expensive the sensor/monitoring system would have to be, since these types of sensors are not used in the industry. All of the above are important questions that need to be answered to determine the most accurate, feasible and cost-effective way to implement remote fault characterisation methods into a WT.

References

[1] NASA. *What Is Climate Change?* 2024. URL: https://science.nasa.gov/climate-change/what-is-climate-change/.

[2] Pablo Rosado Hannah Ritchie and Max Roser. "Total Wind Capacity". In: *Out World in Data* (2023). URL: https://ourworldindata.org/grapher/cumulative-installed-wind-energy-capacity-gigawatts?country=OWID_WRL~OWID_ASI~OWID_NAM~OWID_SAM~OWID_AFR~OWID_EUR.

[3] D. Li, S. M. Ho, and G. Song et. al. "A review of damage detection methods for wind turbine blades". In: *Smart Materials and Structures* (2015). DOI: https://doi.org/10.1088/0964-1726/24/3/033001.

[4] C. Dao, B. Kazemtabrizi, and C. Crabtree. "Wind turbine reliability data review and impacts on levelised cost of energy". In: *Wind Energy* (2019). DOI: https://doi.org/10.1002/we.2404.

[5] Y. Du et. al. "Damage detection techniques for wind turbine blades: A review". In: *Mechanical Systems and Signal Processing* (2020). DOI: https://doi.org/10.1016/j.ymssp.2019.106445.

[6] F. C. Mehlan and A. R. Nejad. "Rotor imbalance detection and diagnosis in floating wind turbines by means of drivetrain condition monitoring". In: *Renewable Energy* (2023). DOI: https://doi.org/10.1016/j.renene.2023.04.102.

[7] M. Dimitrova et.al. "A Survey on Non-Destructive Smart Inspection of Wind Turbine Blades Based on Industry 4.0 Strategy". In: *Applied Mechanics* (2022). DOI: https://doi.org/10.3390/applmech3040075.

[8] L. Fauteux and N. Jolin. "Drone solutions for wind turbine inspections". In: *Nergica: Gaspé* (2018). URL: https://nergica.com/wp-content/uploads/%C3%89tude-Drones_Version-finale_EN_17-d%C3%A9cembre-2018.pdf.

[9] S. Cacciola et al. "Detection of rotor imbalance, including root cause, severity and location". In: *Journal of Physics: Conference* (2016). DOI: https://doi.org/10.1088/1742-6596/753/7/072003.

[10] J. Ledoux, S. Riffo, and J. Salomon. "Analysis of the Blade Element Momentum Theory". In: *SIAM Journal on Applied Mathematics* (2021). DOI: https://doi.org/10.1137/20M133542X.

[11] A. Viré M. Zaaijer. *Introduction to wind turbines: physics and technology*. 2022.

[12] Julian Genov and M Todorov. "DYNAMICAL STRESSES IN THE HIGH CLASS WIND TURBINE BLADES CAUSED BY THE VERTICAL WIND SPEED GRADIENT. PART 1 -AERODYNAMICAL LOADS". In: *Journal of the Balkan Tribological Association* (2019). URL: https://www.researchgate.net/publication/336900115_DYNAMICAL_STRESSES_IN_THE_HIGH_CLASS_WIND_TURBINE_BLADES_CAUSED_BY_THE_VERTICAL_WIND_SPEED_GRADIENT_PART_1_-AERODYNAMICAL_LOADS.

[13] C.L. Bottasso and S. Cacciola. "Model-independent periodic stability analysis of wind turbines". In: (2014). URL: https://re.public.polimi.it/retrieve/e0c31c0e-16e9-4599-e053-1705fe0aef77/Model-independent%20periodic%20stability%20analysis%20of%20wind%20turbines_11311-802526_Bottasso.pdf.

[14] Andreas Heege and Jan Hemmelmann. "Matching experimental and numerical data of dynamic power train loads by modeling of defects". In: *Wind Energy* (2013).

[15] Barry Manz. "Wind Turbines: Tiny Sensors Play Big Role". In: *Mouser Electronics* (2024). URL: https://eu.mouser.com/applications/tiny-Sensors-Role-in-Wind-Turbines/.

[16] SCADA international. “What is SCADA?” In: (2024). URL: https://scada-international.com/what-is-scada/#:~:text=What%20does%20SCADA%20stand%20for,data%20from%20the%20industrial%20equipment..

[17] Zaid Allal et al. “Wind turbine fault detection and identification using a two-tier machine learning framework”. In: *Intelligent Systems with Applications* (2024). DOI: https://doi.org/10.1016/j.iswa.2024.200372. URL: https://www.sciencedirect.com/science/article/pii/S2667305324000486.

[18] Carlos Quiterio Gómez Muñoz and Fausto Pedro García Márquez. “A New Fault Location Approach for Acoustic Emission Techniques in Wind Turbines”. In: *Energies* (2016). URL: https://www.mdpi.com/1996-1073/9/1/40.

[19] B. Eftekharnejad et al. “The application of spectral kurtosis on Acoustic Emission and vibrations from a defective bearing”. In: *Mechanical Systems and Signal Processing* (2011). DOI: https://doi.org/10.1016/j.ymssp.2010.06.010.

[20] Seung-Hyun Moon et al. “Application of machine learning to an early warning system for very short-term heavy rainfall”. In: *Journal of Hydrology* (2019). DOI: https://doi.org/10.1016/j.jhydrol.2018.11.060.

[21] Simscale. “What is Vibration Analysis”. In: (2024). URL: https://www.simscale.com/docs/simwiki/fea-finite-element-analysis/what-is-vibration-analysis/.

[22] Kusnick J, Adams D.E., and Griffith T. “Wind turbine rotor imbalance detection using nacelle and blade measurements”. In: *Wind Energy* (2014). DOI: https://doi.org/10.1002/we.1696.

[23] Xiyun Yang et al. “Image recognition of wind turbine blade damage based on a deep learning model with transfer learning and an ensemble learning classifier”. In: *Renewable Energy* (2021). ISSN: 0960-1481. DOI: https://doi.org/10.1016/j.renene.2020.08.125.

[24] Abhishek Reddy et al. “Detection of Cracks and damage in wind turbine blades using artificial intelligence-based image analytics”. In: *Measurement* (2019). DOI: https://doi.org/10.1016/j.measurement.2019.07.051.

[25] Lei Zhang et al. “Road crack detection using deep convolutional neural network”. In: *2016 IEEE International Conference on Image Processing (ICIP)*. 2016. DOI: 10.1109/ICIP.2016.7533052.

[26] Yajie Yu et al. “Image-based damage recognition of wind turbine blades”. In: *2017 2nd International Conference on Advanced Robotics and Mechatronics (ICARM)*. 2017. DOI: 10.1109/ICARM.2017.8273153.

[27] Afef Fekih, Hamed Habibi, and Silvio Simani. “Fault Diagnosis and Fault Tolerant Control of Wind Turbines: An Overview”. In: *Energies* (2022). URL: https://www.mdpi.com/1996-1073/15/19/7186.

[28] Pierre Tchakoua et al. “Wind Turbine Condition Monitoring: State-of-the-Art Review, New Trends, and Future Challenges”. In: *Energies* (2014). URL: https://www.mdpi.com/1996-1073/7/4/2595.

[29] M. Bertelè, C. L. Bottasso, and S. Cacciola. “Automatic detection and correction of pitch misalignment in wind turbine rotors”. In: *Wind Energy Science* (2018). DOI: https://doi.org/10.5194/wes-3-791-2018.

[30] GL. “Guideline for the Certification of Wind Turbines”. In: *Germanischer Lloyd Industrial Services, Hamburg, Germany* (2010).

[31] M. Saathoff et al. “Effect of individual blade pitch angle misalignment on the remaining useful life of wind turbines”. In: *Wind Energy Science* (2021). DOI: https://doi.org/10.5194/wes-6-1079-2021.

[32] G.R. Hübner et al. “Detection of mass imbalance in the rotor of wind turbines using Support Vector Machine”. In: *Renewable Energy* (2021). DOI: https://doi.org/10.1016/j.renene.2021.01.080.

[33] Niebsch J., Ramlau R., and Nguyen T. T. “Mass and Aerodynamic Imbalance Estimates of Wind Turbines”. In: *Energies* (2010). DOI: https://doi.org/10.3390/en3040696.

[34] A. Grunwald, C. Heilmann, and M. Melsheimer. “Improved quality of rotor balancing measurements throughcriteria from the guideline VDI-3834-1:2015”. In: *WindEurope* (2016). URL: https://windeurope.org/summit2016/conference/allfiles2/349_WindEurope2016presentation.pdf.

[35] B. Jing et al. “Improving wind turbine efficiency through detection and calibration of yaw misalignment”. In: *Renewable Energy* (2020). DOI: https://doi.org/10.1016/j.renene.2020.07.063.

[36] Roohollah Fadaeinedjad, Gerry Moschopoulos, and Mehrdad Moallem. “The Impact of Tower Shadow, Yaw Error, and Wind Shears on Power Quality in a Wind–Diesel System”. In: *IEEE Transactions on Energy Conversion* (2009). DOI: https://doi.org/10.1109/TEC.2008.2008941.

[37] Anna Stawska et al. “Demand response: For congestion management or for grid balancing?” In: *Energy Policy* (2021). DOI: https://doi.org/10.1016/j.enpol.2020.111920. URL: https://www.sciencedirect.com/science/article/pii/S0301421520306315.

[38] ANSI. “Wind Turbine Standards”. In: (2024). URL: https://webstore.ansi.org/industry/energy/wind-turbine.

[39] Clare Davies, Andy Logan, and Alun Roberts. “Job Roles in Offshore Wind”. In: (2020). URL: https://www.bluegemwind.com/wp-content/uploads/2020/07/Job-Roles-in-Offshore-Wind.pdf.

[40] Kenneth Lawani, Billy Hare, and Iain Cameron. “Evaluating Wind Technicians Performance on Safety Critical Rescue Steps”. In: *Management, Procurement and Law* (2018). DOI: https://doi.org/10.1680/jmapl.18.00002.

[41] Tyler Stehly and Patrick Duffy. “2021 Cost of Wind Energy Review”. In: *NREL* (2022). URL: https://www.nrel.gov/docs/fy23osti/84774.pdf.

[42] Sustainability Performance Office. “U.S. Department of Energy Sustainability Reporting”. In: (2024). URL: https://www.energy.gov/management/osp/us-department-energy-sustainability-reporting.

[43] U.S Department of Labor. “Government Performance and Results Act (GPRA)”. In: (). URL: https://www.dol.gov/agencies/eta/performance/goals/gpra.

[44] Samet Ozturk and Vasilis Fthenakis. “Predicting Frequency, Time-To-Repair and Costs of Wind Turbine Failures”. In: *Energies* (2020). DOI: 10.3390/en13051149. URL: https://www.mdpi.com/1996-1073/13/5/1149.

[45] Katherine Ortegon, Loring F. Nies, and John W. Sutherland. “The Impact of Maintenance and Technology Change on Remanufacturing as a Recovery Alternative for Used Wind Turbines”. In: *Procedia CIRP* (2014). DOI: https://doi.org/10.1016/j.procir.2014.06.042. URL: https://www.sciencedirect.com/science/article/pii/S221282711400465X.

[46] FRANCOIS BESNARD. “On Optimal Maintenance Management for Wind Power Systems”. In: (2009). URL: https://kth.diva-portal.org/smash/record.jsfpid=diva2%3A282226&dswid=5977.

[47] IEA. *Renewables 2023. Analysis and forecasts to 2028*. 2024. URL: https://www.iea.org/reports/renewables-2023/Electricity.

[48] SP Global. “Offshore Wind on the Horizon”. In: (2021). URL: https://www.spglobal.com/en/research-insights/featured/markets-in-motion/offshore-wind.

[49] Christian Bak et al. *The DTU 10-MW Reference Wind Turbine*. Danish Wind Power Research 2013 ; Conference date: 27-05-2013 Through 28-05-2013. 2013.

[50] NREL. In: (2024). URL: https://www.nrel.gov/wind/nwtc/openfast.html#:~:text=OpenFAST%20is%20an%20open%2Dsource,now%20take%20place%20in%20OpenFAST..

[51] NREL. “OpenFAST Documentation”. In: (2024). URL: https://openfast.readthedocs.io/en/main/.

[52] P.J. Moriarty and A.C. Hansen. “AeroDyn Theory Manual”. In: (2005). URL: https://www.nrel.gov/docs/fy05osti/36881.pdf.

[53] J. M. Jonkman and M. L. Buhl Jr. “FAST User’s Guide”. In: *NREL* (2005).

[54] Andy Platt, Bonnie Jonkman, and Jason Jonkman. “InflowWind User’s Guide”. In: *National Wind Technology Center* (2016).

[55] Liang Li et al. “Wind field effect on the power generation and aerodynamic performance of offshore floating wind turbines”. In: *Energy* (2018). DOI: 10.1016/j.energy.2018.05.183.

[56] Craig MacEachern and İlhami Yıldız. *Comprehensive Energy Systems*. 2018, pp. 665–701.

[57] IEC. “IEC 61400-1 Ed.3: Wind turbines - Part 1: Design requirements”. In: (2005).

[58] B.J. Jonkman and L. Kilcher. “TurbSim User’s Guide: Version 1.06.00”. In: (2012). URL: https://www.nrel.gov/wind/nwtc/assets/pdfs/turbsim.pdf.

[59] W.T. Cochran et al. “What is the fast Fourier transform?” In: (1967). DOI: 10.1109/PROC.1967.5957.

[60] Qian Xiong et al. “Dynamic characteristic analysis of rotating blade with breathing crack”. In: *Mechanical Systems and Signal Processing* (2023). DOI: https://doi.org/10.1016/j.ymssp.2023.110325. URL: https://www.sciencedirect.com/science/article/pii/S0888327023002327.

A

MATLAB Code: Peak Extraction Algorithm

```
%This function extracts FFT peaks from WT output data, sorts them and averages the values peaks over 60 one-minute time windows
function [Average_Peak] = auto_peaks(signal,T,data,prominance,columns)

%input parameters
load(data)
cols = columns; %analyse select columns to save compute time
input = eval(signal); %input .mat file, first 400s discarded
prom = prominance; %disregard small peaks

%loop for 60 one-minute windows
for jj = 1:60

Fs = 1/T; % Sampling frequency 40Hz
L = 60/T; %length of signal 1 minute
start = jj; % starting time of peak extraction
finish =jj+1; % ending time of peak extraction) (+1 minute)
time_window = [start*L:finish*L]; % 1 minute time interval
order = mean(input(time_window,1))./(60); %RPM/60 -> normilze frequency ( Hz -> 1P,2P,3P...)


%%
h1 = fft(input(time_segment,cols)); %FFT of input.

%Source: MATLAB FFT command documentation (Single-Sided Amplitude Spectrum )
f = (Fs*(0:(L/60))/L)./order ;%normalize frequency Hz-> 1P,2P,3P etc
P2_h = 2*abs(h1./L);
P1_h = P2_h(1:length(f),:);
P1_h(2:end-1) = 2*P1_h(2:end-1);
peaks = [];

for i = 1:length(cols)
    prominence = prom*max(P1_h(:, i)); % filter out peaks smaller than prom*max value (e.g. 10%)

```

```
    Amplitude = [];
    Frequency = [];
    [Amplitude, Frequency] = findpeaks(P1_h(:, i),f,'MinPeakProminence', prominence);

   %fill matrix with extracted FFT peaks and frequencies
   peaks(1:numel(Amplitude), 2*i-1) = Amplitude;
   peaks(1:numel(Frequency), 2*i) = Frequency;

end


%filters out repeated values
for ii = 1:2:7
    for k = 2:length(peaks(:,1))
        if peaks(k,ii)== peaks(k-1,ii) %prevents duplicates of peaks 2 rows in a row
           peaks(k,ii) = 0;
           peaks(k,ii+1) = 0;
        elseif peaks(k-1,ii+1)== peaks(k,ii+1) % same as above
            peaks(k,ii+1)= 0;
        peaks(k,ii) = 0;
        end
    end
% Filter which removes all rows with zeros.
zero_rows = all(peaks == 0, 2);
idx = find(~zero_rows, 1, 'last');
% If there are no non-zero rows, keep the original matrix
if isempty(idx)
    peaks = peaks;
else
    % Keep rows until the last group of zero rows
    peaks = peaks(1:idx, :);
end
Peaks{jj} = peaks; %save peak-frequency pairs of each time window into a cell (repeated for each time window)
end
end

%% make matrices in the cell the same size
%Find the maximum size among all matrices
maxSize = [0, 0];
for i = 1:length(Peaks)
    sizeMatrix = size(Peaks{i});
    maxSize = max(maxSize, sizeMatrix);
end
%adds a row a zeros to a matrix if the size of the matrix is smaller than
%the largest matrix (e.g. converts 3by8 matrix to a 4by8 matrix by adding row of 0s)
for i = 1:length(Peaks)
Peaks{i}=paddata(Peaks{i},maxSize);
end
sorted_Peaks = cell(1, length(Peaks));
for i = 1:length(Peaks)
    matrix = Peaks{i};

```

```
    num_rows = size(matrix, 1);
    num_cols = size(matrix, 2);

    % Sort even columns
    for j = 1:2:num_cols
        [~, idx] = sort(matrix(:, j+1));
        matrix(:, j:j+1) = matrix(idx, j:j+1);
    end

    sorted_Peaks{i} = matrix;
end


%this for loop is responsible for making sure the matrix with least zeros
%is first. Helps the summation for loop below to work and no go above array limits.
for i = 1:length(jj)
    if length(find(~sorted_Peaks{1,1})) > length(find(~sorted_Peaks{1,i}))
        temp = sorted_Peaks{1,1};
        sorted_Peaks{1,1} = sorted_Peaks{1,i};
        sorted_Peaks{1,i} = temp;
        break;
    end
end

%% summation
added = sorted_Peaks{1};
addition_count = ones(size(added)); % counts number of times each corresponding pair was added with one another

% Add peaks-frequency pairs of all time windows. Ensures addition of
% correct peak-frequency pairs (e.g 1P adds with 1P and not with 2P or 3P)
for i = 2:length(sorted_Peaks)
    for j = 1:height(sorted_Peaks{1})
        for k = 2:2:width(sorted_Peaks{1})
            if sorted_Peaks{1}(j,k) == sorted_Peaks{i}(j,k)
                added(j,k-1) = added(j,k-1) + sorted_Peaks{i}(j,k-1);
                added(j,k) = added(j,k) + sorted_Peaks{i}(j,k);
                addition_count(j,k-1) = addition_count(j,k-1) + 1;
                addition_count(j,k) = addition_count(j,k) + 1;
            elseif sorted_Peaks{1}(j,k) ~= sorted_Peaks{i}(j,k) && j < height(sorted_Peaks{1}) && sorted_Peaks{1}(j,k) == sorted_Peaks{i}(j+1,k)
                added(j,k-1) = added(j,k-1) + sorted_Peaks{i}(j+1,k-1);
                added(j,k) = added(j,k) + sorted_Peaks{i}(j+1,k);
                addition_count(j,k-1) = addition_count(j,k-1) + 1;
                addition_count(j,k) = addition_count(j,k) + 1;
            elseif sorted_Peaks{1}(j,k) ~= sorted_Peaks{i}(j,k) && j > height(sorted_Peaks{1}) &&  sorted_Peaks{1}(j,k) ~= sorted_Peaks{i}(j-1,k)
                % add 0 if conditions are not met
                added(j,k-1) = added(j,k-1) + 0;
                added(j,k) = added(j,k) + 0;
                addition_count(j,k-1) = addition_count(j,k-1) + 1;
            else
               added(j,k-1) = added(j,k-1) + 0;
```

```
                added(j,k) = added(j,k) + 0;
            end
        end
    end
end
Average_Peak = added ./ addition_count

end
```

B

Absolute Difference in Peak Magnitude Between Healthy and Faulty Rotor

B.1. Steady State Bar Plots

LSS Moment

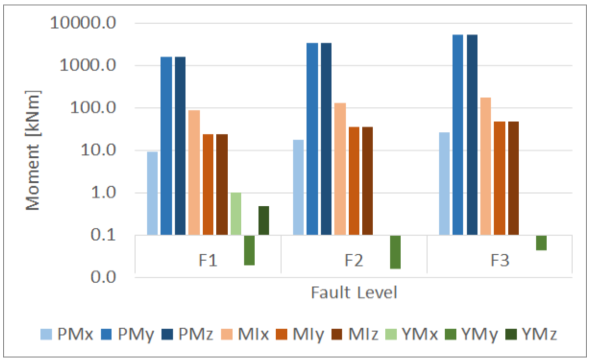

(a) 1P LSS Moment Below Rated U_1 = 4m/s

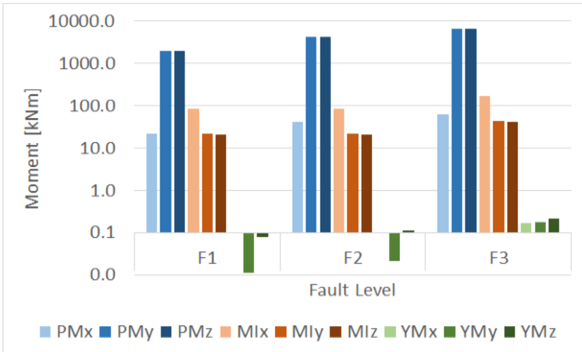

(b) 1P LSS Moment Below Rated U_2 = 7m/s

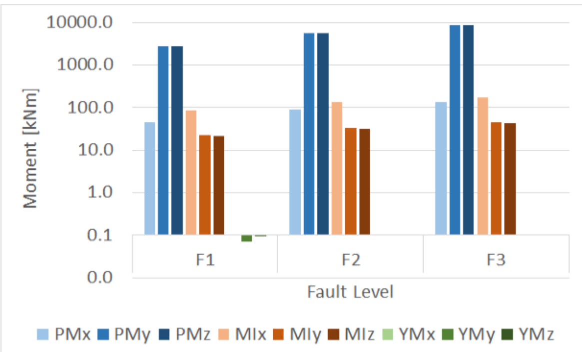

(c) 1P LSS Moment Above Rated U_3 = 10m/s

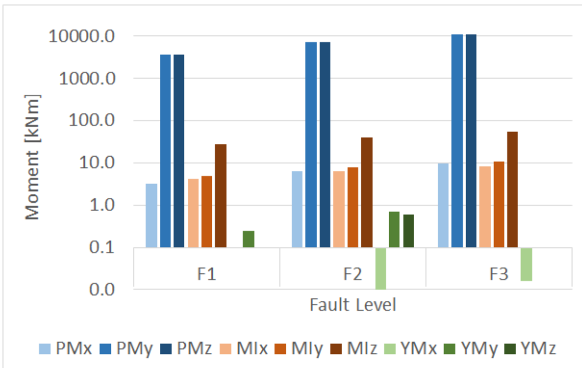

(d) 1P LSS Moment Above Rated U_4 = 12m/s

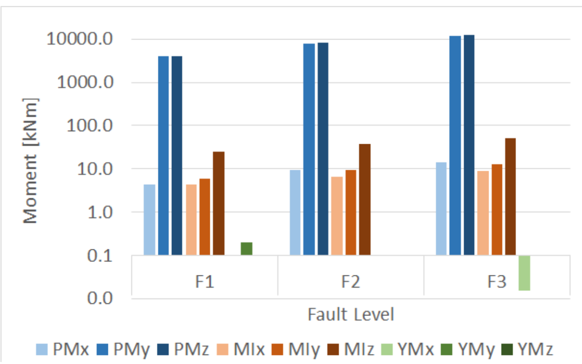

(e) 1P LSS Moment Above Rated U_5 = 14m/s

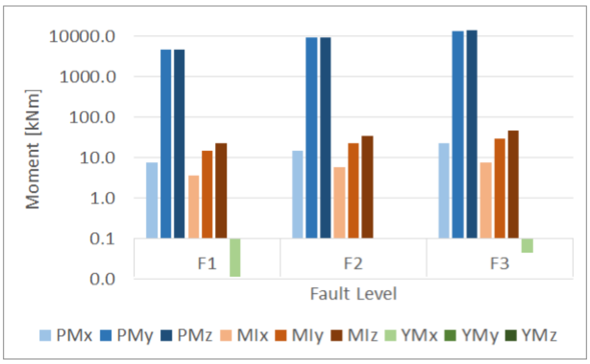

(f) 1P LSS Moment Above Rated U_6 = 20m/s

Figure B.1: Absolute Change in LSS Moment Below and Above Rated Wind Speeds at 1P Frequency in Steady Wind Conditions

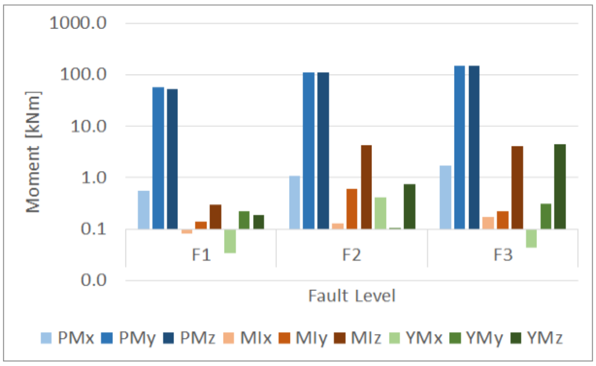

(a) 2P LSS Moment Below Rated U_1 = 4m/s

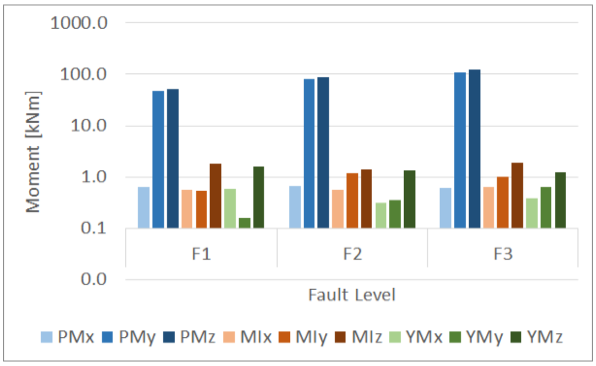

(b) 2P LSS Moment Below Rated U_2 = 7m/s

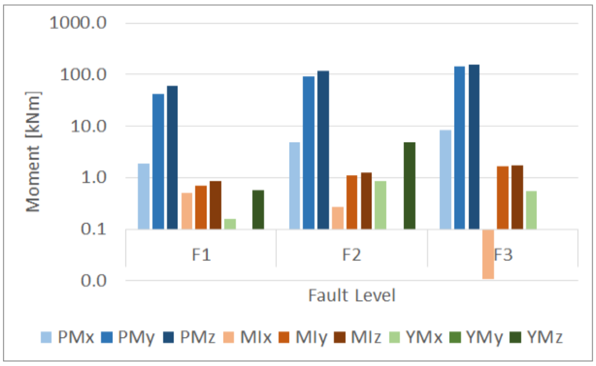

(c) 2P LSS Moment Above Rated U_3 = 10m/s

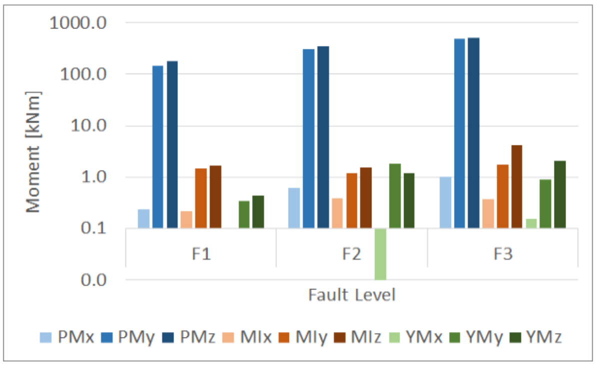

(d) 2P LSS Moment Above Rated U_4 = 12m/s

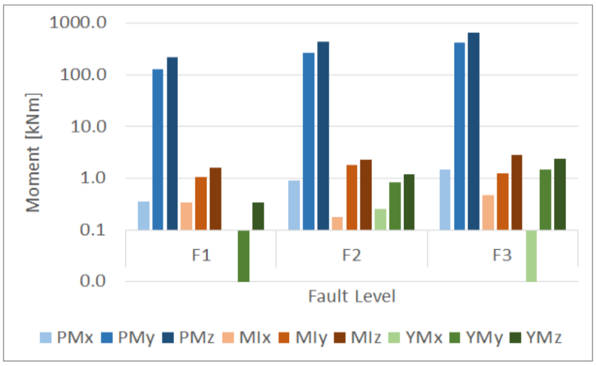

(e) 2P LSS Moment Above Rated U_5 = 14m/s

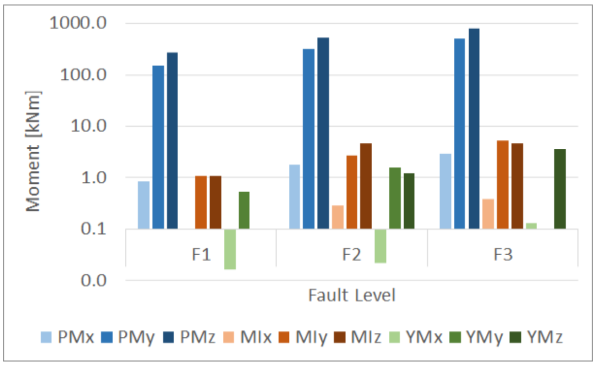

(f) 2P LSS Moment Above Rated U_6 = 20m/s

Figure B.2: Absolute Change in LSS Moment Below and Above Rated Wind Speeds at 2P Frequency in Steady Wind Conditions

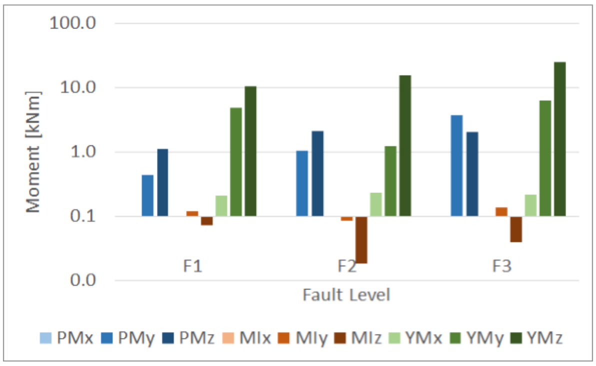

(a) 3P LSS Moment Below Rated U_1 = 4m/s

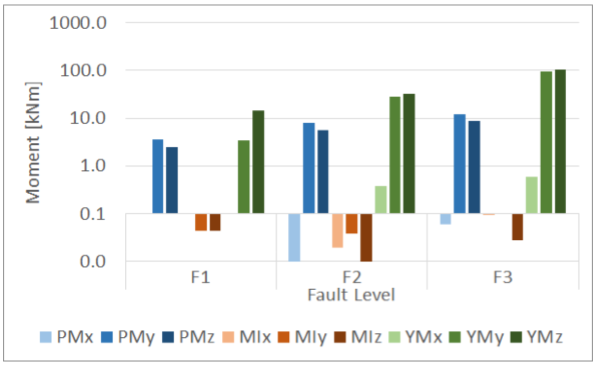

(b) 3P LSS Moment Below Rated U_2 = 7m/s

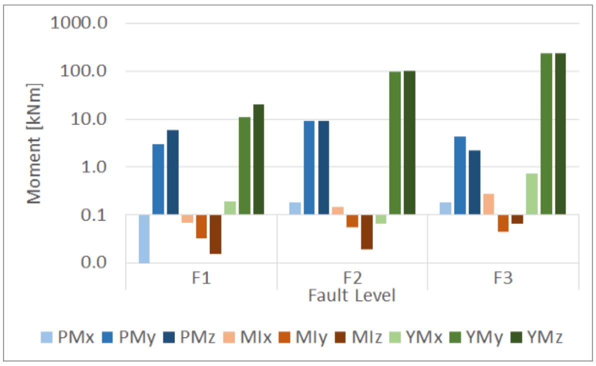

(c) 3P LSS Moment Above Rated U_3 = 10m/s

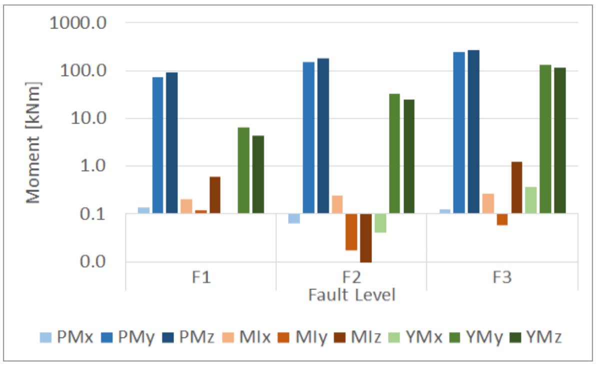

(d) 3P LSS Moment Above Rated U_4 = 12m/s

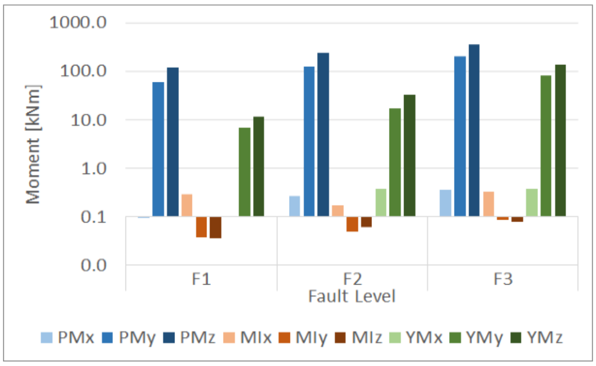

(e) 3P LSS Moment Above Rated U_5 = 14m/s

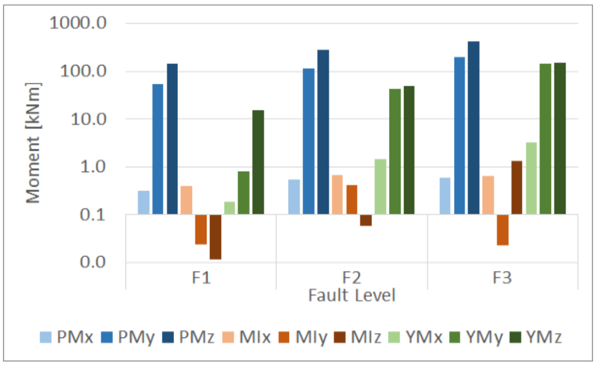

(f) 3P LSS Moment Above Rated U_6 = 20m/s

Figure B.3: Absolute Change in LSS Moment Below and Above Rated Wind Speeds at 3P Frequency in Steady Wind Conditions

LSS Force

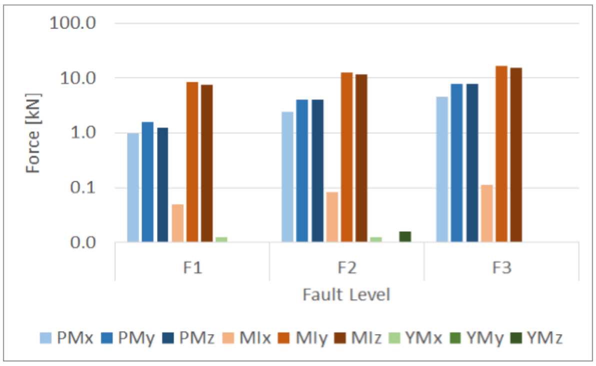

(a) 1P LSS Force Below Rated U_1 = 4m/s

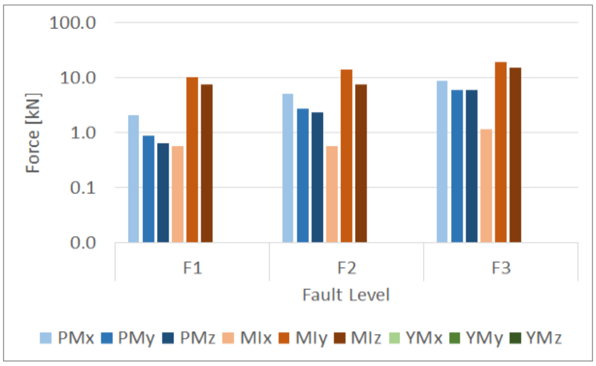

(b) 1P LSS Force Below Rated U_2 = 7m/s

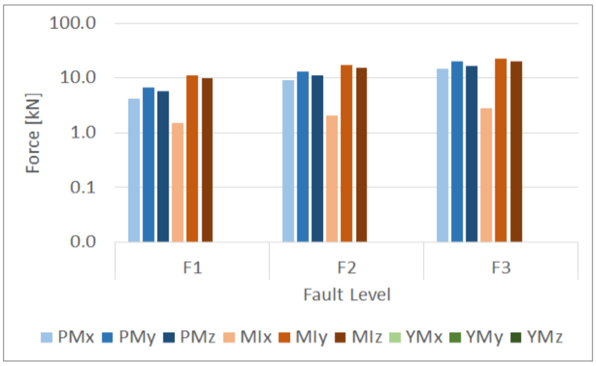

(c) 1P LSS Force Above Rated U_3 = 10m/s

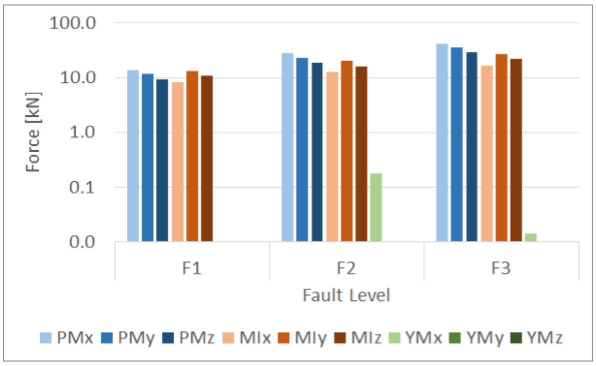

(d) 1P LSS Force Above Rated U_4 = 12m/s

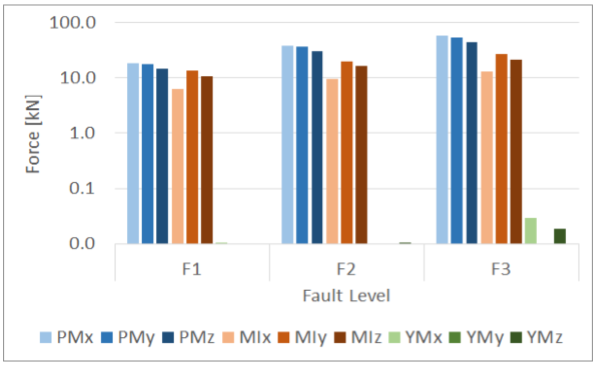

(e) 1P LSS Force Above Rated U_5 = 14m/s

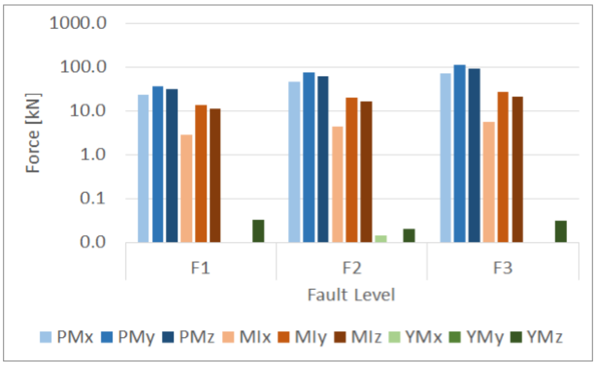

(f) 1P LSS Force Above Rated U_6 = 20m/s

Figure B.4: Absolute Change in LSS Force Below and Above Rated Wind Speeds at 1P Frequency in Steady Wind Conditions

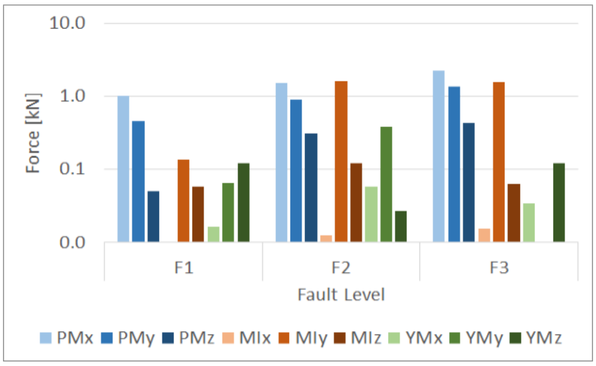

(a) 2P LSS Force Below Rated U_1 = 4m/s

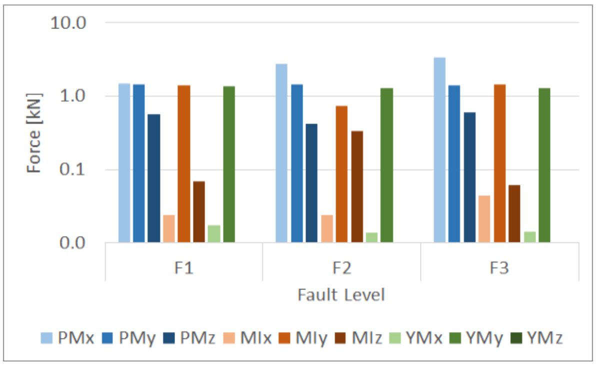

(b) 2P LSS Force Below Rated U_2 = 7m/s

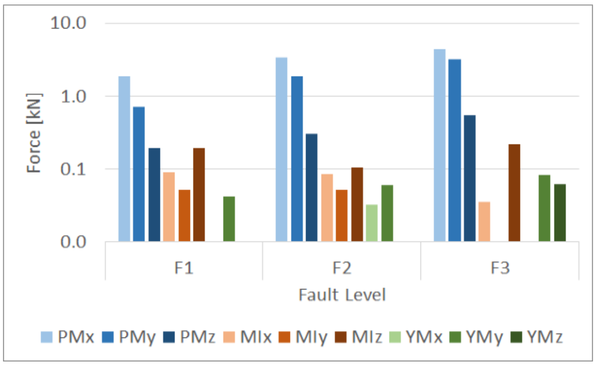

(c) 2P LSS Force Above Rated U_3 = 10m/s

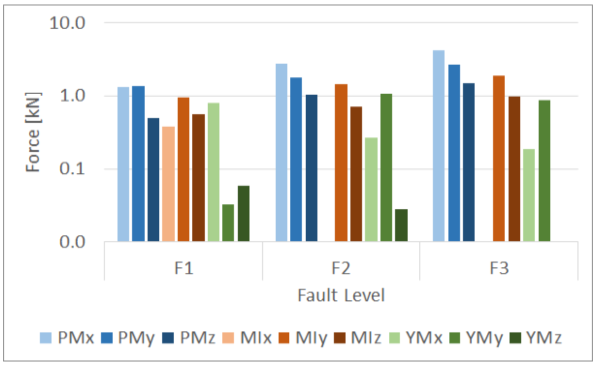

(d) 2P LSS Force Above Rated U_4 = 12m/s

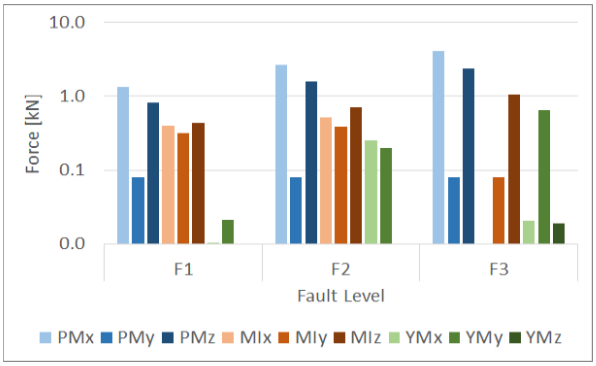

(e) 2P LSS Force Above Rated U_5 = 14m/s

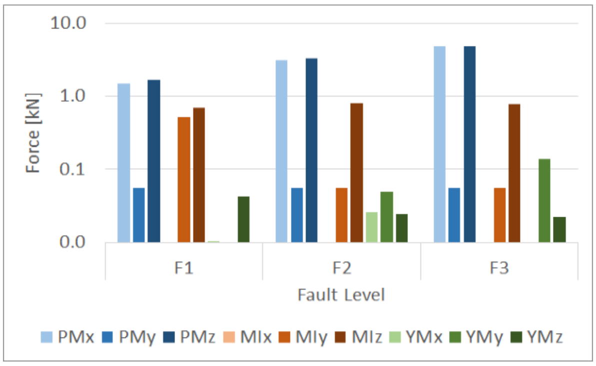

(f) 2P LSS Force Above Rated U_6 = 20m/s

Figure B.5: Absolute Change in LSS Force Below and Above Rated Wind Speeds at 2P Frequency in Steady Wind Conditions

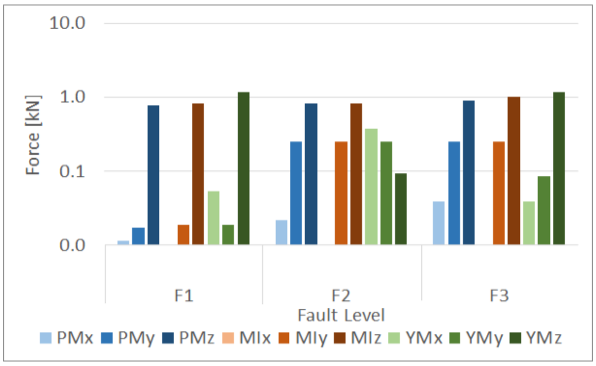

(a) 3P LSS Force Below Rated U_1 = 4m/s

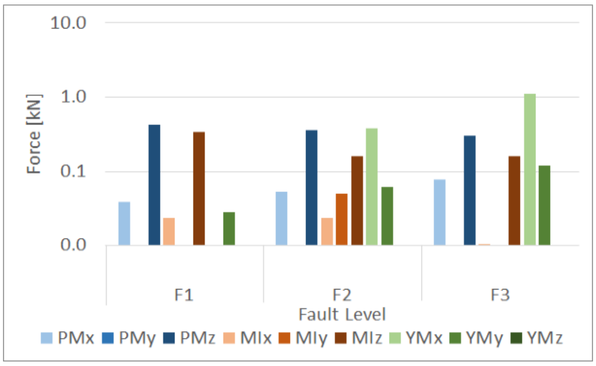

(b) 3P LSS Force Below Rated U_2 = 7m/s

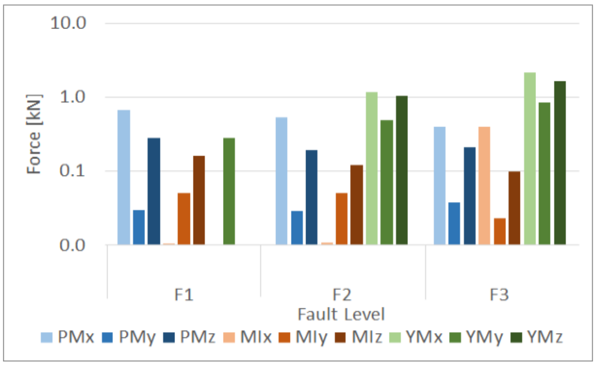

(c) 3P LSS Force Above Rated U_3 = 10m/s

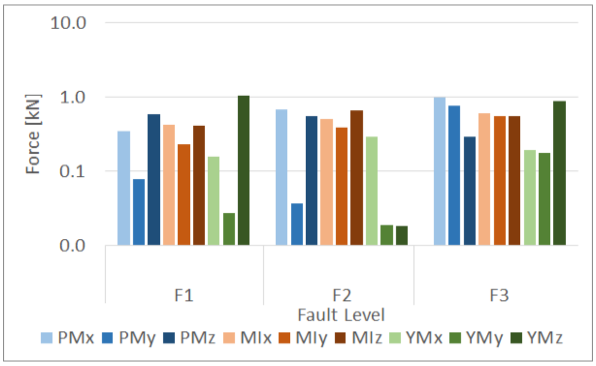

(d) 3P LSS Force Above Rated U_4 = 12m/s

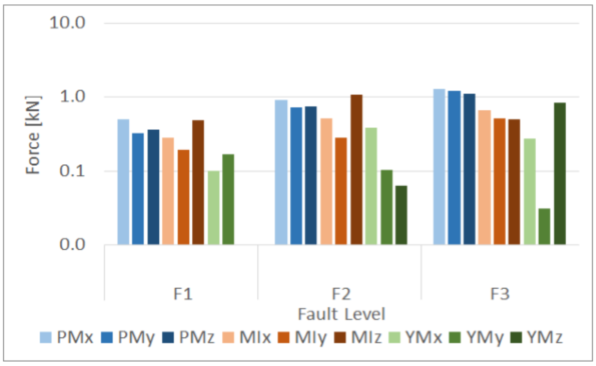

(e) 3P LSS Force Above Rated U_5 = 14m/s

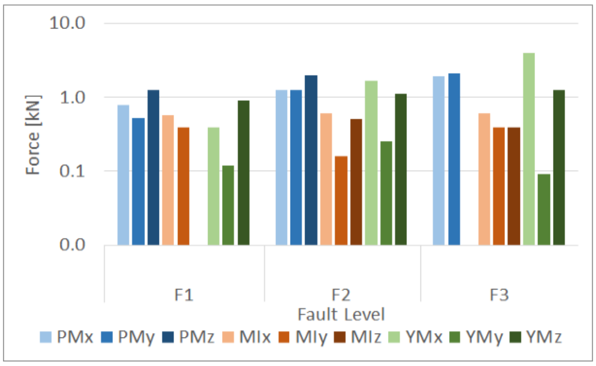

(f) 3P LSS Force Above Rated U_6 = 20m/s

Figure B.6: Absolute Change in LSS Force Below and Above Rated Wind Speeds at 3P Frequency in Steady Wind Conditions

B.2. Turbulent State Bar Plots

LSS Moment

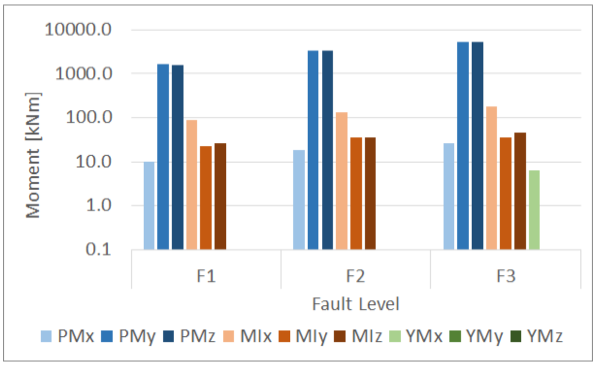

(a) 1P LSS Moment Below Rated U_1 = 4m/s

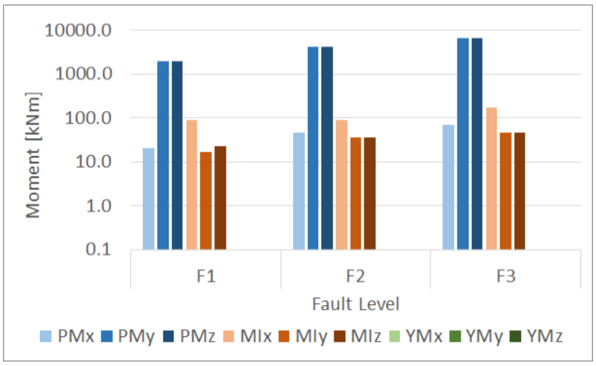

(b) 1P LSS Moment Below Rated U_2 = 7m/s

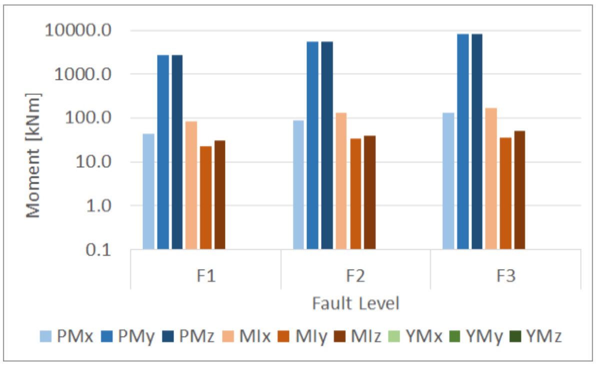

(c) 1P LSS Moment Above Rated U_3 = 10m/s

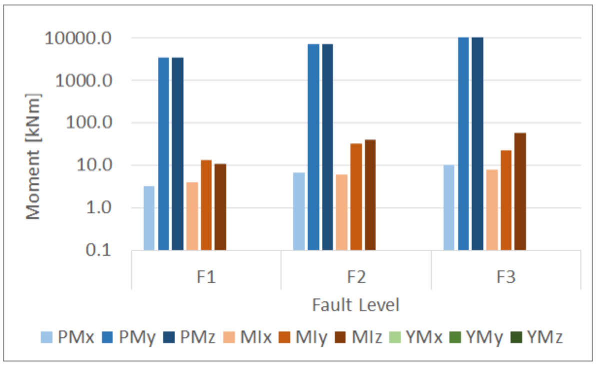

(d) 1P LSS Moment Above Rated U_4 = 12m/s

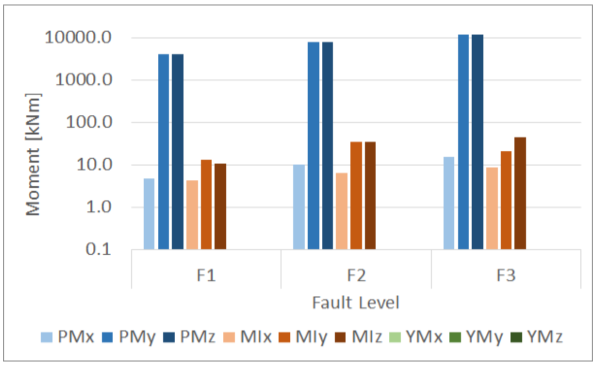

(e) 1P LSS Moment Above Rated U_5 = 14m/s

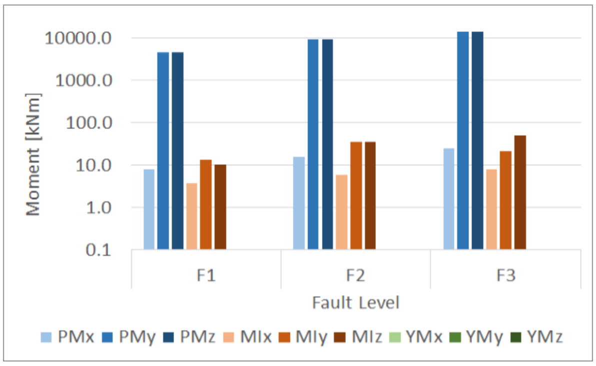

(f) 1P LSS Moment Above Rated U_6 = 20m/s

Figure B.7: Absolute Change in LSS Moment Below and Above Rated Wind Speeds at 1P Frequency in Turbulent Wind Conditions

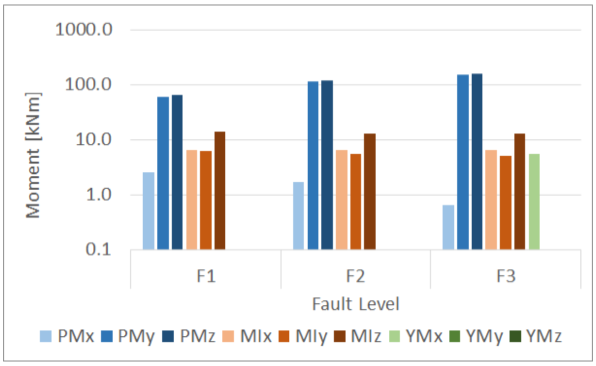

(a) 2P LSS Moment Below Rated U_1 = 4m/s

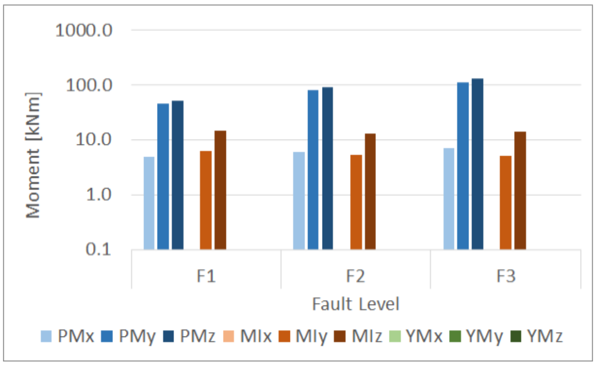

(b) 2P LSS Moment Below Rated U_2 = 7m/s

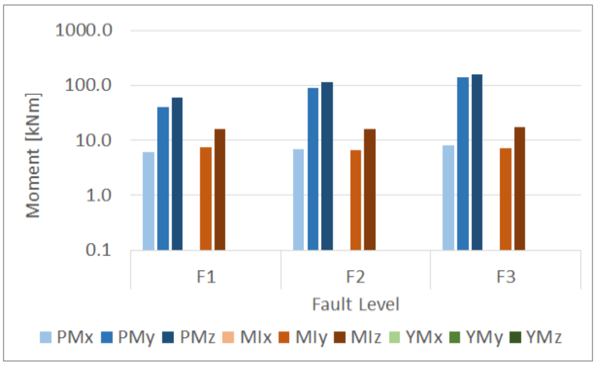

(c) 2P LSS Moment Above Rated U_3 = 10m/s

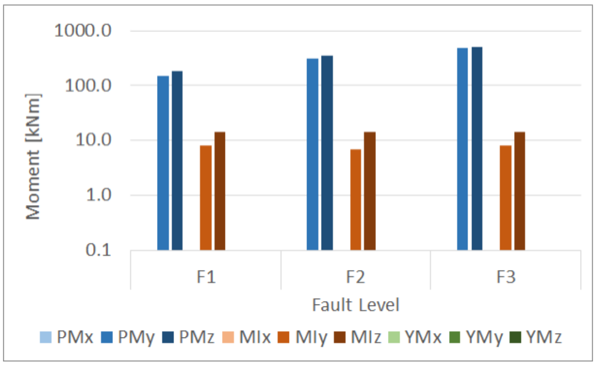

(d) 2P LSS Moment Above Rated U_4 = 12m/s

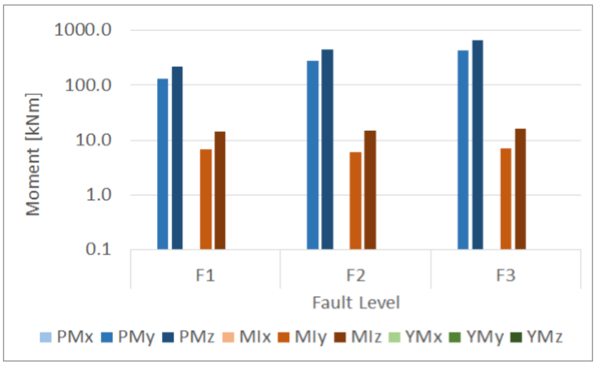

(e) 2P LSS Moment Above Rated U_5 = 14m/s

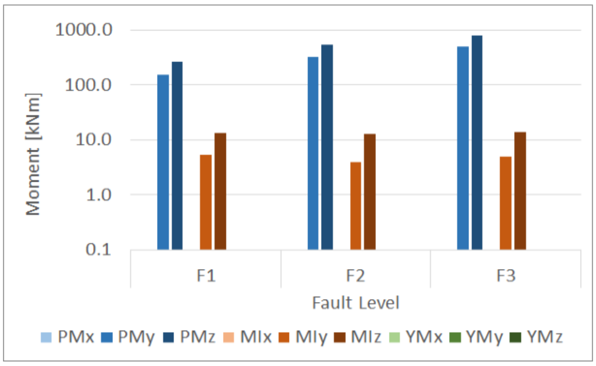

(f) 2P LSS Moment Above Rated U_6 = 20m/s

Figure B.8: Absolute Change in LSS Moment Below and Above Rated Wind Speeds at 2P Frequency in Turbulent Wind Conditions

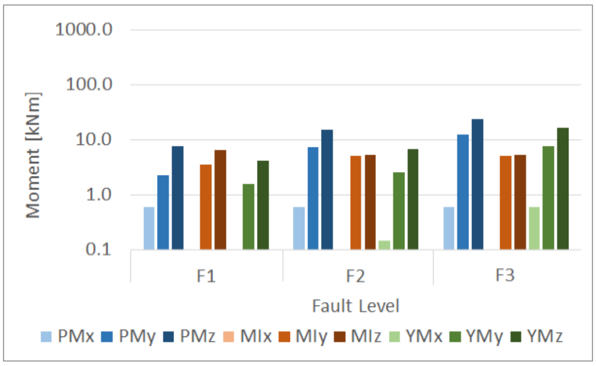

(a) 3P LSS Moment Below Rated U_1 = 4m/s

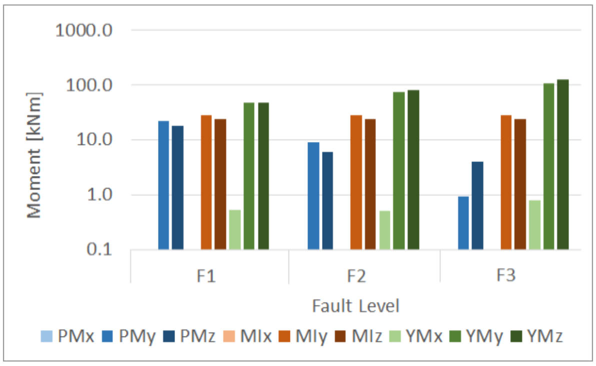

(b) 3P LSS Moment Below Rated U_2 = 7m/s

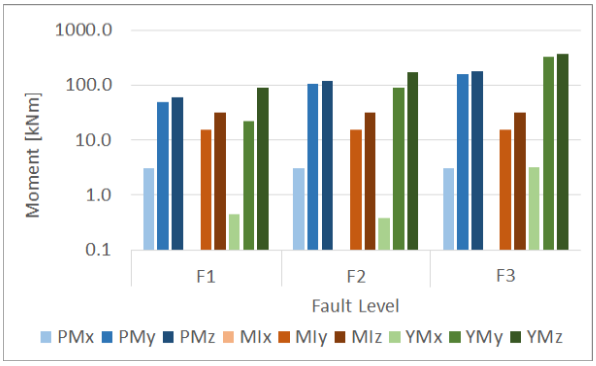

(c) 3P LSS Moment Above Rated U_3 = 10m/s

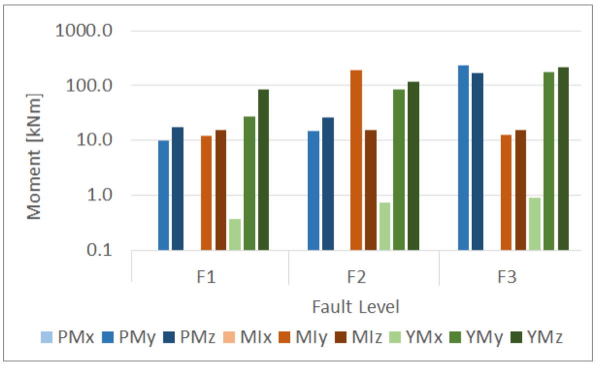

(d) 3P LSS Moment Above Rated U_4 = 12m/s

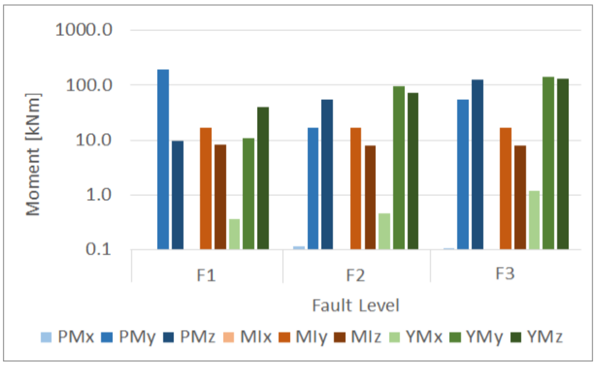

(e) 3P LSS Moment Above Rated U_5 = 14m/s

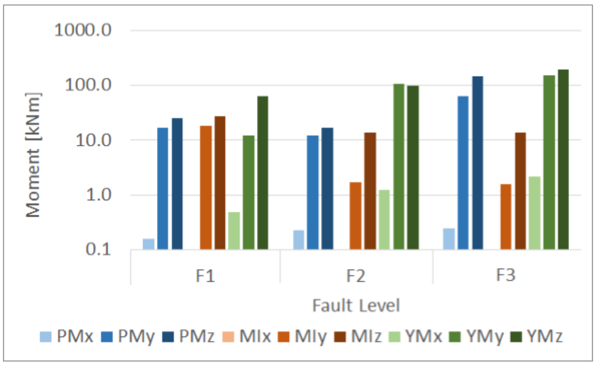

(f) 3P LSS Moment Above Rated U_6 = 20m/s

Figure B.9: Absolute Change in LSS Moment Below and Above Rated Wind Speeds at 3P Frequency in Turbulent Wind Conditions

LSS Force

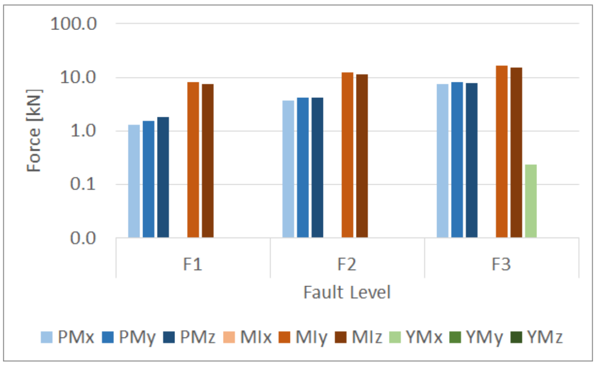

(a) 1P LSS Force Below Rated U_1 = 4m/s

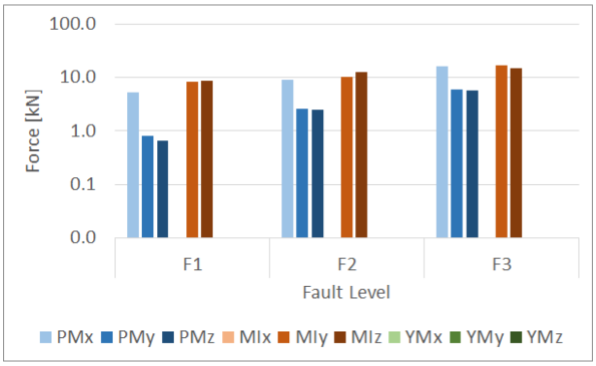

(b) 1P LSS Force Below Rated U_2 = 7m/s

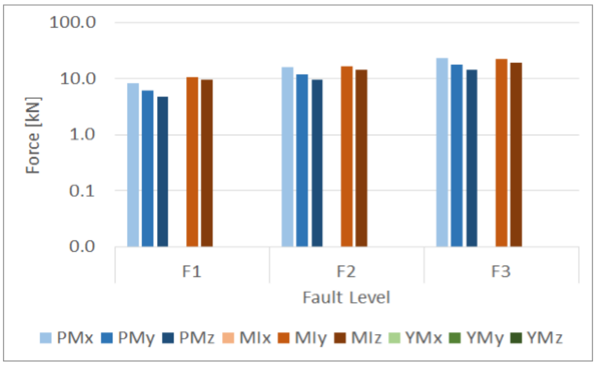

(c) 1P LSS Force Above Rated U_3 = 10m/s

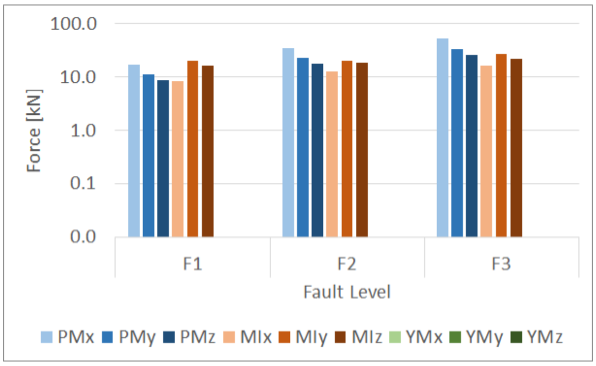

(d) 1P LSS Force Above Rated U_4 = 12m/s

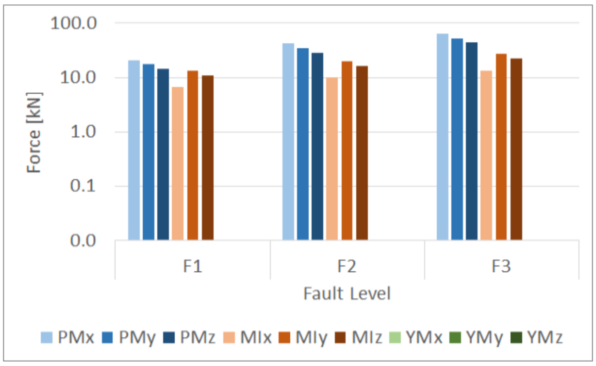

(e) 1P LSS Force Above Rated U_5 = 14m/s

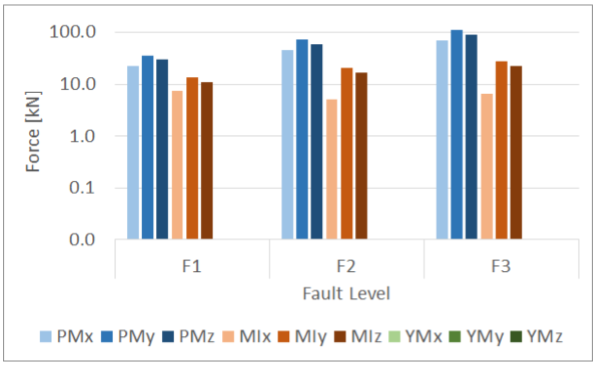

(f) 1P LSS Force Above Rated U_6 = 20m/s

Figure B.10: Absolute Change in LSS Force Below and Above Rated Wind Speeds at 1P Frequency in Turbulent Wind Conditions

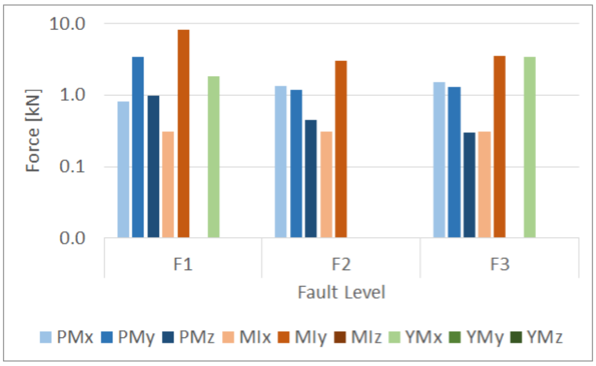

(a) 2P LSS Force Below Rated U_1 = 4m/s

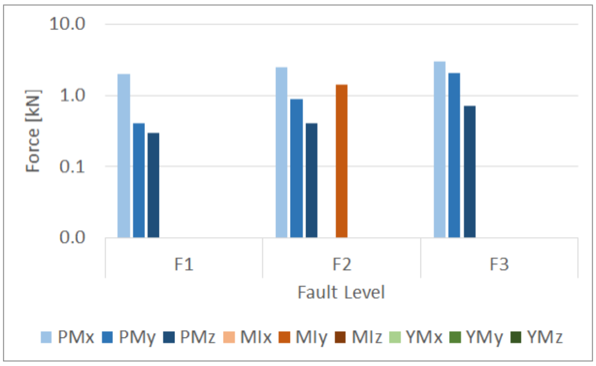

(b) 2P LSS Force Below Rated U_2 = 7m/s

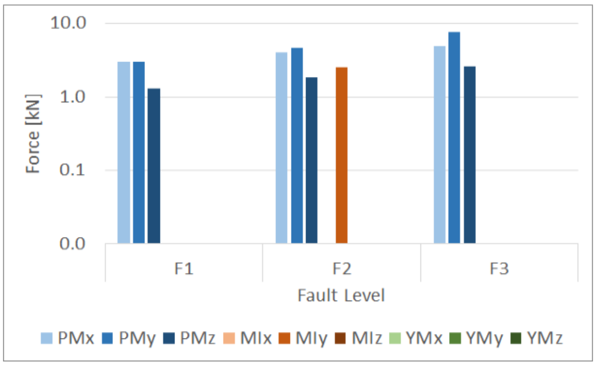

(c) 2P LSS Force Above Rated U_3 = 10m/s

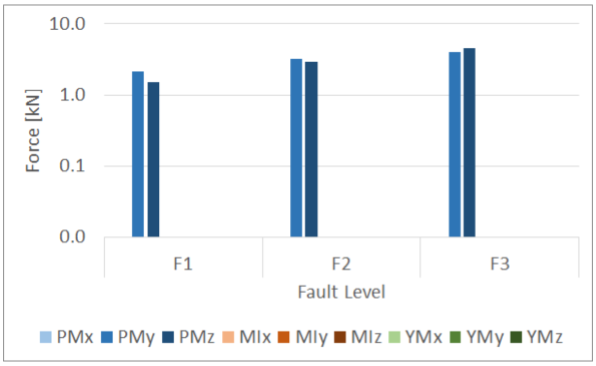

(d) 2P LSS Force Above Rated U_4 = 12m/s

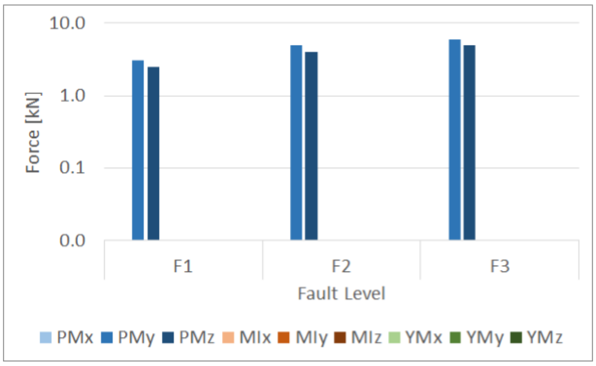

(e) 2P LSS Force Above Rated U_5 = 14m/s

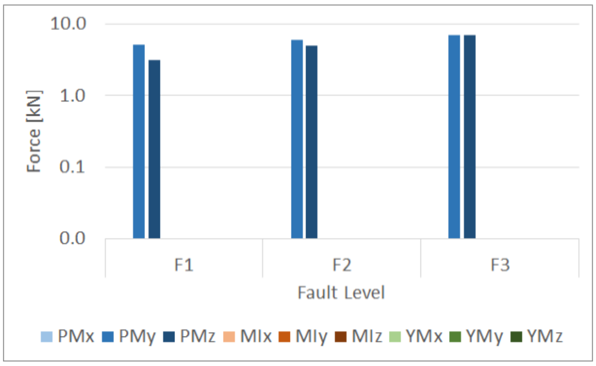

(f) 2P LSS Force Above Rated U_6 = 20m/s

Figure B.11: Absolute Change in LSS Force Below and Above Rated Wind Speeds at 2P Frequency in Turbulent Wind Conditions

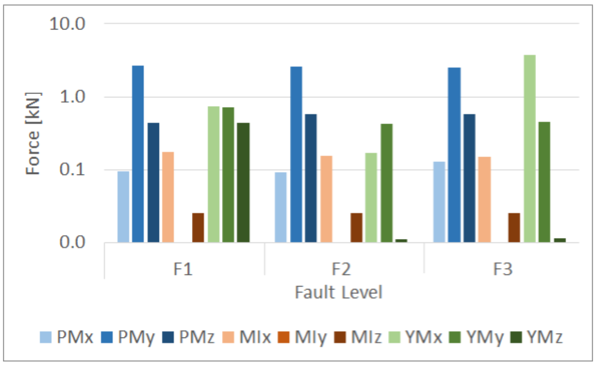

(a) 3P LSS Force Below Rated U_1 = 4m/s

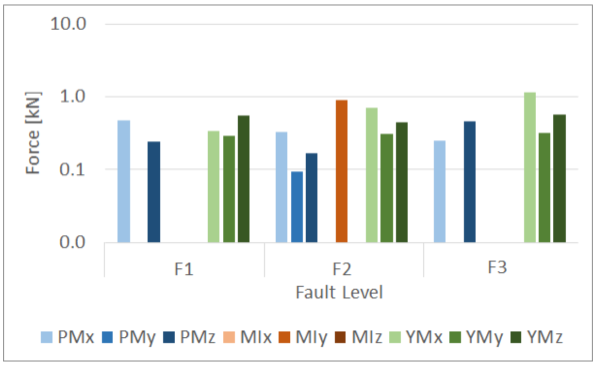

(b) 3P LSS Force Below Rated U_2 = 7m/s

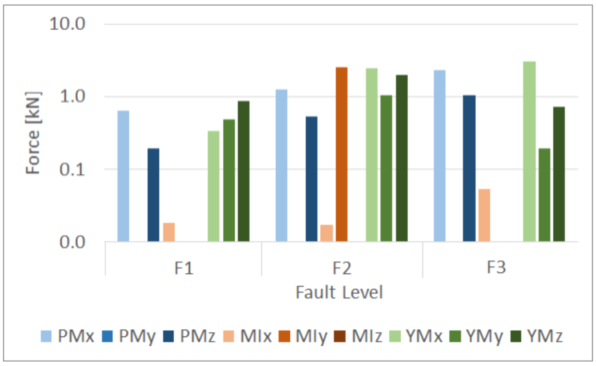

(c) 3P LSS Force Above Rated U_3 = 10m/s

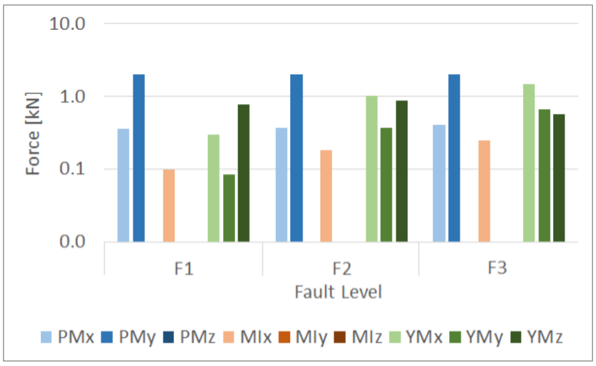

(d) 3P LSS Force Above Rated U_4 = 12m/s

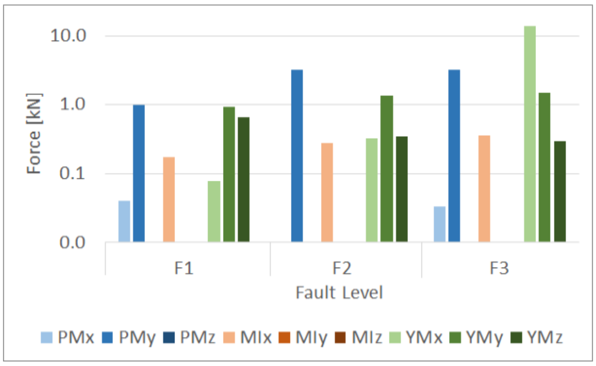

(e) 3P LSS Force Above Rated U_5 = 14m/s

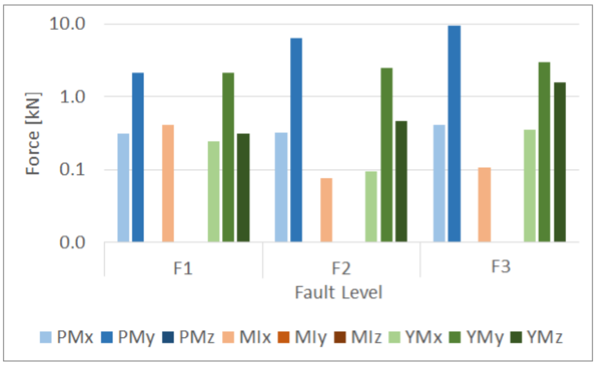

(f) 3P LSS Force Above Rated U_6 = 20m/s

Figure B.12: Absolute Change in LSS Force Below and Above Rated Wind Speeds at 3P Frequency in Turbulent Wind Conditions

C

FFT of the Signal at Steady Wind Conditions

C.1. Pitch Misalignment

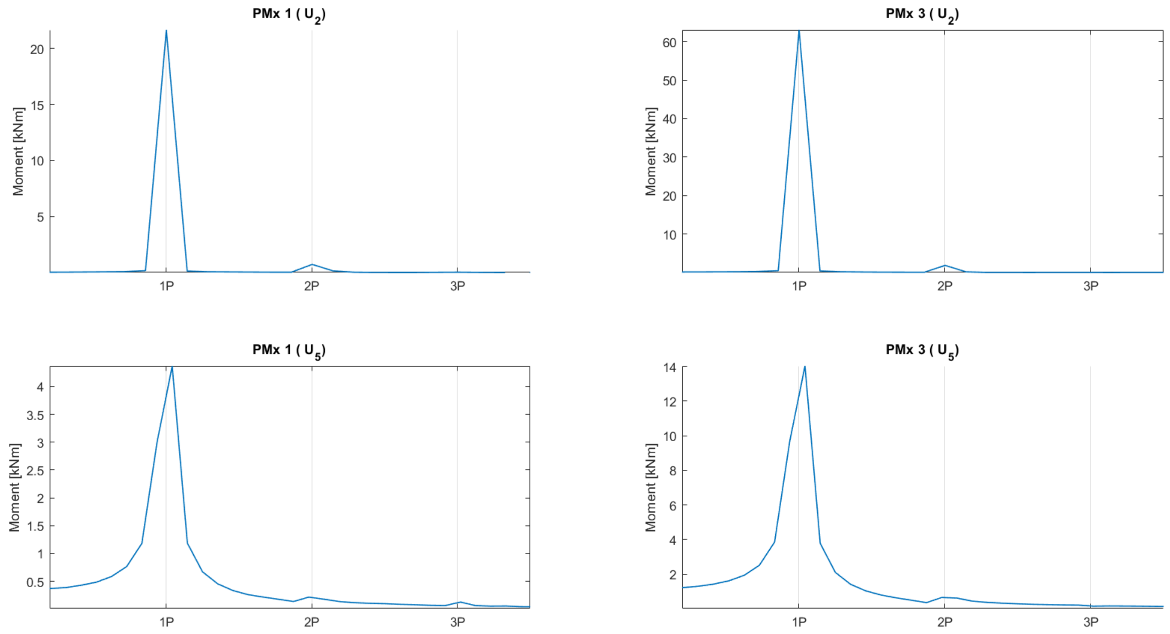

Figure C.1: FFT of PMx LSS Torque at different fault levels and wind speeds

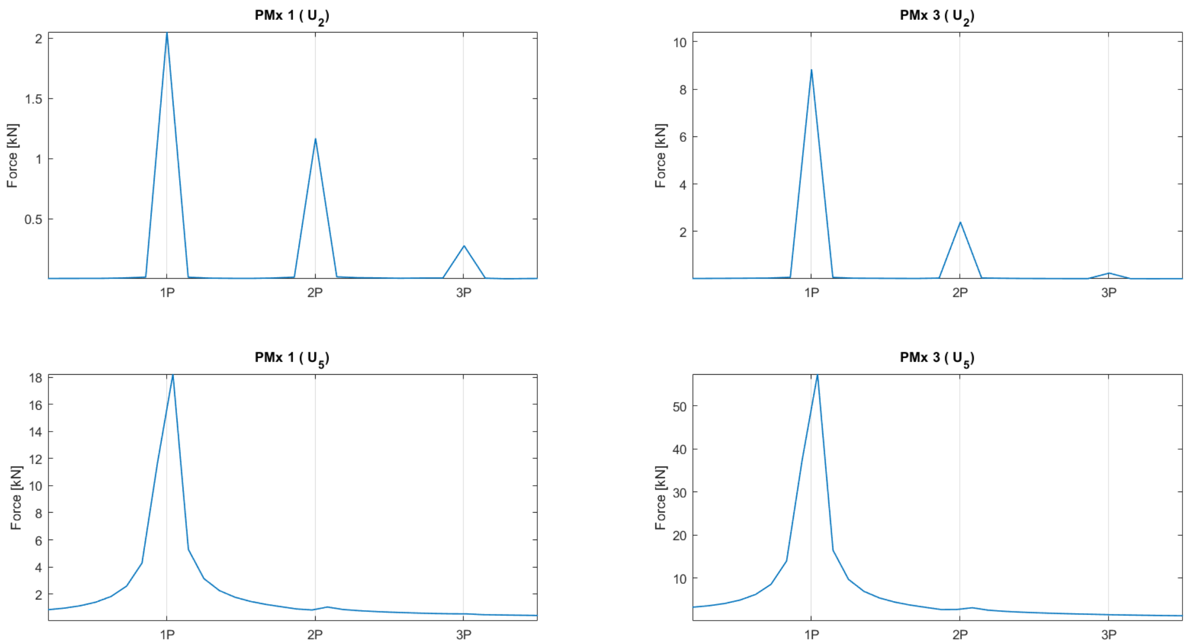

Figure C.2: FFT of PMx LSS Thrust at different fault levels and wind speeds

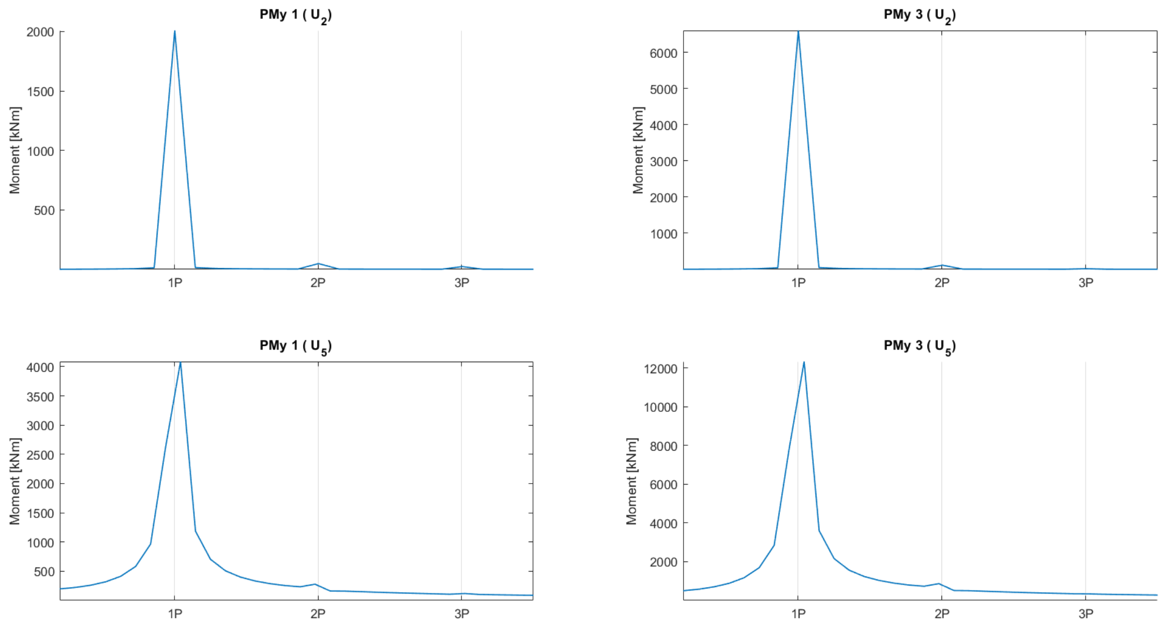

Figure C.3: FFT of PMy LSS Moment at different fault levels and wind speeds

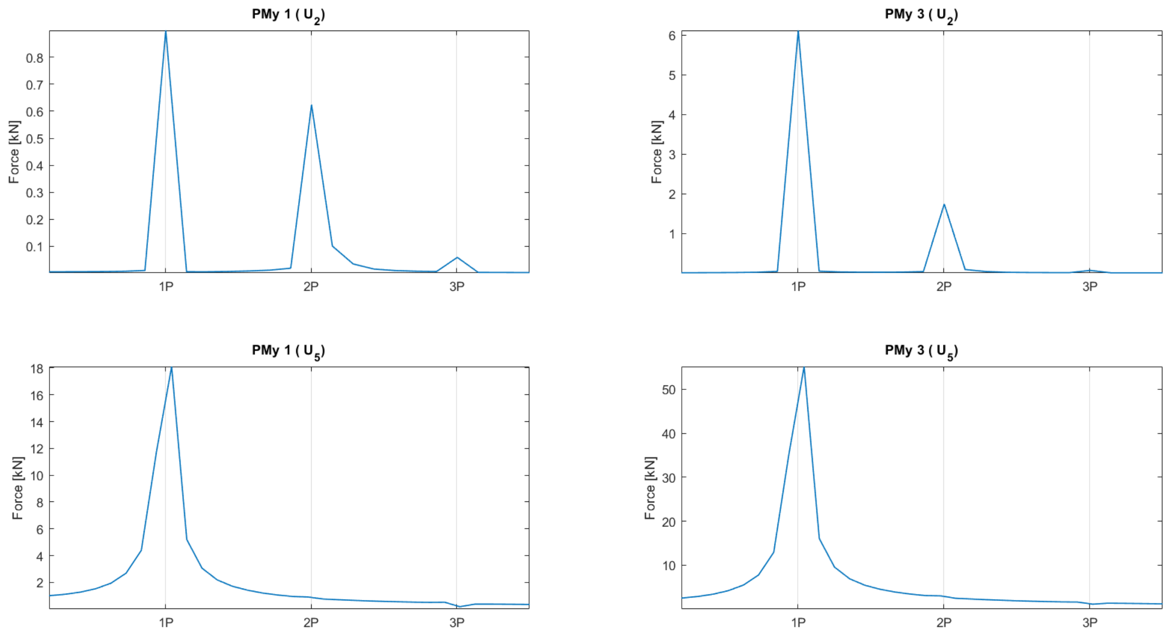

Figure C.4: FFT of PMy LSS Force at different fault levels and wind speeds

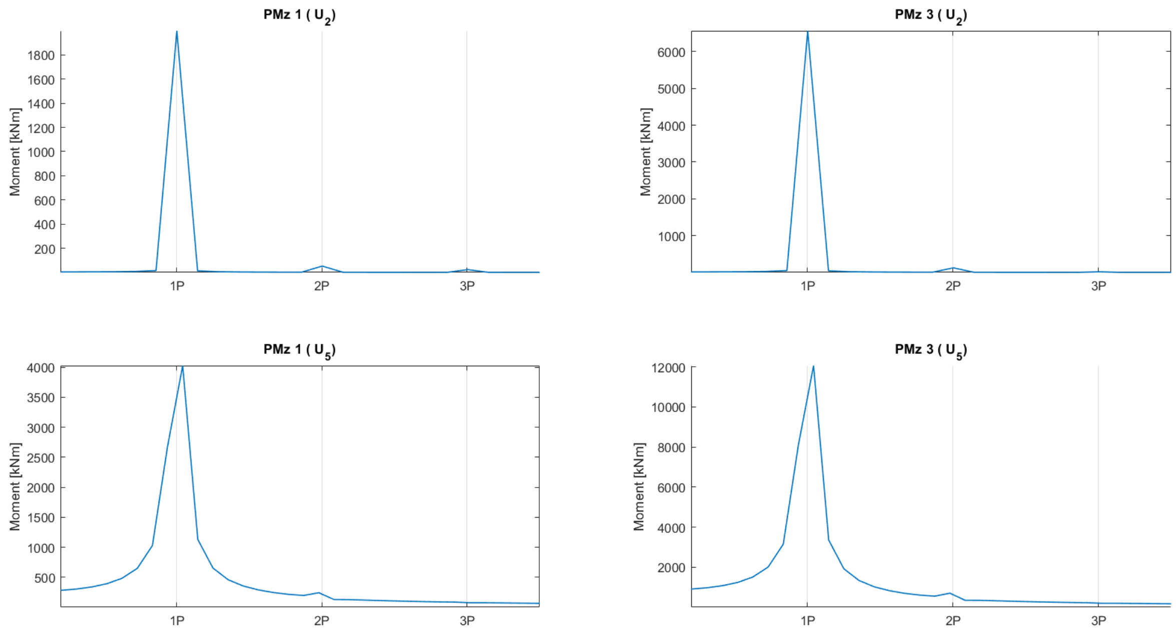

Figure C.5: FFT of PMz LSS Moment at different fault levels and wind speeds

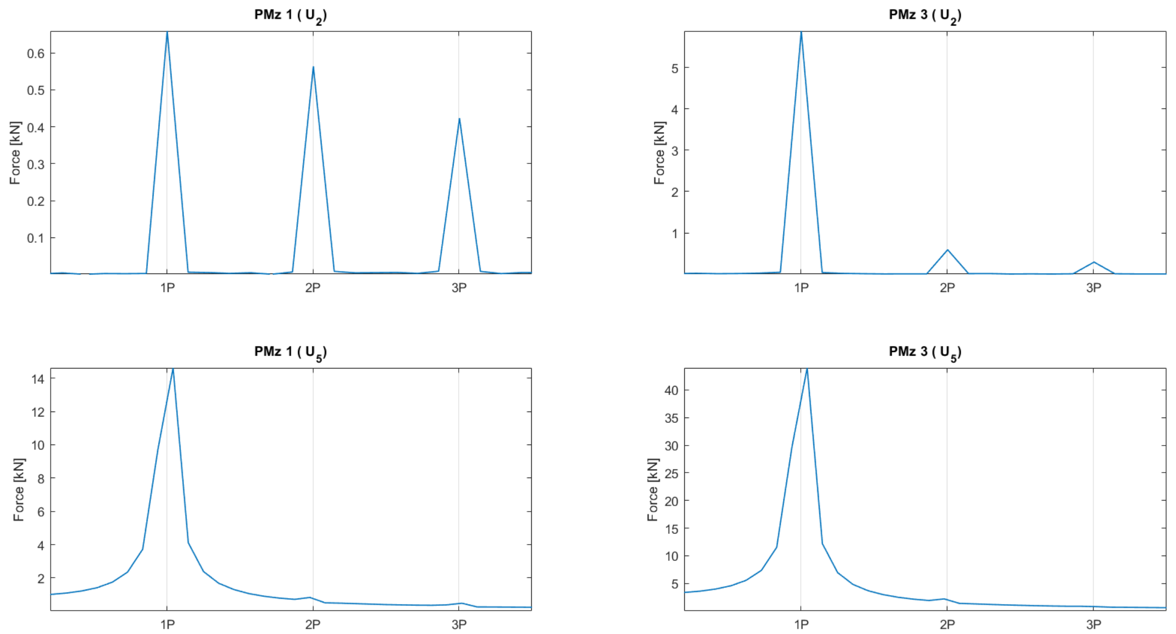

Figure C.6: FFT of PMz LSS Force at different fault levels and wind speeds

C.2. Mass Imbalance

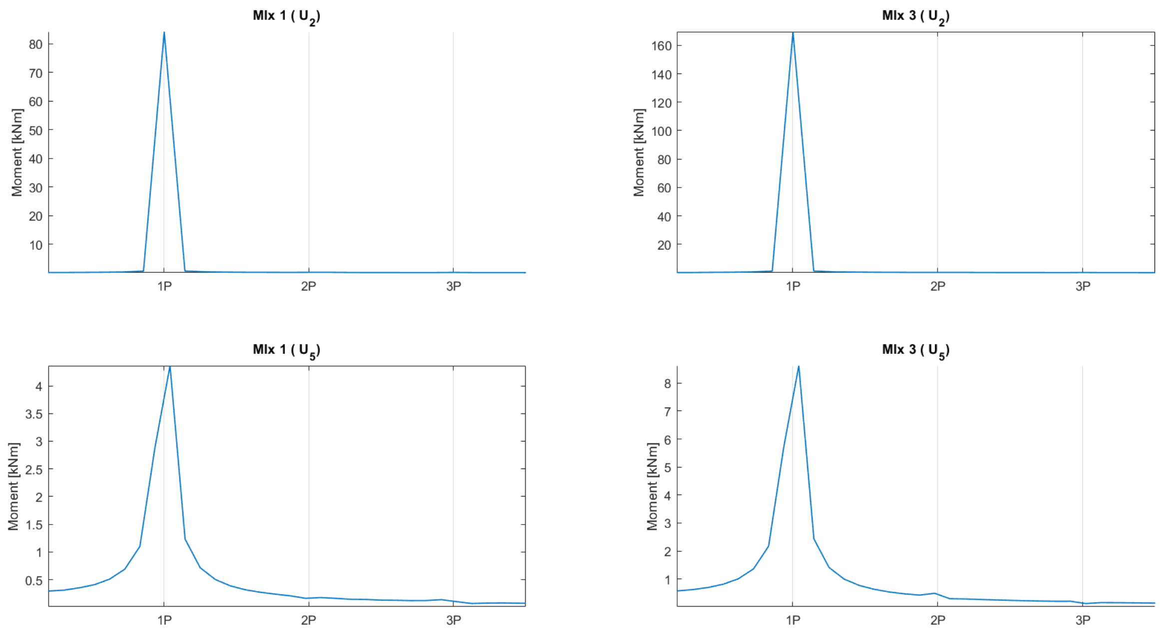

Figure C.7: FFT of MIx LSS Torque at different fault levels and wind speeds

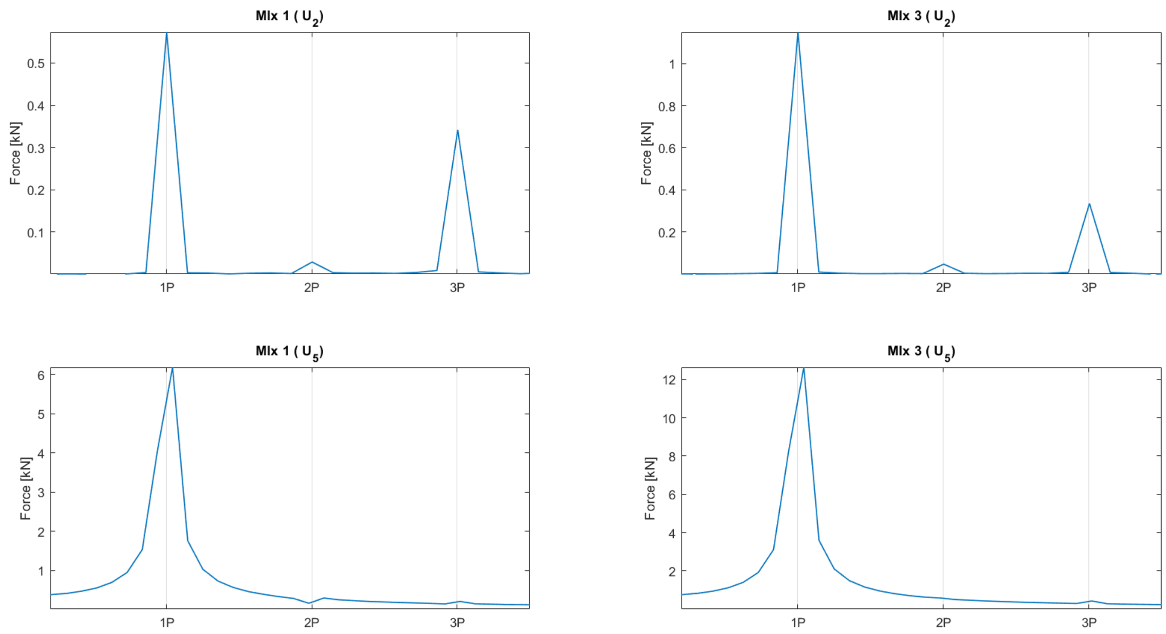

Figure C.8: FFT of MIx LSS Thrust at different fault levels and wind speeds

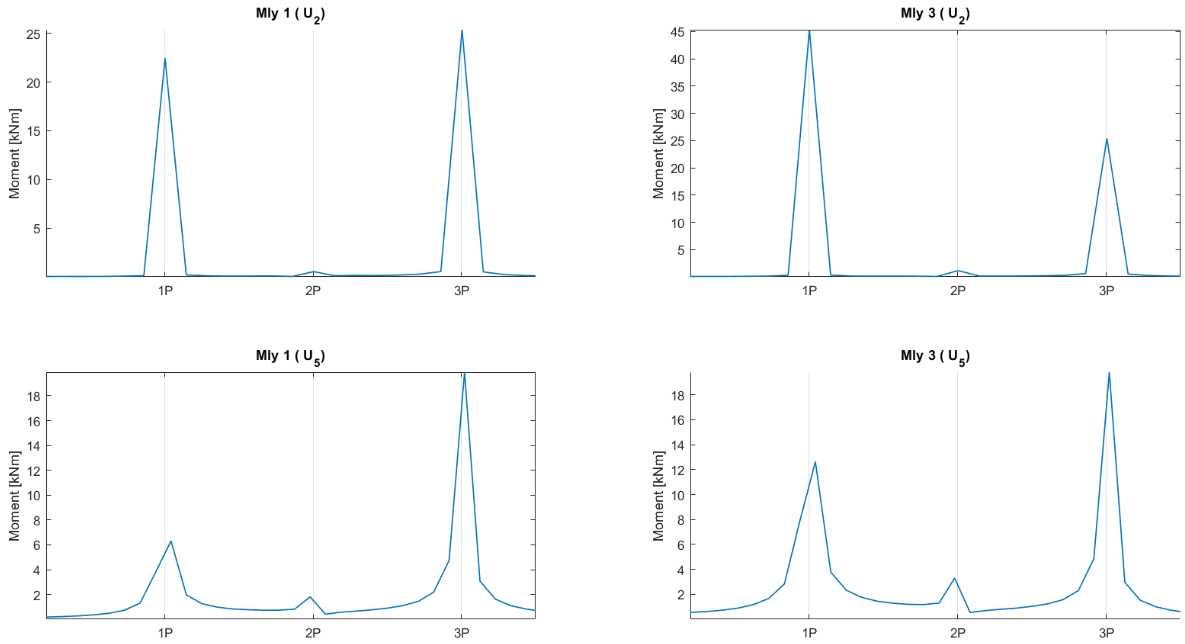

Figure C.9: FFT of MIy LSS Moment at different fault levels and wind speeds

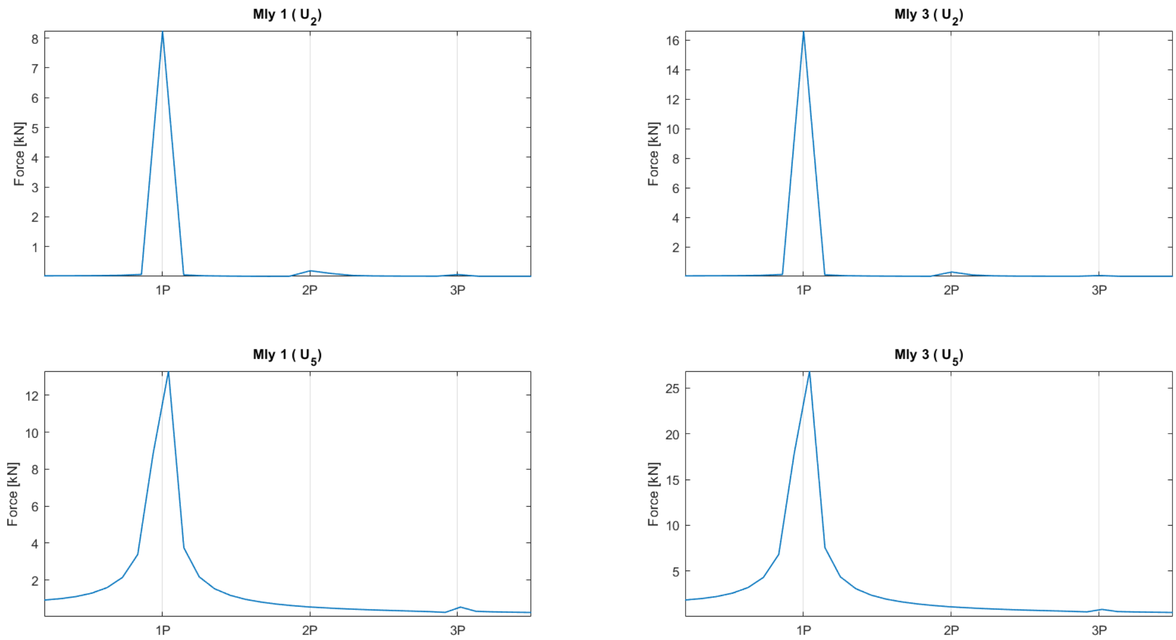

Figure C.10: FFT of MIy LSS Force at different fault levels and wind speeds

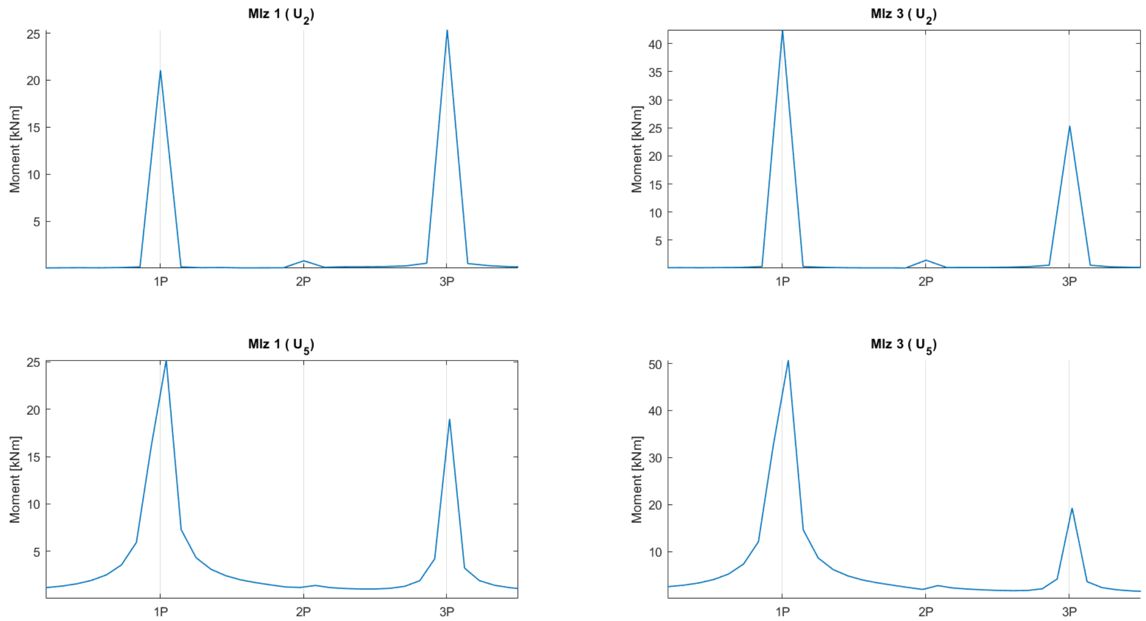

Figure C.11: FFT of MIz LSS Moment at different fault levels and wind speeds

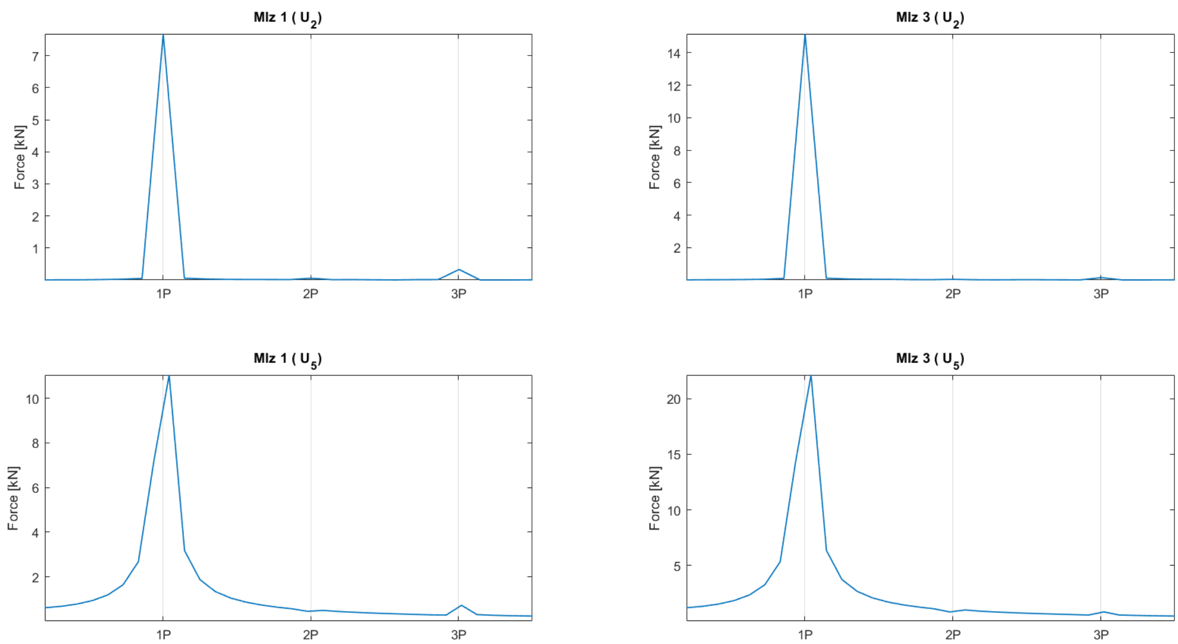

Figure C.12: FFT of MIz LSS Force at different fault levels and wind speeds

C.3. Yaw Misalignment

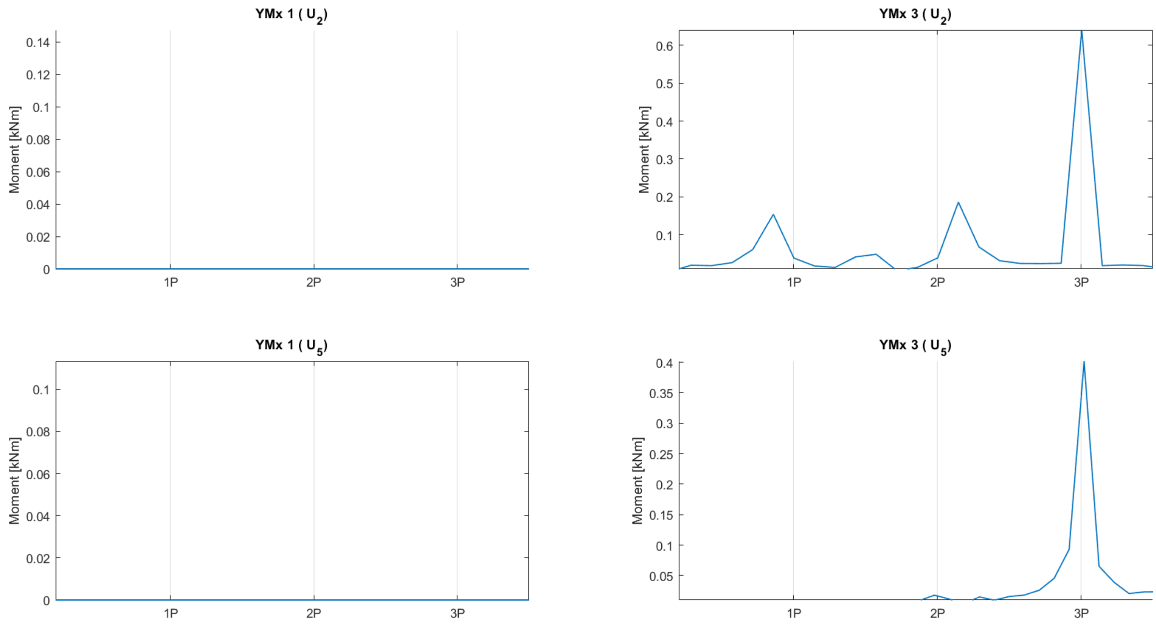

Figure C.13: FFT of YMx LSS Torque at different fault levels and wind speeds

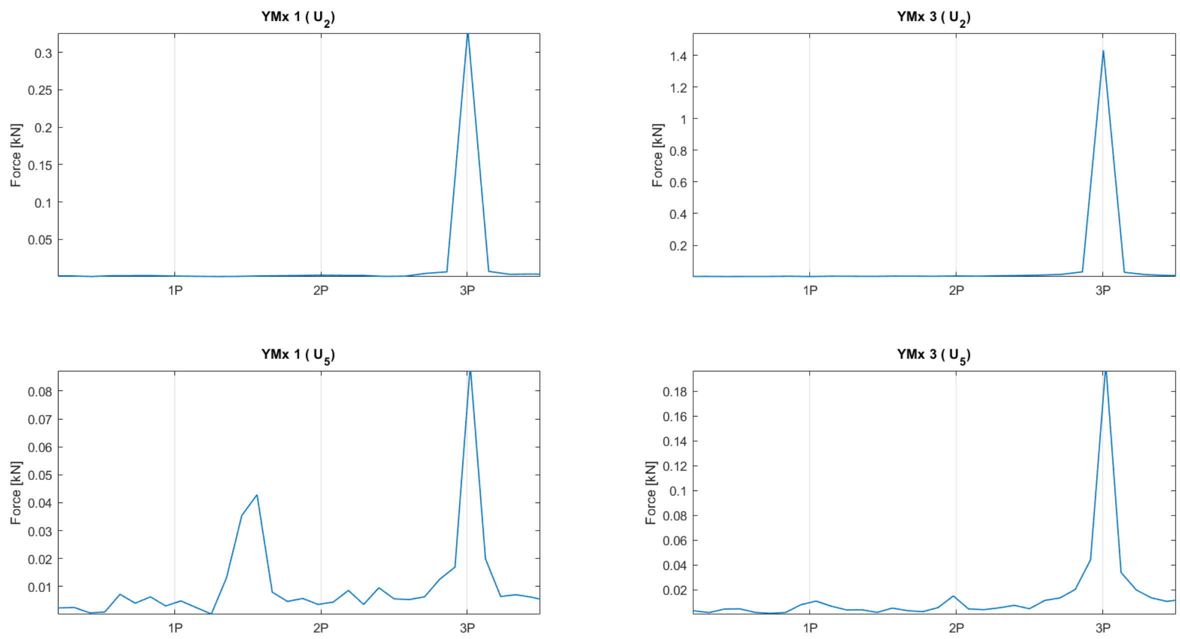

Figure C.14: FFT of YMx LSS Thrust at different fault levels and wind speeds

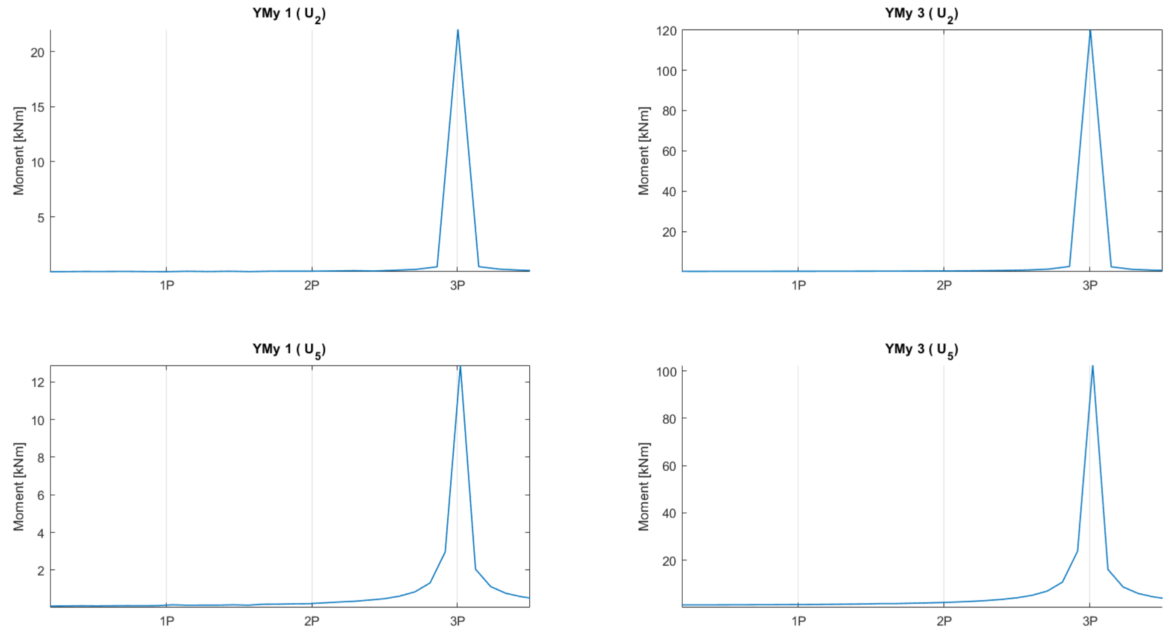

Figure C.15: FFT of YMy LSS Moment at different fault levels and wind speeds

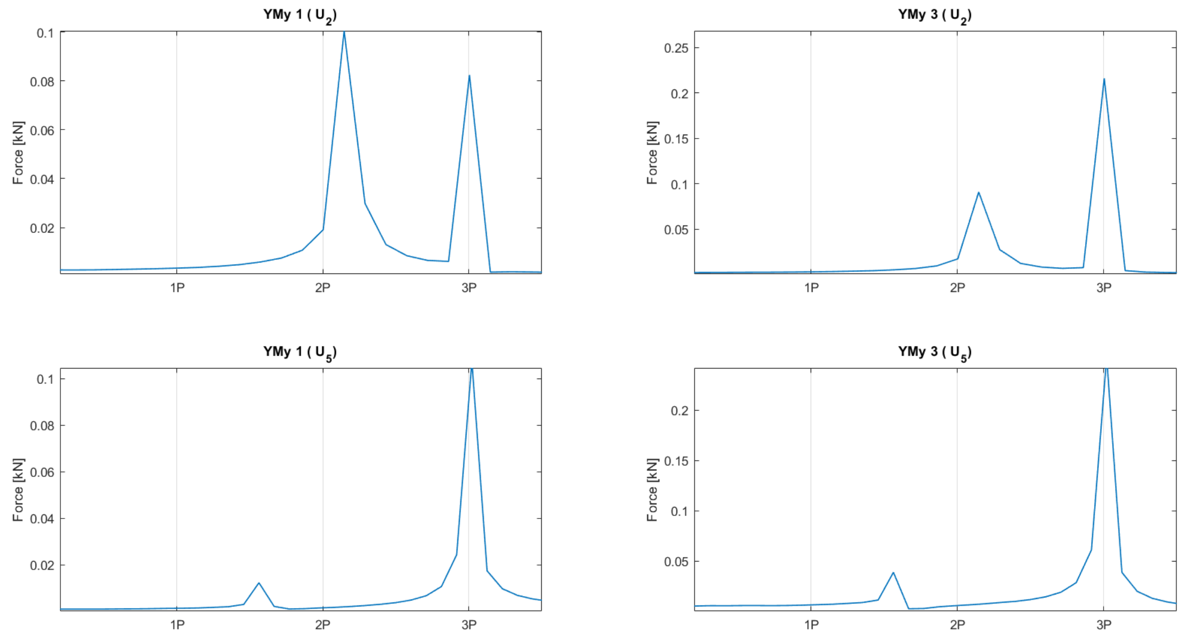

Figure C.16: FFT of YMy LSS Force at different fault levels and wind speeds

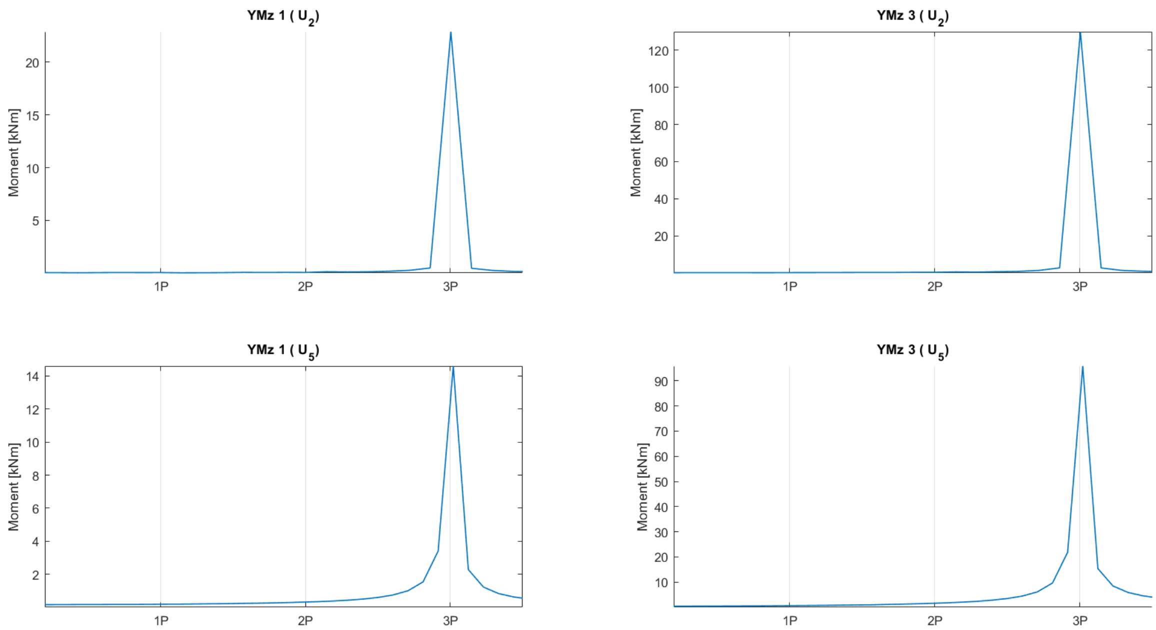

Figure C.17: FFT of YMz LSS Moment at different fault levels and wind speeds

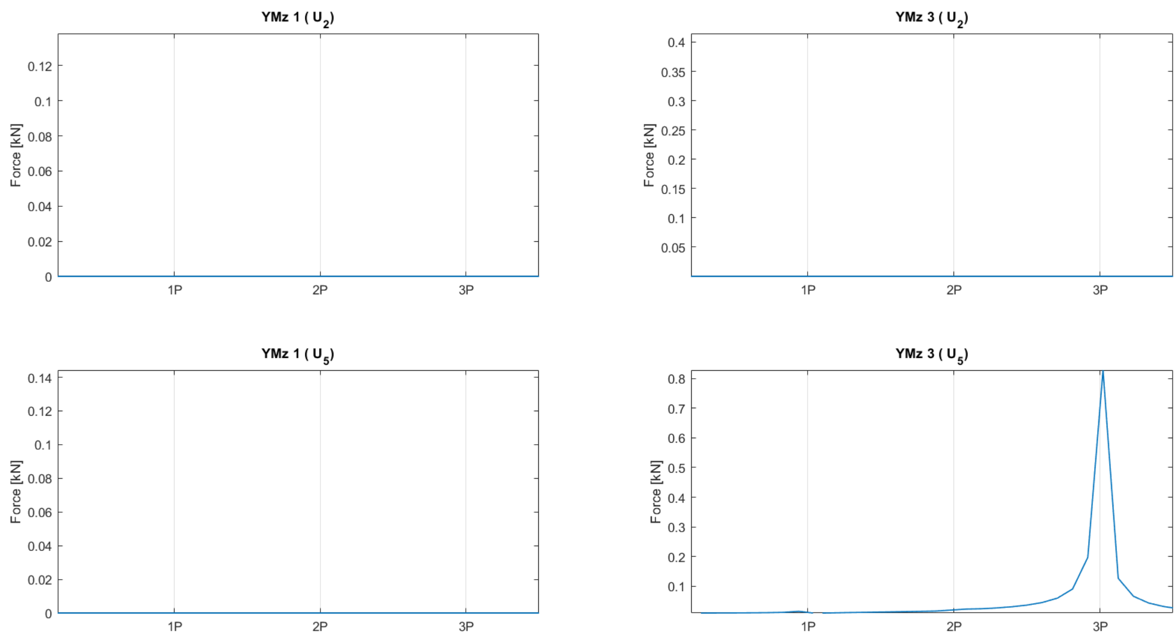

Figure C.18: FFT of YMz LSS Force at different fault levels and wind speeds